

Titre: Nickel Coated Carbon Fibre Nonwoven as Light, Efficient and Scalable Lightning Strike Protection for Carbon Fibre Reinforced Polymers
Title:

Auteur: Etienne Gourcerol
Author:

Date: 2022

Type: Mémoire ou thèse / Dissertation or Thesis

Référence: Gourcerol, E. (2022). Nickel Coated Carbon Fibre Nonwoven as Light, Efficient and Scalable Lightning Strike Protection for Carbon Fibre Reinforced Polymers
Citation: [Mémoire de maîtrise, Polytechnique Montréal]. PolyPublie.
<https://publications.polymtl.ca/10363/>

 **Document en libre accès dans PolyPublie**
Open Access document in PolyPublie

URL de PolyPublie: <https://publications.polymtl.ca/10363/>
PolyPublie URL:

Directeurs de recherche: Daniel Therriault, & Frédéric Sirois
Advisors:

Programme: Génie aérospatial
Program:

POLYTECHNIQUE MONTRÉAL

affiliée à l'Université de Montréal

**Nickel Coated Carbon Fibre Nonwoven as Light, Efficient and Scalable
Lightning Strike Protection for Carbon Fibre Reinforced Polymers**

ETIENNE GOURCEROL

Département de génie mécanique

Mémoire présenté en vue de l'obtention du diplôme de *Maîtrise ès sciences appliquées*

Génie aérospatial

Mai 2022

© Etienne Gourcerol, 2022.

POLYTECHNIQUE MONTRÉAL

affiliée à l'Université de Montréal

Ce mémoire intitulé :

Nickel Coated Carbon Fibre Nonwoven as Light, Efficient and Scalable Lightning Strike Protection for Carbon Fibre Reinforced Polymers

présenté par **Etienne GOURCEROL**

en vue de l'obtention du diplôme de *Maîtrise ès sciences appliquées*

a été dûment accepté par le jury d'examen constitué de :

Jean-Jacques LAURIN, président

Daniel THERRIault, membre et directeur de recherche

Frédéric SIROIS, membre et codirecteur de recherche

Fabien THOLIN, membre

ACKNOWLEDGEMENTS

I would like to thank my research supervisors Frédéric Sirois and Daniel Therriault for their guidance and support during my first steps in research, even when I was stuck on the other side of the Atlantic Ocean.

I would also like to thank the other members of the “Bell LSP” project: David Brassard for his experience in conducting a research project and the fount of knowledge that he is, Kambiz Chizari for the project management and the feedbacks to improve our presentation, Jean Langot for his constant drive to move forward despite the delays and the disappointments as well as his beautiful schematics, and finally Anamaria Serbescu for her support during these 18 months as desk neighbours, for the interesting talks we had, and for welcoming me in Montreal. I would like to thank Maxime Lapalme and Alexandra Desautels from Bell Textron for their help and desire to see this project succeed.

Finally, I would like to thank the “Phamille” of the JAB students for the enriching time spent together.

RESUME

Le secteur aéronautique s'est engagé à réduire ses émissions de CO₂, dans le but d'atteindre la neutralité carbone d'ici 2050. L'utilisation croissante de matériaux composites pour remplacer l'aluminium dans les pièces structurelles contribuera à accroître le rendement énergétique des avions. En effet, les polymères renforcés de fibres de carbone ont de meilleures propriétés mécaniques spécifiques que l'aluminium. Cependant, leur conductivité électrique est plus faible, ce qui les rend plus vulnérables aux dommages causés par la foudre. En effet, un avion commercial est frappé en moyenne une fois par an par la foudre. Pour compenser cette faiblesse, un grillage métallique est ajouté sur les composites pour protéger la structure contre la foudre. Ce grillage est efficace mais lourd. L'objectif de ce projet est d'étudier l'efficacité de protection contre la foudre d'une couche légère et capable d'être facilement mise à l'échelle protégeant des panneaux composites peints contre les dommages structurels, en utilisant des matériaux fabriqués commercialement à base de fibres de carbone recouvertes de nickel (FCRN).

Deux stratégies sont envisagées. Pour la première, un tissé de FCRN sec est intégré à l'aide d'une couche de résine époxy comme premier pli d'un stratifié à 8 plis, ajoutant ~150 g/m². Pour la seconde, quatre types de voiles non-tissés de FCRN sont ajoutés au-dessus d'un stratifié à 8 plis, ajoutant respectivement 18, 19, 43 et 70 g/m². Plus la densité surfacique est élevée, plus la résistivité de surface du voile est faible et plus le revêtement de nickel sur les fibres est épais.

Les panneaux protégés peints et non peints sont testés avec un émulateur de foudre de 40 kA, développé à Polytechnique Montréal. La surface des panneaux est observée avec une caméra thermique à haute vitesse durant le test. La caractérisation des dommages est effectuée à l'aide de quatre méthodes : une inspection par ultrasons pour les dommages en surface et interne, une observation en coupe ainsi qu'une microtomographie à rayons X pour les dommages internes et un test de flexion à 4 points pour évaluer la conservation des propriétés mécaniques après le test. Les résultats des panneaux protégés par des matériaux à base de FCRN sont comparés à deux types de panneaux de référence : des stratifiés à 8 plis protégés par un maillage de cuivre de 360 g/m² et des stratifiés à 8 plis non-protégés.

Sans peinture, les panneaux protégés par le voile non-tissé avec la plus faible résistivité de surface ne présentent aucun dommage interne et une conservation de la résistance mécanique à la flexion de 97%, plus élevée que celle des panneaux protégés par le maillage de cuivre. Le non-tissé est à peine évaporé à la surface du panneau, ce qui confirme l'absence de zones de haute température observée avec la caméra thermique et indique la bonne dispersion de l'énergie de l'éclair. Le tissé de FCRN conserve 63% de sa résistance à la flexion, ce qui est dans la même plage que le stratifié non-protégé. Les panneaux peints protégés par les non-tissés sont plus sévèrement endommagés que ceux protégés par l'ECF, conservant au mieux 69% de leur résistance à la flexion. A cause de la peinture, le courant de foudre a été conduit plus profondément dans le stratifié. En raison de l'effet Joule, la résine a pyrolysé à l'intérieur du stratifié. L'accumulation de gaz a généré des surpressions qui ont conduit à des délaminations et à la rupture des fibres de carbone dans les premiers plis. La peinture n'a pas eu d'effet sur les propriétés mécaniques des panneaux protégés par le maillage de cuivre : ils ont conservé la même résistance à la flexion que leurs homologues non peints avec 83 %.

Les non-tissés de FCRN constituent une alternative prometteuse aux grillage métallique. Le voile de 70 g/m² est 80 % plus léger, 30 % moins cher et aussi efficace sans peinture. La mise à l'échelle de cette solution est simple car celle-ci est déjà commercialisée et pourrait être pré-imprégnée de résine. Cependant, des recherches supplémentaires sont nécessaires pour réduire l'effet néfaste de la peinture sur l'efficacité de protection contre la foudre et rendre cette solution utilisable par l'industrie aéronautique.

ABSTRACT

The aviation industry is committed to reduce its CO₂ emissions to a net zero level by 2050. The increasing use of composite materials as a replacement for aluminium in structural parts will help increase the fuel efficiency of aircraft. Indeed, carbon fibre reinforced polymers (CFRP) have better specific mechanical properties than aluminium. However, their lower electrical conductivity makes them more subject to lightning strike damage. Indeed, a commercial airplane is struck in average one time per year by lightning. To compensate this weakness, a metallic mesh is added on top of the composites to protect the structure from lightning strike. The addition of metal mesh is efficient but heavy. The aim of this project is to investigate the lightning strike protection (LSP) efficiency of a light and scalable layer that protects painted composite panels from structural damage, using dry commercially fabricated nickel coated carbon fibre (NCCF)-based materials.

Two strategies are considered. For the first one, a woven NCCF fabric is integrated by wet lay-up as the first ply of an 8-ply laminate, adding ~150 g/m². For the second one, four types of nonwoven NCCF veils are stacked on top of an 8-ply laminate, adding respectively 18, 19, 43 and 70 g/m². The higher the areal density is, the lower the sheet resistivity and the thicker the nickel coating on the fibres.

Painted and nonpainted protected panels are tested with an in-house 40 kA lightning strike emulator and observed during the test with a high-speed thermal camera. The damage characterisation is made using four methods: an ultrasonic inspection for the surface and internal damage, a cross-section observation and an X-ray microtomography scan for the internal damage, and a 4-point bending test to assess the mechanical properties retention after the test. The results of the NCCF-based LSP are compared with two reference panels: 8-ply laminates protected by a 360 g/m² expanded copper foil (ECF) and non-protected 8-ply laminates.

Without paint, the panels protected by the nonwoven veil with the lowest sheet resistivity show no internal damage and a mechanical flexural strength retention of 97%, higher than the ECF-protected panels. The nonwoven is scarcely evaporated on the panel surface, confirming the absence of high temperature areas observed with the thermal camera and indicating the good dispersion of the lightning strike energy. The woven cloth maintains 63% of its flexural

strength, which is in the same range as the non-protected laminate. The painted panels protected by the nonwoven veils are more severely damaged than the ones protected by the ECF, retaining at best 69% of their flexural strength. The lightning current was conducted deeper in the laminate and the pyrolysis gas, released from the heating of the resin in the depth of the laminate, generated overpressures that led to delamination and fibre breakage in the first plies. However, paint had no effect on the mechanical properties of the ECF-protected panels: they retained the same flexural strength as their nonpainted counterparts with 83%.

Nonwoven NCCF are a promising alternative to the ECF. The 70 g/m² veil is 80% lighter, 30% cheaper and as efficient without paint. The scalability of this solution is straightforward as it is already commercialised and could be pre-impregnated with resin. However, further investigations are required to overcome the detrimental effect of paint on the lightning strike protection efficiency and make this solution applicable.

TABLE OF CONTENTS

ACKNOWLEDGEMENTS.....	III
RESUME.....	IV
ABSTRACT.....	VI
TABLE OF CONTENTS.....	VIII
LIST OF TABLES.....	XI
LIST OF FIGURES.....	XII
LIST OF SYMBOLS AND ABBREVIATIONS.....	XV
LIST OF APPENDICES.....	XVI
CHAPTER 1 INTRODUCTION.....	1
CHAPTER 2 REVIEW.....	3
2.1 Lightning strikes to aircraft	3
2.1.1 Natural formation of lightning	3
2.1.2 Lightning-aircraft interaction	6
2.2 Damage to carbon fibre reinforced polymers.....	12
2.2.1 Direct effects	12
2.2.2 Indirect effects.....	18
2.3 Lightning strike protection	18
2.3.1 On top of the laminate	20
2.3.2 Inside the laminate	28
2.3.3 Commercialised lightning strike protection	31
2.3.4 Conclusion and research objectives	32
CHAPTER 3 METHODOLOGY - EXPERIMENTAL PLAN.....	37
3.1 Materials.....	37
3.1.1 Selection	37

3.1.2	Integration	38
3.2	Pre lightning strike test characterisation	41
3.2.1	Mass and thickness	41
3.2.2	Scanning electron microscopy (SEM).....	41
3.2.3	Simultaneous thermal analysis (STA).....	41
3.2.4	Emissivity.....	41
3.2.5	Conductivity measurements	42
3.3	Lightning strike test.....	44
3.3.1	Lightning strike emulator	44
3.3.2	Voltage and current measurements	46
3.3.3	High-speed thermal camera.....	46
3.4	Post lightning strike test	46
3.4.1	Visual observation.....	46
3.4.2	Ultrasonic testing (C-Scan)	46
3.4.3	X-ray microtomography (μ -CT).....	47
3.4.4	4-point bending test (4PBT).....	47
CHAPTER 4	RESULTS.....	51
4.1	Integration	51
4.1.1	Integration test.....	51
4.1.2	Final integration	52
4.2	Pre lightning strike test characterisation	53
4.2.1	Dry mass and thickness	53
4.2.2	Scanning electron microscopy (SEM).....	55
4.2.3	Conductivity measurements	58
4.3	Lightning strike test.....	60
4.3.1	Voltage and current measurements	60

4.3.2	High-speed thermal camera.....	62
4.4	Post lightning strike test	66
4.4.1	Surface damage	66
4.4.2	Internal damage	68
4.4.3	4 points bending test.....	78
4.5	Cost.....	81
4.6	Damage mechanisms and discussion on LSP efficiency	82
4.6.1	ECF and PECF	82
4.6.2	NS and CF	82
4.6.3	PNS and PCF.....	83
4.6.4	Different behaviour of the painted panels	84
4.6.5	NC	85
CHAPTER 5	CONCLUSION	87
5.1	Summary of the results.....	87
5.2	Future work	88
5.3	Outcomes.....	88
REFERENCES	90
APPENDICES	97

LIST OF TABLES

Table 2.1: Main properties of nickel, silver, and copper.....	33
Table 2.2: Summary of the published LSP layers that were tested.....	34
Table 3.1: Areal density and sheet resistivity ranges from commercialised nonwoven NCCF.	38
Table 4.1: Average thickness of the panels and paint thickness measured.....	55
Table 4.2: Stored energy between 20 °C and vaporisation per mass for copper, nickel and graphite.....	58
Table 4.3: Stored energy per area in each LSP layer.	58
Table 4.4: Waveform parameters of the tested panels.	62
Table 4.5: Diameter of the internal damage and damage depth of each solution after LS test.	77
Table 4.6: Flexural strength and effective bending stiffness before and after LS for each solution.....	79
Table 6.1: Materials emissivity measured with a reflectometer.....	112
Table 6.2: Equivalent electrical conductivity of the NCCF filament of the woven and nonwoven in comparison with the copper filament.	113

LIST OF FIGURES

Figure 2.1: Positive and negative leaders structure and propagation.	4
Figure 2.2: Typical waveform of a negative CG flash.	5
Figure 2.3: Lightning-aircraft interaction.	7
Figure 2.4: Sweeping effect.	8
Figure 2.5: Examples of zoning on the nose and the wingtips of an airplane.	10
Figure 2.6: Zoning of a helicopter with horizontal stabilizer.	10
Figure 2.7: Lightning current waveform parameters and link with zoning.	11
Figure 2.8: Thermal, electrical and mechanical constraints at the attachment point on a CFRP.	13
Figure 2.9: Evolution of the lightning damage on a 13 plies CFRP protected by an ECF with different paint thickness.	17
Figure 2.10: Expanded copper foil details.	19
Figure 2.11: Evolution of the number of published articles and LSP solutions, tested with a lightning strike, since 1993.	20
Figure 2.12: Recommended disposition of the ECF in swept stroke zone.	22
Figure 2.13: Temperature profiles of the nonprotected and PANI-protected panels after 120 ms.	24
Figure 2.14: Views of the ECF- or nonwoven NCCF- protected laminates after lightning strike with a waveform D.	26
Figure 2.15: Cross-section and top views of the CF/PANI with various through-thickness conductivities after a 43 kA lightning strike test.	30
Figure 3.1: Integration test panels configuration.	39
Figure 3.2: Test panels configuration for each LSP solution.	40
Figure 3.3: 4-point probe and 2-point probe methods with equivalent electrical diagram.	43
Figure 3.4: 4-point probe method setup.	44
Figure 3.5: Lightning strike emulator and equivalent electrical circuit.	45

Figure 3.6: Cutting patterns on damaged samples.	47
Figure 3.7: 4-point bending test method and set-up.	48
Figure 3.8: Deflection-load curve of a typical 4-point bending test.	49
Figure 3.9: Experimental plan for each LSP solution.	50
Figure 4.1: Full and zoomed views of the integration test panels after LS test.	52
Figure 4.2: Top view of the surface of NS0.1 after curing.	53
Figure 4.3: Same scale cross-section views of a NS0.04 and a PNS0.04 panels.	53
Figure 4.4: Measured dry mass of the LSP solutions and total mass of the LSP considering the dry material and the adhesive/resin necessary for the integration.	54
Figure 4.5: Scanning electron microscope observations of the nickel coating thickness on the woven NCCF.	56
Figure 4.6: Scanning electron microscope observations of the nickel coating thickness on a filament of a nonwoven NCCF.	56
Figure 4.7: Sheet resistivity of the dry and integrated materials.	59
Figure 4.8: NS0.1 cross-section observation with optical microscope	59
Figure 4.9: Measured sheet resistivity of the nonpainted panels and equivalent sheet resistivity of the panels considering the dry NCCF materials and the CF laminate in parallel.	60
Figure 4.10: Typical test waveform produced by the lightning strike emulator developed at Polytechnique Montreal.	61
Figure 4.11: Surface temperature of composites panels recorded by the high-speed thermal camera.	63
Figure 4.12: Areas above 100 °C and 200 °C observed with the high-speed thermal camera.	65
Figure 4.13: Top and close-up views of one damaged nonpainted panel per solution.	67
Figure 4.14: Top and close-up-views of one damaged painted panel per solution.	69
Figure 4.15: C-Scan of one damaged nonpainted panel per solution.	70
Figure 4.16: C-Scan of one damaged painted panel per solution.	70

Figure 4.17: Damaged area of the nonpainted and painted panels measured with C-Scan.	72
Figure 4.18: Damaged nonpainted panels cross-section observation.....	73
Figure 4.19: Damaged painted panels cross-section observation.	74
Figure 4.20: X-ray microtomography observations of a NS0.5 panel with a top and two cross-section views and a NS0.1 panel with a top and one cross-section view.....	76
Figure 4.21: Flexural strength retention of nonpainted and painted panels after LS test.	80
Figure 4.22: Effective bending stiffness retention of nonpainted and painted panels after LS test.	81
Figure 4.23: Price of the LSP layers.	81
Figure 4.24: Damage mechanism of nonpainted panels and three damage types.....	83
Figure 4.25: Damage mechanism of painted panels and two damage types.....	84
Figure 6.1: Typical electric charge distribution in a thundercloud and lightning strike altitude distribution..	98
Figure 6.4: Microstructure of protected panels with and without a glassfibres ply below the LSP layer post-lightning.....	104
Figure 6.5: Views of laminates manufactured with different resin after a 100 kA lightning strike test.	107
Figure 6.6: Insertion of the MWCnT-based film between the first 4 layers and on top of the laminate to enhance the through-thickness conductivity.	109
Figure 6.7: Thermogravimetric analysis of a CF panels at three heating rates.....	111
Figure 6.8: Emissivity of a CF sample at different temperatures and for infrared wavelength ranging from 2.5 μm to 25 μm	112
Figure 6.9: Observed electrical arc attachment behaviours on the surface of nonpainted and painted composite panels.	115

LIST OF SYMBOLS AND ABBREVIATIONS

2PPM	2-point probe method
4PPM	4-point probe method
4PB	4-point bending
C-Scan	Ultrasonic non-destructive testing
CF	Carbon fibres
CFRP	Carbon fibre reinforced polymers
ECF	Expanded copper foil
EMI	Electromagnetic interference
LS	Lightning strike
LSP	Lightning strike protection
NW	Nonwoven
NC	NiCloth. Name of the woven NCCF-protected panels
NS	NiShield. Name of the nonwoven NCCF-protected panels
SEM	Scanning electron microscopy
STA	Simultaneous thermal analysis
W	Woven
μ -CT	X-ray microtomography
ρ_s	Sheet resistivity
t_1	Time to peak
t_2	Time to half peak value

LIST OF APPENDICES

Appendix A	Exhaustive literature review	97
Appendix B	Simultaneous thermal analysis (STA)	111
Appendix C	Emissivity	112
Appendix D	Computation of the equivalent electrical conductivity based on SEM observations.....	113
Appendix E	Electrical arc attachment observations.....	114

CHAPTER 1 INTRODUCTION

In October 2016, the International Civil Aviation Organisation adopted the Carbon Offsetting and Reduction Scheme for International Aviation (CORSIA) with the goal to achieve a carbon neutral growth starting in 2021, based on the 2019 carbon emission levels [1]. In October 2021, the International Air Transport Association signed a “Net zero 2050” resolution explaining their strategy to achieve net zero CO₂ emissions by 2050, helped by CORSIA. To do so, 21.2 Gt of CO₂ are to be abated from a ‘business as usual’ trajectory. New technologies should contribute up to 13% by increasing the fuel efficiency, which already increased by 80% in the last 50 years [2]. For instance, traditional aluminium parts have been increasingly replaced by carbon fibre reinforced polymers (CFRP). Indeed, these materials achieve the same mechanical performance with a lower density, increasing the fuel efficiency.

Unfortunately, CFRP are significantly less electrically conductive than aluminium and are, therefore, more subject to damage from lightning strike. Hence, a mesh of copper or aluminium is added on top of the laminates to conduct the lightning current and protect the integrity of the structure. This lightning strike protection (LSP) is very efficient but has drawbacks. It is relatively heavy, up to ~400 g/m², prone to galvanic corrosion since the metal is in contact with the carbon fibres, and, to a lesser extent, difficult to repair.

Aircraft manufacturers, like Bell Textron, the industrial partner in this project, are interested in developing new light, scalable and efficient LSP that could equip, for example, the Bell NEXUS, an electric or hybrid-electric vertical take-off air taxi concept. A painted laminate protected by this LSP should maintain its mechanical properties after a lightning strike test.

The research on LSP significantly increased since the beginning of the 2010s and many alternatives for metallic meshes have been investigated: continuous metallic layers, carbon nanomaterial papers, metal coated carbon fibre, conductive resins, etc. In the meantime, the direct effects of the lightning strike on composite panels were also investigated, and the predominant role of the paint layer in the damage was also observed. Unfortunately, almost no alternatives to the metallic meshes were tested on painted panels and the scalability of the LSP was not often mentioned.

Based on this review, two avenues were considered for this project. The first one was to use silver coated milled carbon fibre (SCCF) to increase the conductivity of the paint layer. The

second one, that is presented in this Master thesis, was to use commercially fabricated nickel coated carbon fibre (NCCF)-based materials as LSP layer. A broad experimental plan was developed to characterise the NCCF-based materials, test them with an in-house lightning strike emulator, investigate the damage and measure their LSP efficiency in comparison to reference panels: unprotected CFRP panels and CFRP panels protected by an expanded copper foil.

This thesis is organised in four chapters. Chapter 2 presents a literature review explaining the lightning strike phenomenon and its interaction with an aircraft, the direct effects of lightning to composite panels and an exhaustive overview of the tested LSP. Chapter 3 describes the broad experimental plan designed to test and understand the behaviours of the NCCF-based and reference materials under the lightning strike. In Chapter 4, the results of the experimental plan are presented, the LSP efficiency of all materials are evaluated, and the different observed damage mechanisms are explained. Finally, the main results are summarised in Chapter 5 and potential future works are described.

This work is the result of a team effort. I worked closely with Jean Langot, a post-doctoral fellow, on the NCCF-based solutions. Anamaria Serbescu, another master's student, and David Brassard, a post-doctoral fellow, investigated the SCCF-based solutions. Kambiz Chizari was project manager. All five of us participated in the test and characterisation of the materials.

CHAPTER 2 REVIEW

In average, each commercial airplane is struck by lightning one time per year [3]. However, aluminium is increasingly replaced by carbon fibre reinforced polymers (CFRP) in aircraft structure. Despite their excellent mechanical performance, these composites suffer considerable damage when struck by lightning. Lightning strike protection (LSP) solutions are thus required for this new generation of aircraft.

Firstly, we will clarify the basics of the lightning strike phenomenon, its interaction with aircraft and the recommended practices of the aerospace industry regarding LSP. Secondly, we will explain the damage caused by lightning strikes on composite structures. Finally, we will describe and categorise the LSP solutions for composites that were published over the years.

2.1 Lightning strikes to aircraft

2.1.1 Natural formation of lightning

2.1.1.1 Electronic avalanche and corona streamers

Electric fields high enough to ionise the air are found in a stormy environment. Above 3 kV/mm under normal atmospheric conditions, electrons gain enough energy to separate from their nuclei, creating electron/ion pairs. These free electrons are then accelerated, colliding with other atoms to create more electron/ion pairs. If the electric field is maintained above a critical value, a runaway phenomenon occurs, the electron avalanche. The plasma formed gathers in the form of corona streamers, which are filaments of cold plasma that can be several metres long [4].

2.1.1.2 Propagation of leaders

These streamers are attached to a common root called stem [5] and point in the same direction. If the electric field increases in this region, the number of streamers will also increase. The region containing these filaments will heat up to 5,000-6,000 K [4], creating a channel of increasingly hot plasma. This channel is called a leader and this phenomenon is the

streamer-leader transition and allows the formation and propagation of a leader at a speed of 10^5 m/s. The electric field needed for a stable propagation of lightning discharge is 750 V/mm, which is lower than the breakdown value.

A distinction between positive and negative leaders is made because of the differences in their structure and propagation, as can be seen in Figure 2.1. A positive leader will propagate continuously as the corona region heats up the front, whereas a negative leader will have a stepped propagation. In this case, the formation starts with a negative corona followed by the apparition of a space leader in the middle of this region. This space leader propagates in both direction until the junction of the two leaders that produces a strong illumination. The process repeats itself inducing this ‘stepped’ effect.

In the case of lightning discharge, it is generally admitted that the leader propagates bidirectionally [4]: a positive leader in the direction of the electric field and a negative one in the other.

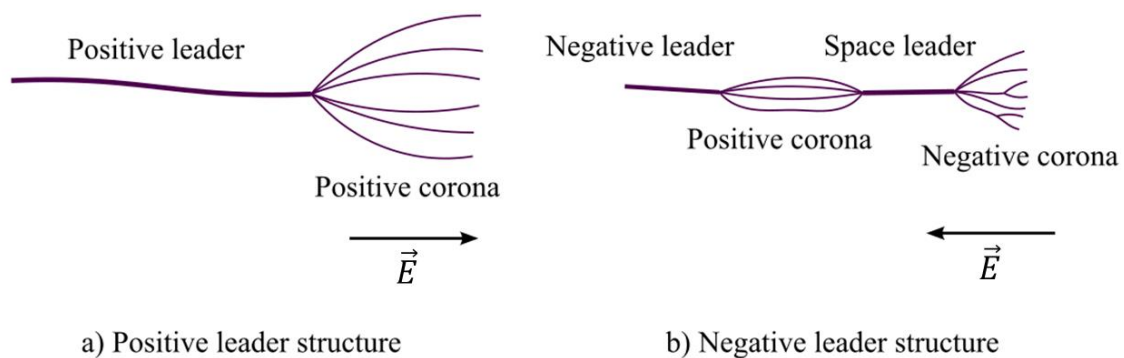


Figure 2.1: a) Positive and b) negative leaders structure and propagation. A positive leader has a continuous propagation, and a negative leader has a stepped propagation.

2.1.1.3 Junction and return arc

When two leaders from oppositely charged regions meet, the two hot plasma channels are joined. This medium is highly conductive in comparison with the surrounding air. Therefore, a high current flows in this plasma channel to balance the two regions of charge: this is the return stroke. The effect of this high current is to rapidly heat the channel previously created by the leaders to 30,000 K [4], violently expanding the gas. This causes a flash visible to the naked eye, as well as a pressure shock wave in the air: the thunder.

The current waveform pattern is the same for each strike: the first current peak is the highest, then a continuous current of 100-400 A appears until the end of the flash. However, leaders from other surrounding charged regions may propagate to the still hot plasma channel, causing new current peaks in the channel. These peaks are called subsequent return strokes.

A distinction between intra-, intercloud (IC) and cloud to ground (CG) flashes and between positive and negative flashes is made because their characteristics and frequency of occurrences are different.

Positive CG are the least frequent (only 10% of the CG flashes) but can be much more severe than negative ones. Indeed, their initial peak current has a median value of 35 kA, up to 250 kA for the 5% more severe strokes (respectively 30 and 80 kA for negative CG). However, negative CG flashes are more subject to subsequent return strokes: between 1 and 24 current peaks are usually recorded, with an average of 3. The subsequent return strokes are generally lower, with a median value of 12 kA. A typical negative CG flash waveform is presented in Figure 2.2, with a high current first return stroke followed by smaller subsequent strokes and a continuous current in between.

IC flashes are known to be less severe than CG flashes with peak currents usually between 20 and 30 kA [6]. Over 50% of all flashes are intracloud [7]. An aircraft is likely to encounter all these types of lightning strikes, releasing each time around 1 GJ of electrostatic energy [8].

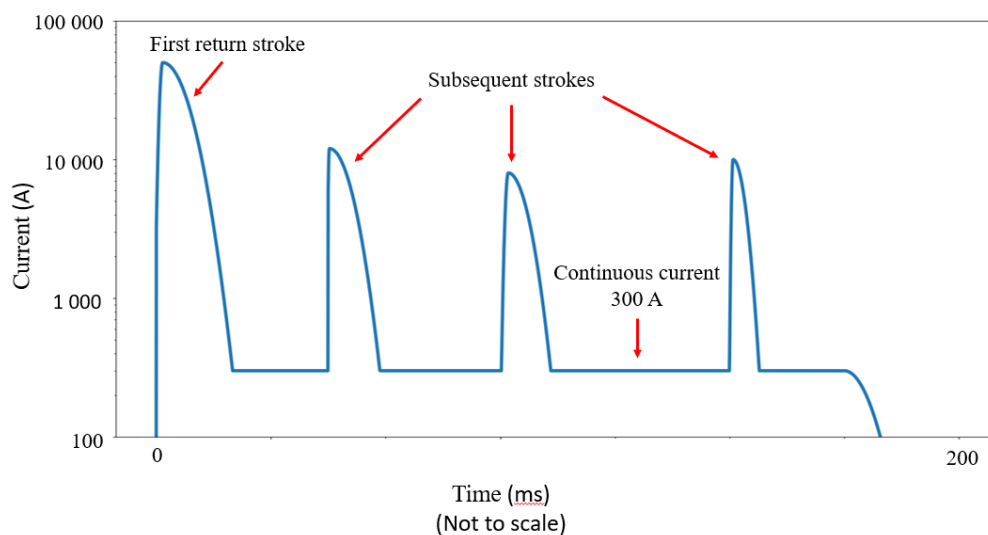


Figure 2.2: Typical waveform of a negative CG flash

2.1.2 Lightning-aircraft interaction

2.1.2.1 Aircraft-initiated and aircraft-intercepted strikes

When an aircraft is in a thunderstorm area, it is at the same potential as the surrounding air. It compresses the equipotential at its extremities (nose, wing tips, fin tips, blade tips...), this phenomenon being more amplified as edges are pointier. This so-called tip effect increases the electric field locally. If the right conditions are met, leaders can then form from these tips and propagate. If leaders from the aircraft connect two pockets of opposite charge, it results in a lightning strike initiated by the aircraft. This process is presented on top of Figure 2.3.a). It is also possible that an aircraft leader joins other naturally occurring leaders that are already formed, allowing the lightning discharge, as shown in Figure 2.3.b).

Two studies [9], [10] from the 1990s used data from tests campaigns carried out in France with a C-160 and in the USA with a CV-580 to understand the difference between these two interactions. They reported that 90% of the lightning strikes measured were initiated by the aircraft.

The lightning current is injected at the entry point, or point of attachment, passes through the aircraft structure and exits through an exit point into another plasma channel. The aircraft replaces a part of the hot plasma channel, but it is not the beginning nor the end of the flash. The aircraft structure must be conductive to be able to carry this high current from the attachment point to the exit point.

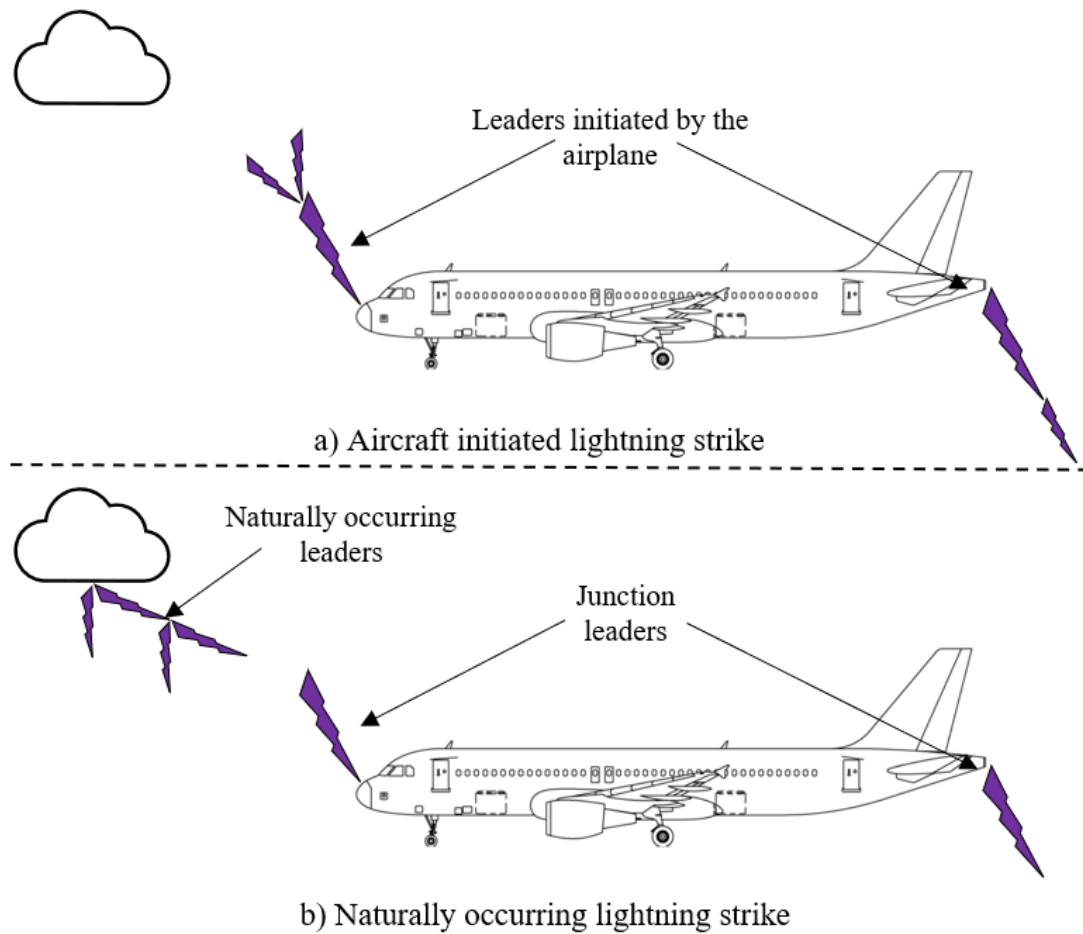


Figure 2.3: Lightning-aircraft interaction: a) Aircraft initiated lightning strike. b) Naturally occurring lightning strike

2.1.2.2 Sweeping effect

As the aircraft is normally in motion when struck by lightning, the plasma channel will tend to lay along the structure. The channel may then re-attach farther along the aircraft structure if the potential difference between the channel and the structure is higher than the critical electric field of the air E_c [12]. Figure 2.4.a) presents this phenomenon with the initial arc in light purple, and the new arc in purple laying along the structure as the air moves around the aircraft.

This re-attachment phenomenon can lead to a sweeping effect on the aircraft surface at both the entry and exit points. The arc will reattach and damage the structure at several points, as shown in Figure 2.4.b). The dwell time, i.e. the time between reattachments, depends on the aircraft surface and the speed of the aircraft [12]. A formula [4] gives the distance between the attachment points:

$$D = \frac{h \times TAS}{v}, \quad (2.1)$$

where h is the aircraft altitude, $v = 150 \text{ km/s}$ the speed of the leader and TAS the aircraft speed relative to the ambient air. This distance, giving us the dwell time, is an important information to predict the amount of energy that will be deposited at each point of the structure.

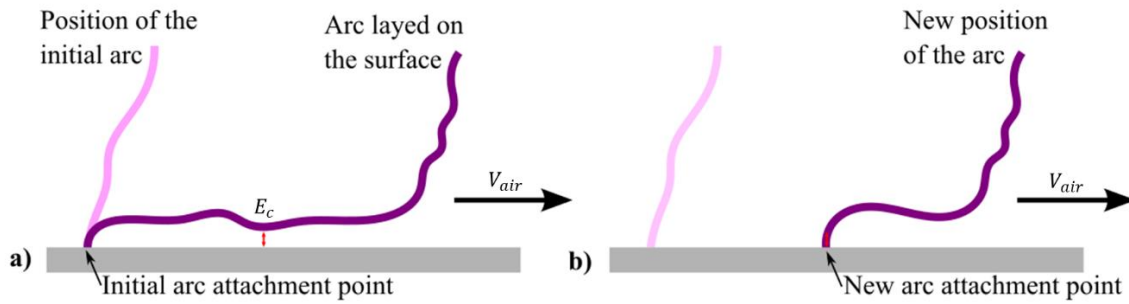


Figure 2.4: Sweeping effect. a) As the air moves around the aircraft with a speed V_{air} , the plasma channel lays on the surface. b) At some point, the electric field is higher than the critical value E_c , and another attachment point is created.

2.1.2.3 Recommended practices for lightning strike protection of aircraft

a) Aircraft zoning

This zoning, described in SAE International Recommended Practice ARP5414 [11], classifies the aircraft into 3 zones that should be adequately protected. Each zone is defined and determined using the same approach as described before. Zone 1 is the area of the initial point of attachment. Therefore, it must be able to withstand the maximum current of the return stroke. Zone 2 is an area where re-attachments are likely to occur, but after the first current peak. Zone 3 is a zone where the probability of attachment and sweep is low, the structure in this zone must only be able to conduct the current. This is the conduction zone.

Zone 1 is further divided into 3 risk levels:

- Zone 1A - First return stroke zone: this is the zone where the first point of attachment is most likely to occur, and this for low flying aircraft ($<1,500 \text{ m}$). The peak currents are higher in this case than higher up in altitude. The length of this zone can be calculated using (2.1), an aircraft velocity of 130 m/s and an altitude of $1,500 \text{ m}$. We get $d_1 = 1.3 \text{ m}$, as shown in Figure 2.5 and Figure 2.6.

- Zone 1B - First return stroke zone with long hang on: if Zone 1A extends till the back edge of the structure, the section at the far back is the Zone 1B. As no sweeping can occur in this zone, the lightning channel will be attached at the same point for all its duration.
- Zone 1C - Transition zone for first return stroke: this is the zone where a return stroke of lower intensity might be found for aircraft flying at medium altitude ($1,500 \text{ m} < h < 3,000 \text{ m}$). The size of this zone can be calculated from (2.1) using an aircraft velocity of 130 m/s and an altitude of 3,000 m. We get $d_2 = 2.6 \text{ m}$, as shown in Figure 2.5 and Figure 2.6..

Zone 2 is divided into two risk levels:

- Zone 2A – Swept stroke zone: this zone is located after Zone 1C. Zone 2A generally covers most of the aircraft structure in terms of lightning protected area. On a Boeing 787, the Zone 2A represents around $2,500 \text{ m}^2$ while the Zone 1 represents less than 200 m^2 (computation made with the recommended practice and the Boeing 787 dimensions [13]).
- Zone 2B – Swept stroke zone with long hang on: if Zone 2A extends till the back edge of the structure, the section at the far back is the Zone 2B.

Based on these descriptions, a zoning of each aircraft types is made to determine the parts of the structure at risk. Figure 2.5 shows the zoning of a traditional commercial airplane. The wing tip and the nose are in Zone 1. The values of d_1 and d_2 were given above. A small portion near the wing tip is in Zone 2. The fuselage and a portion on the wing around the propulsor are also in Zone 2 but are not represented in this figure. Figure 2.6 shows the zoning of a helicopter with a horizontal stabiliser. The tip of the rotors blades and the nose are considered in Zone 1. The tailfin and the stabiliser are also considered in Zone 1, as they would on an airplane. The landing gear and the centre of the rotor are considered in Zone 1B because an arc initially attached at these points would not be able to sweep the structure. The rest of the rotors blades and the bottom of the structure is considered in Zone 2.

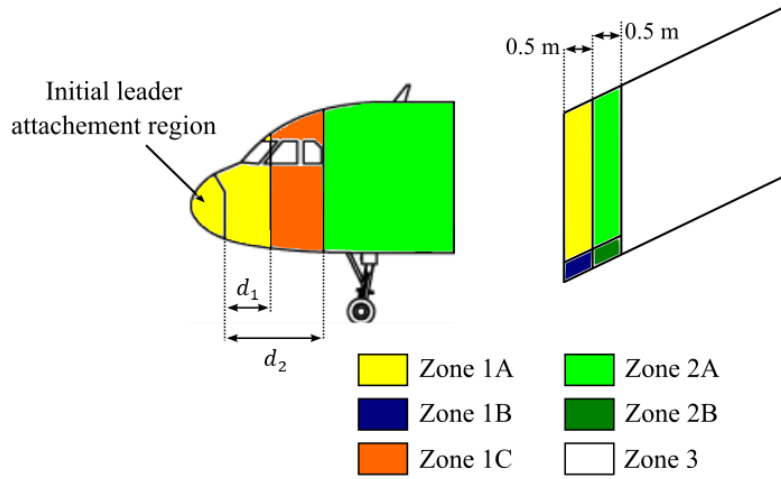


Figure 2.5: Examples of zoning on the nose and the wingtips of an airplane.

Length of Zone 1A: $d_1 = 1.3$ m. Length of Zone 1C: $d_2 = 2.6$ m [11]

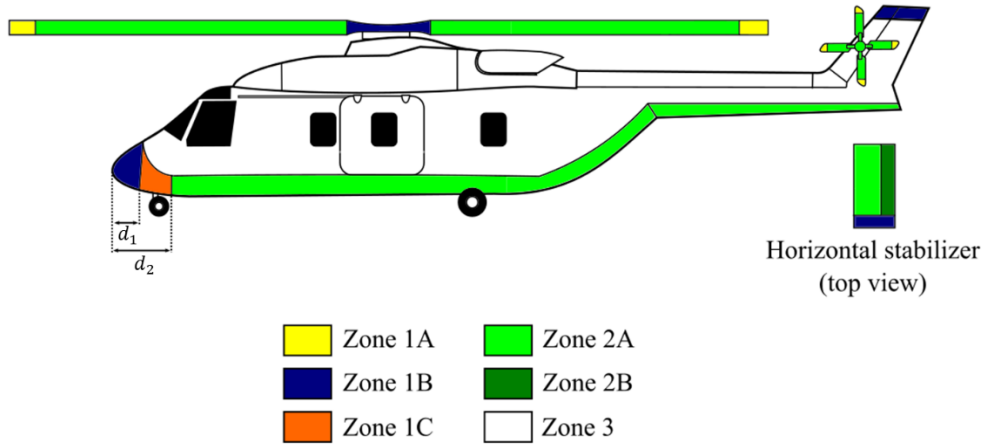


Figure 2.6: Zoning of a helicopter with horizontal stabilizer.

Length of Zone 1A: $d_1 = 1.3$ m. Length of Zone 1C: $d_2 = 2.6$ m [11]

b) Current waveform

Finally, to certify the different zones of the aircraft structure, standardised current waveforms have been introduced in the SAE International Recommended Practice ARP5412 [7]. They are defined by their peak current, duration, action integral and/or electric charge transfer, as shown in Figure 2.7.

$$\text{Electric charge transfer} = \int i(t)dt \text{ in Coulomb (C)}$$

$$\text{Action integral} = \int [i(t)]^2 dt \text{ in } A^2 \cdot s = J/\Omega$$

The waveform A represents the first return stroke. It has a peak current of 200 kA, a duration of less than 500 μ s and an action integral of 2×10^6 A²/s. The waveform B represents the transition from peak current to continuous current. It lasts less than 5 ms, with a charge transfer of 10 C and an average amplitude of 2 kA. The waveform C represents the continuous current that is set up at the end of the flash. Its amplitude is between 200 and 800 A, its duration between 0.25 and 1 s for a charge transfer of 200 C. Finally, the waveform D represents a subsequent return stroke. Its amplitude is 100 kA, its duration less than 500 μ s and its action integral $4 \times$ lower than the waveform A: 0.25×10^6 A²/s. The properties of all these waveforms are summarised in Figure 2.7.

A and D waveforms are also characterised by the time t_1 to reach the peak, and the time t_2 for the current to reach half of the peak value. These waveforms are generated by various lightning emulators to test and certify aeronautical structures.

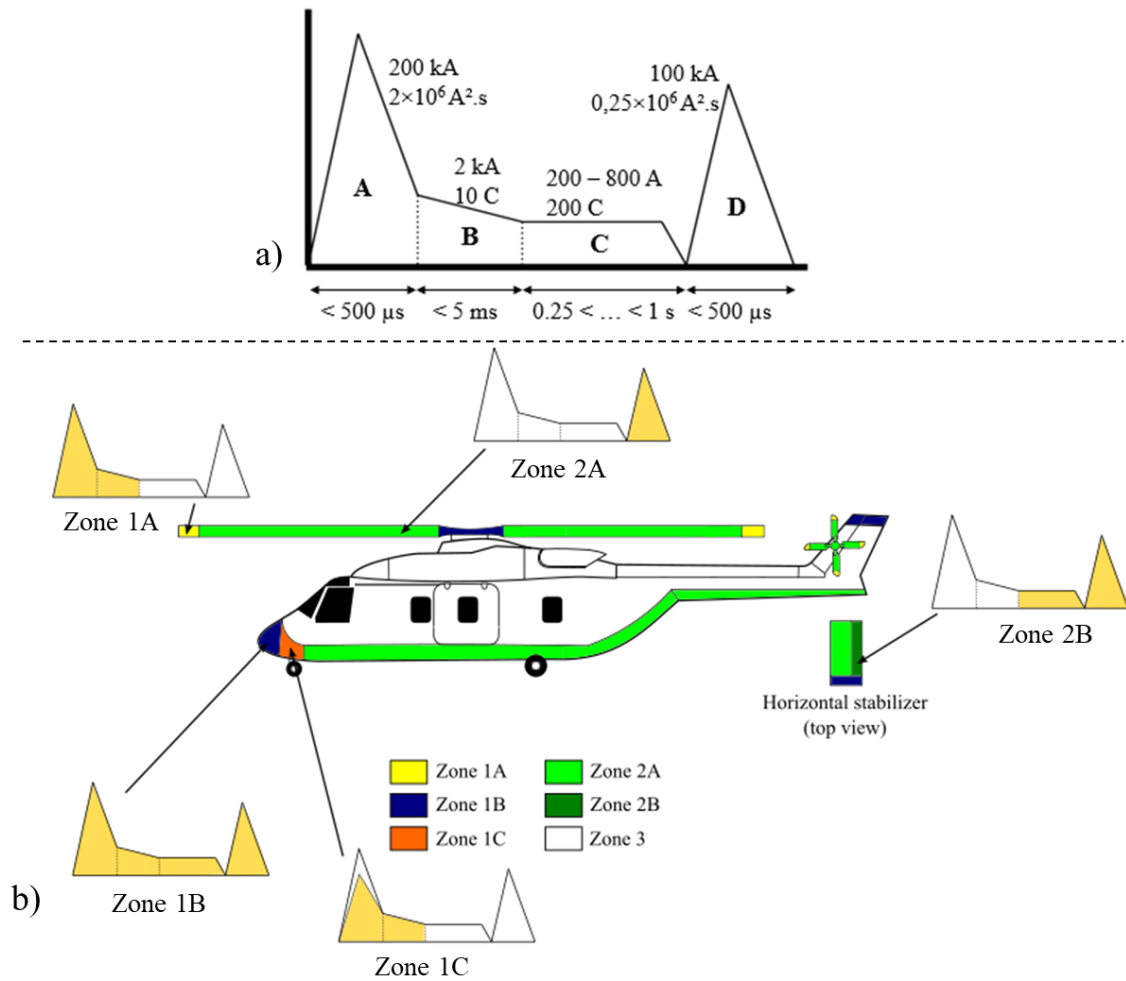


Figure 2.7: a) Lightning current waveform parameters. b) Lightning current waveform and zoning link. A_h is a current reduced A waveform used to represent the Zone 1C.

2.2 Damage to carbon fibre reinforced polymers

Until recently, aircraft were designed with a structure mostly made of aluminium. The Boeing 777 uses 50% aluminium and 12% composites in its structure weight. Thanks to its high electrical conductivity, the structure also served as LSP and as shielding against electromagnetic interference (EMI). However, in more recent aircraft (Airbus 220, Boeing 787), to reduce the weight of the aircraft, the aluminium structure was replaced by CFRP (50% composites and 20% aluminium for the Boeing 787). Indeed, their specific strength and specific modulus is higher than all metals (respectively $7\times$ and $4\times$ than aluminium [1]), allowing much lighter structures with the same mechanical performances, but their electrical conductivity is lower by several order of magnitude.

Metals are the most conductive material at room temperature. For example, aluminium has an electrical conductivity of $\sigma_{Al} = 3.77 \times 10^7$ S/m [15]. Carbon fibres (CF) are also good conductors, but their properties are anisotropic. In the fibres direction, the conductivity is 2×10^5 S/m, while in the transverse direction it is limited to 3.3×10^2 S/m. The resin, most of the time epoxy, is an insulating material. CFRP have thus a lower electrical conductivity than CF alone. In the fibres direction, the electrical conductivity is around $10^3 - 10^4$ S/m close to that of CF, but in the through-thickness direction it is much lower, between $10^{-3} - 10^0$ S/m, because the different fibre plies are separated by an insulating resin layer [16]–[19]. Generally, good electrical conductors are good thermal conductors [20] because both phenomena rely on the presence of free or easily mobilised electrons to achieve the conduction.

Thus, replacing the aluminium structure by CFRP reduces the weight of the aircraft but makes it more susceptible to lightning strike damage. We will now detail the lightning current path in the aircraft structure and see the different damage mechanisms of composite materials subjected to lightning strikes.

2.2.1 Direct effects

The combination of the stresses from the plasma channel and the effect of the current propagating in the structure may cause important damage to the structure. They are categorised by the SAE Aerospace as : dielectric puncture, arc root thermal damage and

heating effects, acoustic shockwave damage and magnetic force [21]. Figure 2.8 presents these mechanical, thermal, and electrical constraints on a CFRP struck by lightning.

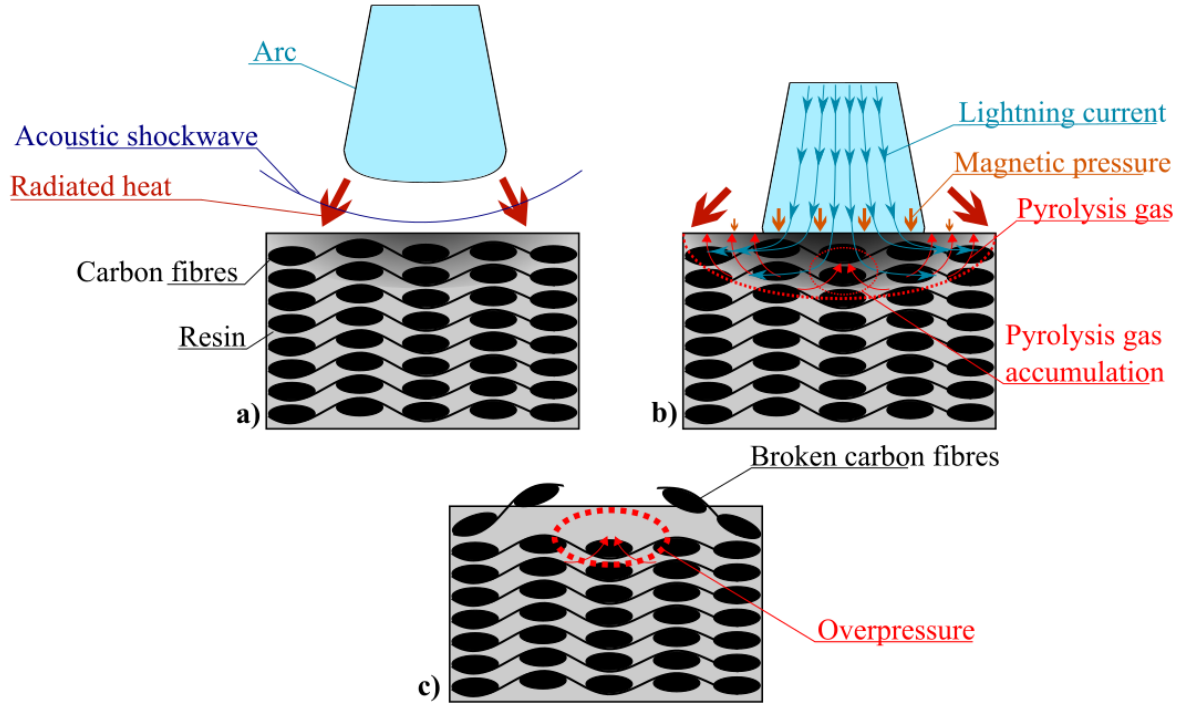


Figure 2.8: Thermal, electrical and mechanical constraints at the attachment point on a CFRP. a) Plasma channel approaching the composite structure. b) Effect of the current propagation in the laminate. c) Damaged post-lightning strike due to increased internal pressure.

2.2.1.1 Mechanical and thermal stresses from the plasma channel

When the lightning leader approaches the structure at high speed, it creates an acoustic shockwave that hits the structure around the point of attachment. A rough estimate of its amplitude is 10 MPa [22]. A magnetic pressure is also applied on the structure around the point of attachment. Indeed, the current propagating in the plasma channel generates an orthoradial magnetic field \vec{B} . Inside the structure, the current is conducted radially from the point of attachment. The Laplace force is applied by the magnetic field on the conducting network and point in direction of the laminate. Hence, the magnetic pressure field expression for an infinite plane is [22]:

$$p(r, t) = \begin{cases} \frac{\mu_0 I^2(t)}{4\pi^2 R_c^2}, & r < R_c \\ \frac{\mu_0 I^2(t)}{4\pi^2 r^2}, & r \geq R_c \end{cases}, \quad (2.2)$$

where r is the radial distance to the attachment point, $\mu_0 = 4\pi \times 10^{-7}$ H/m the magnetic permeability of free space, R_c [m] the radius of the plasma channel and $I(t)$ [A] the intensity of the current. A rough estimate of its amplitude for a 200 kA discharge and a arc root radius of 5 mm is 50 MPa [22]. The significance of the heat transmitted by the plasma channel via radiation and conduction in comparison with the heat released by the current is still debated [23].

2.2.1.2 Effect of current propagation in the structure

The lightning current takes the most conductive path to the exit point. If the structure is made of CFRP, most of the current will flow through the fibres. Thus, when current is injected into the top of the structure, it must pass through the thin insulating layer to reach the fibres.

a) Penetration of the top insulating layer

The thin insulating layer vaporises under the effect of the heat from the plasma channel, or the heat released by the Joule effect, i.e. by the passage of the current in a medium of non-zero electrical resistance. The insulating layer can also be punctured by dielectric breakdown. The breakdown has the effect of ionising a path in the insulator to allow current to flow through it, connecting the plasma channel to the conductive carbon fibres.

When the first layer of carbon fibres is reached by the current, the electrical conduction happens mainly in the plane along the fibres, as described by the current streamlines in Figure 2.8. The conduction is accompanied by an increase in the fibres and resin temperature due to the Joule effect, and the temperature evolves according to the heat equation:

$$\rho C_p \frac{\partial T}{\partial t} - \vec{\nabla} \cdot (\underline{\underline{k}} \cdot \vec{\nabla} T) = Q_J, \quad (2.3)$$

where T [K] is the temperature, ρ [g/m³] is the density, C_p [J/(kg.K)] the specific heat and $\underline{\underline{k}}$ [W/(m.K)] the thermal conductivity tensor. Q_J [W/m] is the Joule heating source:

$$Q_J = \vec{J} \cdot \vec{E}, \quad (2.4)$$

where \vec{J} [A/m²] is the electric current density tensor and \vec{E} [V/m] is the electric field tensor.

Yet, for a material with an electrical conductivity tensor $\underline{\underline{\sigma}} = \underline{\underline{\rho}}^{-1}$ (electrical resistivity), we have:

$$\vec{J} = \underline{\underline{\sigma}} \cdot \vec{E} \Leftrightarrow \vec{E} = \underline{\underline{\rho}} \cdot \vec{J}. \quad (2.5)$$

Thus, the more conductive the material, the lesser the dissipated power in the form of Joule heating. That is if we consider the lightning channel as a current source. C_p , \underline{k} and $\underline{\underline{\sigma}}$ are temperature dependent. For metals, \underline{k} and $\underline{\underline{\sigma}}$ decrease with increasing temperatures. For semi-conductors, like carbon fibres, \underline{k} and $\underline{\underline{\sigma}}$ increase with increasing temperatures [24].

The temperature increase leads to the degradation of the resin in the first instance and the sublimation of the carbon fibres in the second.

b) Resin degradation and fibres sublimation

For epoxies, the first step is the glass transition at $T_g = 75$ °C, which is a reversible transition that changes the solid state of the resin into a viscous state. The pyrolysis of the matrix starts between 225 and 425 °C. This thermal decomposition without oxygen will decompose the resin molecules in smaller ones producing gas (pyrolysates), liquid (tar) and solid (char) compounds. In epoxies, between 5 and 20% mass of char will be produced, resulting in an increase of the porosity. The gas is at first stored in the pores and then released at an increasing speed due to the increase in the porosity. Some compounds ignite at the contact of oxygen and add another source of heat. The porosity of the composites being high at this stage, oxygen diffuses in the laminates and oxidises the char and the carbon fibres at ~345 °C degrading their properties [25]. However, this last process is rather slow and might not take place during the lightning strike test. The temperature keeps increasing due to Joule heating and the carbon fibres sublime at 3,650 °C, inducing carbon fibre breakage.

c) Overpressures

Some current can flow into the lower plies if there is contact between the CF or via dielectric breakdown. As explained before, the resin and the fibre decomposition release hot gases that

can be stored below the other plies or within the pores of the matrix. These pockets of trapped gas increase the internal pressure and create overpressures that can cause debonding between the fibres and the matrix, fibre breakage, or even delamination, i.e. the detachment of the carbon fibre plies, as shown in Figure 2.8.c). The effect of overpressures is more remarkable on painted panels.

In 2010, *Hirano et al.* [26] were the firsts to describe and categorise the three damage modes of carbon fibre reinforced polymers. Each one was highly correlated with a lightning current parameter:

- Fibre damage with peak current,
- Resin deterioration with the electric charge transfer,
- Delamination with the action integral.

The damage depth is also governed by the peak current. These results were confirmed by *Sun et al.* [27] that tested their CFRP with combinations of standardised waveforms. The high current impulses (A or D) had a bigger impact on the damage depth and area than longer but lower impulses (C).

2.2.1.3 Effect of paint

On the aircraft structure we find a finishing layer that protects the structure from the outside environment. The layer is an electrical insulator that has a huge influence on the lightning strike resistance of the structure. Any structure should therefore be tested with a finishing layer to validate its lightning strike behaviour. *Bigand et al.* [28] and *Kawakami et al.* [29] reported the tests of panels protected by expanded copper foil (ECF, the most common solution in the aeronautical industry) and coated with different layers of paint subjected to lightning strikes. The nonpainted panel showed very little damage. As the thickness of the paint increased, so did the surface and the damage depth, as is shown in Figure 2.9. *Moupfouma* [30] tested aluminium panels with D, B and C waveforms. The panels had different paint thickness and the C waveform lasted between 5 and 100 ms (which is 5 to 100× shorter than the recommended practice for a C waveform of 400 A). He observed that for short durations, increasing the paint thickness helped protecting the aluminium panels, but

this effect was not significant for longer durations (above 40 ms). In this case, increasing the paint thickness increased the damage depth. The damage area was not reported.

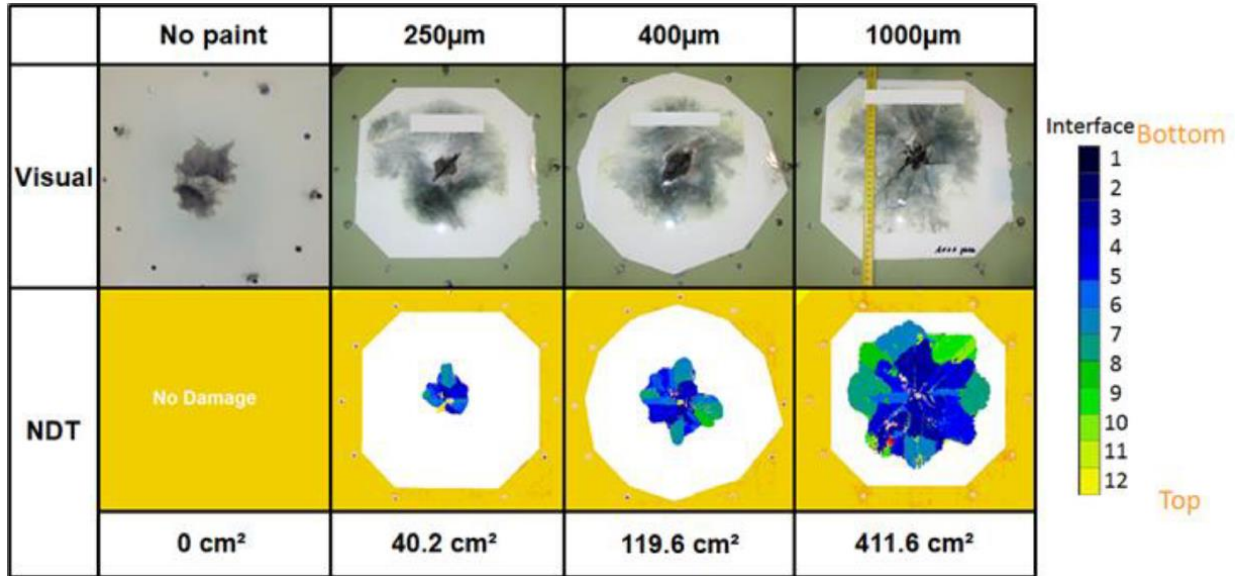


Figure 2.9: Evolution of the lightning damage on a 13 plies CFRP protected by an ECF (195 g/m²) with different paint thickness. A waveform D was used for the tests [28].

An explanation for the results reported in the literature could be that the insulating layer has the effect of constraining the arc root radius of the plasma channel. This phenomenon was observed by *Chemartin et al.* [12] for waveforms A and D. They put an aluminium panel with or without paint under a 100 kA arc and observed the radius of the damaged zone. The radius of the damaged zone exceeded 2 cm for the nonpainted but was limited to 0.5 cm for the painted one. However, for the waveform C, the constraining effect of the paint was only observed during the first 10 ms in simulation, while the waveform total duration is longer than 250 ms. The same phenomenon was observed by *Martins* [31] on aluminium panels. The reduced arc root radius induces a higher current density at the point of attachment. The Joule heating is thus more intense according to equation (2.4). Therefore, it is easier for the lightning current to penetrate the lightning protection layer and the first plies of the laminate. Hot gases are released in deeper layers, creating overpressures and bigger damage than with a lower current density. The insulating paint layer also favours the accumulation of hot gases and increases the probability of overpressures.

The damage mechanisms being now explained for CFRP without and with a finishing layer, we now explain the influence of the different parameters of the injected current on the damage.

2.2.2 Indirect effects

The indirect effects of a lightning strike result from the interaction of the aircraft and the electromagnetic (EM) field radiated by the lightning current. The EM field penetrates the conductive structure with an exponentially decreasing amplitude and passes through apertures (non-conductive parts of the structure like windows) without attenuation, inducing currents and voltages in the structure and equipment. Currents also penetrate via wires connecting internal elements with external ones, like antennas. These induced currents might damage internal equipment [21].

Having a conductive structure or a conductive layer on top of the structures limits the EM field penetration in the structure. Indeed, the skin depth, the characteristic penetration depth of the EM field, is proportional to the inverse of the square root of the electrical conductivity. A conductive layer will reduce the likeliness of EM interference (EMI). Research on LSP is often coupled with the research on EMI shielding.

2.3 Lightning strike protection

CFRP are vulnerable to lightning strikes, hence the necessity to add a LSP layer on top of them when they are used in the structure. The solution chosen for most composite aircraft is to add a metal mesh embedded in resin on top of CFRP. The metals used are mostly copper and aluminium, which are not as conductive as silver but cheaper [32]. The mesh, which looks like a grid, is either made of woven metal wires or perforated metal foils. Solid metal foils are perforated while being stretched to produce the diamond shape pattern presented in Figure 2.10. They are then flattened to achieve the required thickness. An expanded foil has a higher electrical conductivity than a wire mesh because it suppresses all contact resistances within the wire network. The five parameters characterising an expanded foil are its material, the strand width and thickness, the short width of the diamond (SWD) and the long width of the diamond (LWD). However, its areal density is the most used parameter to describe an expanded foil.

If we consider all the materials necessary for its integration (foil + adhesive), this protection becomes rather heavy. 3M offers expanded copper foils (ECF) between 137 and 292 g/m² [33]. The heavier the foil, the higher its resistance to lightning strikes. But the heavier the foil, the higher the fuel consumption. Metallic foils also present risks of galvanic corrosion [34] as the metal can be in contact with the carbon fibres, that have a different galvanic potential. That corrosion might damage the mesh. Thus, many alternatives to expanded foils have been actively investigated over the last years.

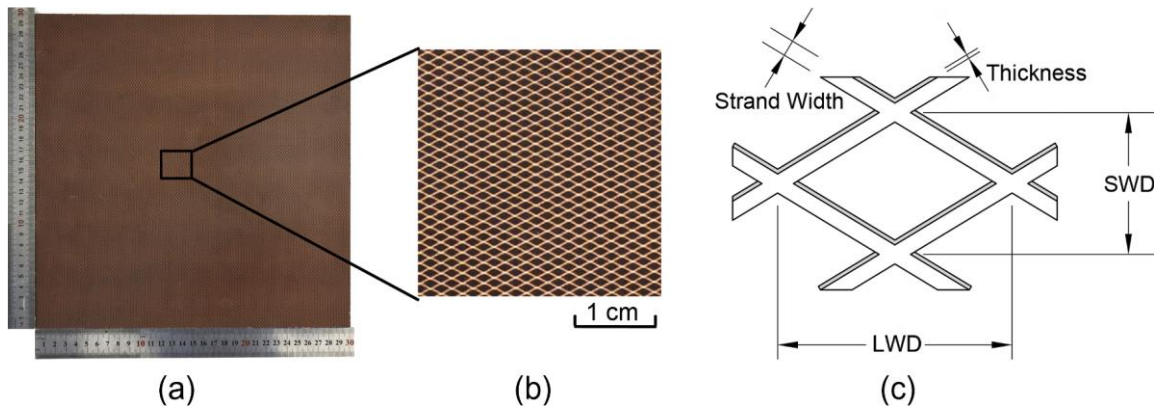


Figure 2.10: Expanded copper foil details. This ECF has a thickness of 0.076 mm, a strand width of 0.1778 mm, a short width of the diamond of 1.33 mm and a long width of the diamond of 3.18 mm. Its areal density is 141.6 g/m² [35].

The review presented below regroups all the published articles on LSP solutions for CFRP that were tested under a lightning strike emulator. As shown in Figure 2.11, the research efforts started around 2010 with the publication of at least 5 solutions per year since then, except 2012, 2014 and 2015. The years before COVID-19 were the most prolific, with 8 articles published in average in 2017, 2018 and 2019. Reviews on LSP technologies were published by *Gagné and Therriault* [32] in 2014 and by *Kumar et al.* [36] in 2020, as well as one conference paper in 2016 [37]. *Kumar et al.* review is the most complete one so far. Two reviews on lightning strike test simulations were also published in 2017 [38] and 2021 [23].

LSP solutions are grouped according to their position in the laminate (on top or inside), their type and the material used (metallic, non-metallic and hybrid). Only the most relevant ones are presented in this chapter, the rest are presented in the Appendix.

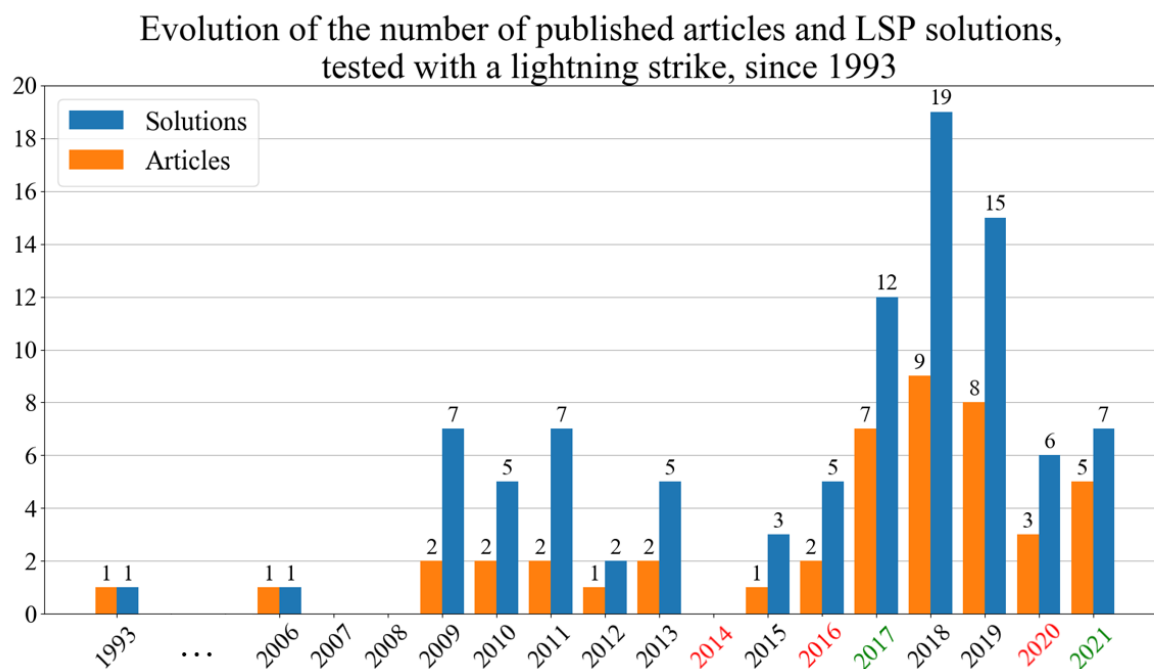


Figure 2.11: Evolution of the number of published articles and LSP solutions, tested with a lightning strike, since 1993. In red, the year during which a review on LSP solutions was published. In green, the year during which a review on lightning strike test simulations was published.

2.3.1 On top of the laminate

The LSP located on the top of the CFRP are meant to prevent the lightning current to penetrate. The first and most investigated type is a conductive layer that will be damaged during the lightning strike, sacrificing itself to protect the CFRP. The second type has an insulating layer incorporated between the sacrificial conductive layer and the CFRP.

2.3.1.1 Sacrificial layer

a) Metallic

Mesh

As metal meshes are already used on commercial aircraft, research on them is now focusing on details of their use or possible improvements. *Kawakami and Feraboli*. [29] studied how the quality of repair of an ECF affected the LSP efficiency. They artificially damaged protected CFRP and repaired them in two different ways. The ‘bad’ way was to leave a 3.18 mm gap between the replacement ECF and the existing one, while the ‘good’ way was to

overlap the two meshes by 3.18 mm. After testing at 80 kA, the 'right' way retained 100% of the flexural strength, like the pristine ECF, while the 'wrong' way retained only 61%. *Guo et al.* [35] analysed how the anisotropic electrical conductivity of ECF or expanded aluminium foil (EAF) could be used to optimise LSP for different areas of the aircraft. Indeed, they noticed that the damage to the mesh took the shape of a diamond with the same orientation as the mesh pattern, the damage spreading in the LWD direction. Zones 1 and 3 being, respectively, the attachment and conduction zones, the mesh used in these zones should be oriented in the direction of current conduction to favour current evacuation. This orientation is presented in Figure 2.12.a). For Zone 2, which is the zone in where most reattachment take place, the mesh should be oriented perpendicular to the direction of sweeping, as presented in Figure 2.12.b). In this way, re-attachment would less likely occur in an already damaged area.

Other metallic solutions were considered as sacrificial conductive layer, but with much lower efficiency than metallic meshes:

- nanoparticles dispersed in the finishing layer [39],
- silver [39] or copper [40] electroless deposition on the laminate surface,
- aluminium [41]–[43] or tin and copper-tin [39], [44] sprays on the laminate surface.

b) Non-metallic

Most non-metallic sacrificial layers are based on carbon nanomaterials: graphene or single or multi-wall carbon nanotubes (SW- or MW CnT) because of their high electrical conductivity. These materials are integrated in the form of bucky paper (BP) with a thickness varying from a few tens to a few hundred micrometres. Conductive adhesive or even insulating glass fibres reinforced polymers (GFRP) were also considered.

Graphene

Zhang et al. [45] have fabricated graphene films with thicknesses ranging from 22.9 to 140 μm and through-thickness conductivities ranging from 1.76×10^5 to 1.32×10^4 S/m. The 100 μm thick and 200 g/m² film was chosen for lightning testing as it was the best compromise between flexibility, stability, and conductivity. The addition of this graphene film on a CFRP reduced the damage area by 94% and the damage volume by 96% compared to the pristine CFRP. Shortly afterwards, *Wang et al.* [46] made an epoxy resin film

containing Reduced Graphene Oxide (RGO) in different amounts (0-0.2 g) using a percolation assisted resin film infusion method. As the resin flow was directed through the thickness, and not from the side as usual, a more uniform distribution of the RGO on the surface was expected. The percolation threshold was reached for 0.05 g of RGO with a conductivity of 3.70 S/m and a thickness of 0.03 mm. The material was tested with a 40 kA lightning strike and allowed a limitation of the damage to the first two layers (0.3 mm) of the laminate, while the conventional CFRP was affected on 3 or 4 layers (0.7 mm). In addition, the retention of flexural strength increased from 43.9% to 76.8% for a coating of 30.6 g/m² only.

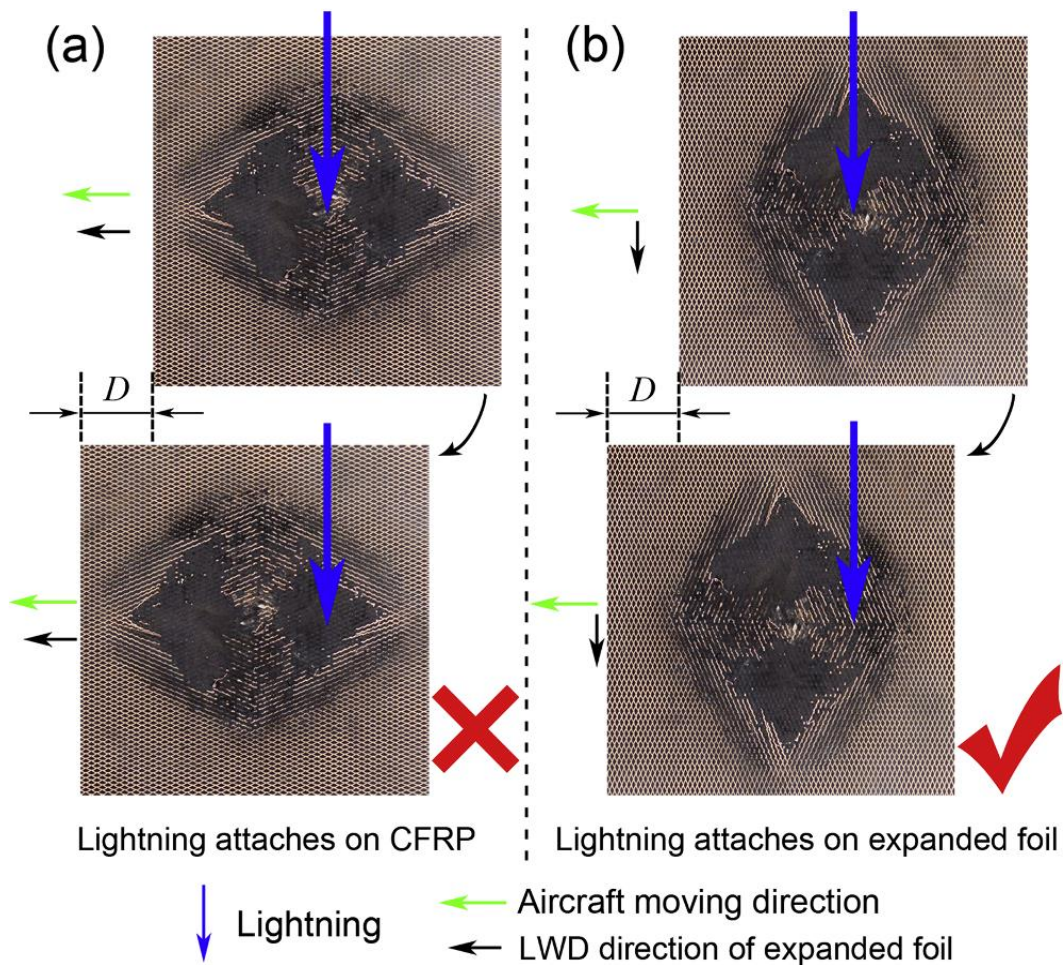


Figure 2.12: Recommended disposition of the ECF in swept stroke zone. (a) LWD direction is parallel to the aircraft moving direction, the reattachment is thus likely to occur on a damaged section. (b) LWD is perpendicular to the aircraft moving direction, the reattachment is thus less likely to occur on a damaged section.

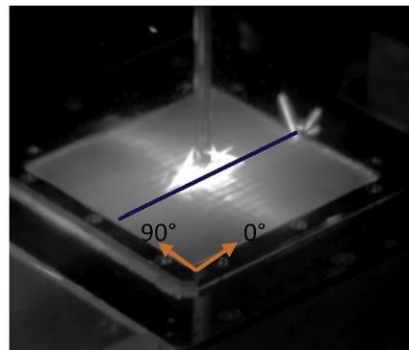
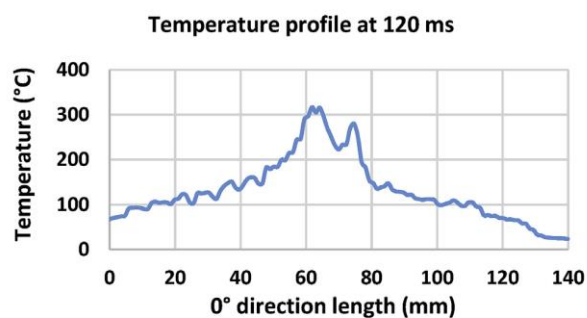
The value of D is calculated using equation (2.1) [35].

Conductive adhesive

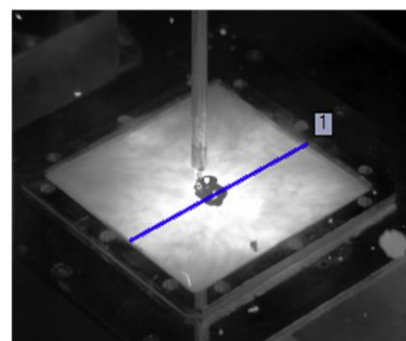
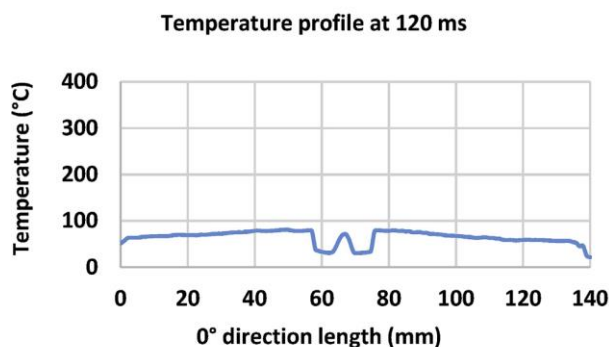
Kumar et al. [17] applied an adhesive made from a conductive polymer, polyaniline (PANI). Dodecylbenzenesulfonic acid (DBSA)-doped PANI complex was prepared and incorporated in a thermosetting polymer, divinylbenzene (DVB). This adhesive had a thickness between 0.25 and 0.4 mm, and an aerial density of around 357 g/m² (1-1.1 g/cm³). The laminate was painted and then tested under a 100 kA discharge. The adhesive increased the flexural strength by 14.2% before the lightning tests and, more importantly, retained 99% of this strength after the tests, whereas the unprotected CFRP retained only 36.6%. This efficiency was explained by the excellent thermal stability of the PANI layer. As shown in Figure 2.13.(a), the maximum temperature, of the pristine CFRP, 120 ms after the lightning strike, was measured above 300 °C, the degradation onset temperature of the resin. Therefore, thermal damage were expected for this laminate. As shown in Figure 2.13.(b), the maximum temperature of the PANI layer was measured at 80°C. This low heat generation was due to the highly isotropic electrical conductivity of 100 S/m and the high thermal stability of the PANI layer that decomposes at high temperature. The temperature profile in the middle of the panel in Figure 2.13.(b) was explained by the difference in temperature between the PANI layer and the CF layer below.

Despite their relatively high electrical conductivity, SW and MW CnT papers alone were not yet able to significantly protect the CFRP from lightning damage. RGO provided good results with a small added mass. Conductive PANI adhesive had a great LSP efficiency on a painted CFRP panel, with no improvement in the added mass in comparison with standard ECF. The PANI adhesive is, so far, the only published alternative to ECF for painted panels.

Single-wall (SW) [47]–[49] or multi-wall (MW) [50], [51], [19] Carbone nanotube (CnT) papers were also considered as sacrificial layers, as well as glass fibres fabrics [52].



(a) Unprotected CFRP struck with 40 kA lightning



(b) PANI-Layer protected CFRP struck with 100 kA lightning

Figure 2.13: Temperature profiles of the struck panels after 120 ms. (a) Pristine CFRP panel. (b) PANI protected panels. The epoxy degradation onset temperature is around 300 °C [17].

c) Hybrid

Carbon materials are not able to protect the laminate alone, but their high specific electrical conductivity encourages their use combined with that of metals. Carbonous papers can be enriched with metallic nanoparticles. Carbon nanomaterials or carbon fibres can also be coated with metal, providing a strong yet conductive backbone. Nylon was also considered to replace carbon. Silver and nickel are the two most used metals in these studies.

Spray of metal coated carbon nanomaterial

Chakravarthi et al. [53] coated SWCnT with nickel by electroless plating and sprayed it onto the first carbon fibre ply before resin infusion. The addition of 4 wt% of Ni-SWCnT reduced the surface resistivity by 8 orders of magnitude. After a test with the three standard waveforms D, B and C (DBC test), the fibres were damaged over an area of 517 mm² for the protected laminate compared to 3,285 mm² for the pristine CFRP.

Rajesh et al. [39] also tested silver coated carbon nanofibres (CnF) impregnated in an epoxy film. This 2.4 g/m² solution with a thickness of 8 to 10 µm had poor results in lightning strike tests at 40 kA with a damage area of 2,758 mm² and a depth of 1.31 mm, much worse than pristine CFRP (2139 mm² and 0.83 mm). The same process was used to manufacture the film tested by *Cauchy et al.*[54]. This 28 g/m² coating was tested by a 15 kA lightning strike after which no damage to the laminate plies was noticed.

Metal coated nonwoven carbon fibre paper

In 2006, *Haynes et al.* [55] considered a nonwoven of nickel coated carbon fibre (NCCF). This 100 g/m² solution was painted and tested by a Zone 1A (ABC) lightning strike. No structural damage or delamination was reported, like for the solution using an EAF. In 2019, *Guo et al.* [56] tested nonwoven NCCF weighing 34 (N1) and 70 g/m² (N2) with waveforms C and D. In both cases, N2 was more effective than ECF. Figure 2.14 shows views of the panels after the waveform D. The CFRP panel (a) suffered the most severe damage with fibre breakage, ply lift and resin decomposition on a 75 mm diameter area. The ECF (b) protected the CFRP, but the foil was vaporised on a large area. N1 (c) did not fully protect the CFRP as the first CF layer, oriented at 45°, was damaged on a 30 mm diameter area. Finally, N2 (d) suppressed the damage on the CFRP surface and on the LSP layer. For the waveform D, N2 retained 98.33% of its flexural strength while ECF retained only 91.79%. These very good performances are explained by the high electrical conductivity of nickel, 1.44×10^7 S/m, and carbon fibres and the good ablation resistance of the paper. Indeed, even if the nickel evaporates due to the Joule effect, the carbon fibre can take over the electrical conduction and absorbs a large amount of energy before breaking. After lightning tests, the fibre network is practically intact.

In the same year *Zhang et al.* [57] tested a similar solution, replacing the nickel with silver. The 150 g/m² fabric was struck by a waveform D. The damage were limited to an area of 1,660 mm² and a depth of 0.20 mm, a reduction of 66% and 92% respectively compared to pristine CFRP. Based on the results from *Haynes et al.*, *Guo et al.* and *Zhang et al.*, it seems that silver coated CF nonwoven are less efficient than nickel coated ones.

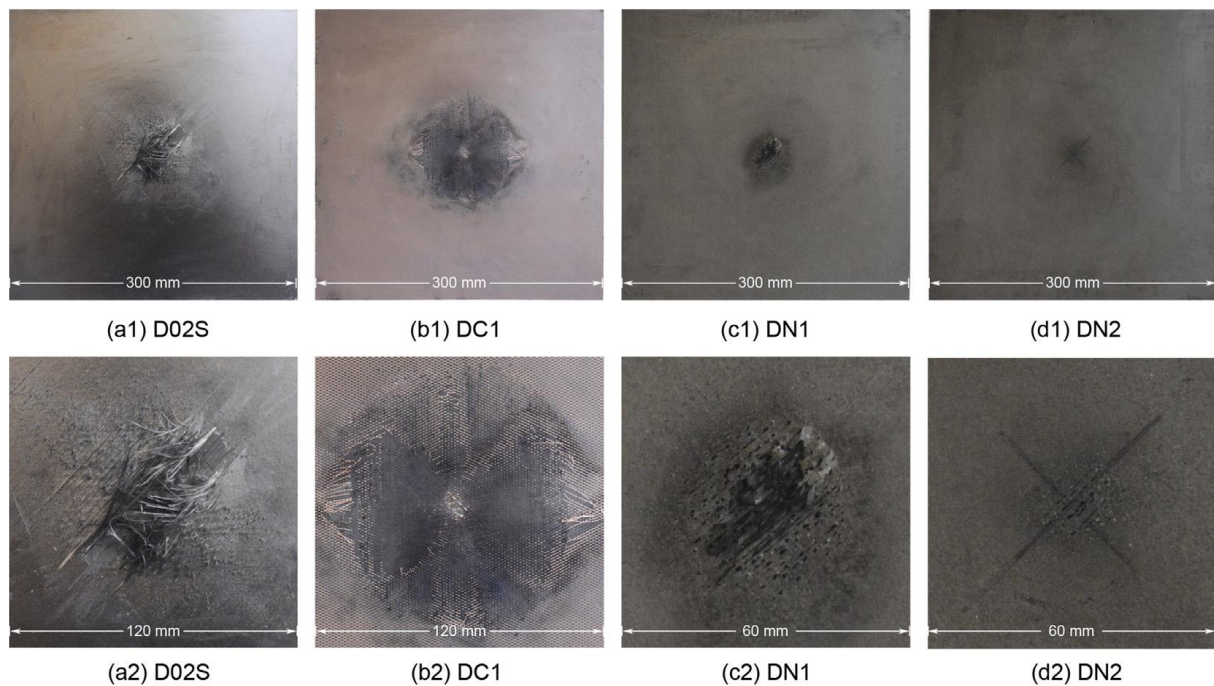


Figure 2.14: Views of the laminates after lightning strike with a waveform D. (a) Pristine CFRP. (b) ECF-protected CFRP. (c) N1 (34 g/m²) protected CFRP. (d) N2 (70 g/m²) protected CFRP [56].

Metal coated carbon fibre woven ply

In 1993, *Henn et al.* [58] described the damage to composite panels containing 9 conventional plies of woven carbon fibres and a final ply of woven (NCCF). The nickel was deposited by electroless deposition, and the ply contained 190 g/m² of nickel or 47% of the total weight. After testing at 200 kA, the three specimens tested were not perforated and the damage area was smaller than for unprotected CFRP. However, the authors believe that improvements are needed, particularly regarding the nickel deposition, to better protect the composite structure. In 2009, *Mall et al.* [59] used a 12k NCCF woven fabric as a basis for five different LSP. It was used alone, with NinS or with three types of SWCnT paper. The CnT were either aligned by a magnetic field, randomly oriented, or mixed with vapor-grown carbon fibres. The resulting panels were struck by a 100 kA current. No solution was able to retain more than 70% of the ultimate compressive strength after the lightning tests. The NCCF+NinS combination retained only 25% of this property and the NCCF woven fabric alone 50%. The randomly oriented SWCnT paper and NCCF combination had the best results.

More recently, *Ming et al.* [60] fabricated a 3k NCCF fabric on a laminate with an automated fibre placement method. The fibre was coated by electroless deposition before being

deposited by a print head with a spacing of 3.59 mm to achieve the same areal density as the ECF (195 g/m²). This solution was able to limit damage to the surface of the laminate, when exposed to a current of 100 kA, behaving like the ECF protection.

Metal coated chopped carbon fibre paper

Zhao et al. [43] used chopped NCCF (15 to 20 mm long) to make several films and impregnated them with a varying quantity of bismaleimide resin (BMI), from 10 to 60 g/m². The 20 g/m² film showed the best compromise between tensile strength and through-thickness conductivity. However, when added to the top of the laminate, the laminate retained only 40% of its compressive strength after a DBC test, while the unprotected laminate retained 46%.

Metal coated nylon

Zhao et al. [61] combined three layers of 26 g/m² silver plated nylon web containing 42.3 wt% of silver, and a 55 g/m² graphene doped epoxy film. After a DBC test, damage to the first three layers of the laminate (0.52 mm) were observed, as well as a damage area of 7,562 mm². In comparison, the ECF-protected specimen was only damaged on one layer (0.25 mm). This solution retained a compressive strength after lightning strike (CALS) of 381 MPa, 50 MPa higher than pristine CFRP but 28 MPa lower than ECF.

Zhu et al. [51] fabricated a coating based on nylon filters on which nickel was deposited by electroless deposition. A 16.1 µm thick layer of nickel was deposited on both sides of the 100 µm thick nylon filter, forming a sandwich structure with a conductivity of 3.15 S/m. The film weighed 149.7 g/m² and contained 58.8 wt% nickel. The nylon film provided better protection against a 100 kA lightning strike than the ECF, while being slightly lighter. Indeed, the compressive strength was maintained at 95.82% compared to 92.62% for ECF. Due to its sandwich structure, this coating was also very effective for electromagnetic shielding. The low cost of this solution, below 20 \$/m², was also highlighted.

Metallic nanoparticles dispersed in CnT paper [47], [48] or CnF paper [62] were also considered as hybrid sacrificial layer. The first solution had a higher retention of compressive strength after a DBC test than the ECF and the second one retained 90% of its flexural strength after a 100 kA test.

2.3.1.2 Sacrificial and insulating layer

Some research groups have evaluated the effect of adding an insulating layer between the LSP and the CFRP, such as woven glass fibres [63] or insulating adhesive [50], [61].

The insulating layer acts as [63]:

- an electrical insulator by limiting the arc attachment to the laminate surface as well as perforation by dielectric discharge,
- as a thermal insulator by protecting the CFRP from very high arc temperatures and gases from the vaporised sacrificial layer by Joule effect,
- as a refractory material that can withstand very high temperatures (up to 1,000 °C for glass fibre, 900-1,500 °C for boron nitride [50] without catching fire).

However, as *Kumar et al.* [36] have noted, the high-intensity discharge emulators used in the laboratory generally operate at relatively low voltages (20 to 30 kV) which are not representative of the voltages found in nature (>100 kV). Thus, the use of dielectric layers for LSP is not recommended until high-current and high-voltage tests are carried out together to confirm their performance.

2.3.2 Inside the laminate

Modifications can also be made within the laminate to increase its resistance to lightning strikes. Several approaches were studied: the modification/replacement of the epoxy resin, the use of thin ply preregs, the addition of layers between the carbon fibre plies, of nanofillers or of conductive wires in the thickness direction. Each solution generally has one or both of the following objectives: increasing the through-thickness conductivity and increasing the interlaminar resistance.

2.3.2.1 Resin modification

a) PANI

In 2016, *Hirano et al.* [64] produced a PANI-based resin containing DBSA, DVB and p-toluenesulfonic acid (PTSA) (15/31/50/4 by mass percentage). DBSA acts as a dopant for PANI and as a curing agent for DVB, while PTSA is used to increase the electrical conductivity of the resin. A laminate containing this resin (CF/PANI) and a conventional one

(CF/epoxy) were produced. The flexural strength of the CF/PANI laminate was 267 MPa compared to 610 MPa for the CF/epoxy laminate, a 56.2% decrease. However, the flexural modulus was maintained at the same level, slightly above 50 GPa. Both laminates were exposed to 40 and 100 kA lightning strikes. The CF/PANI laminate retained 90% of its flexural strength in both cases, while the CF/epoxy laminate retained only 24% for the 40 kA lightning strike and was destroyed in the 100 kA test. These excellent results were explained by a $5.92\times$ increase in the in-plane electrical conductivity and a $27.4\times$ increase in the through-thickness conductivity compared to CF/epoxy. Thermal properties and mass varied very little between the two laminates.

In 2017, *Katunin et al.* [65], [66] produced a slightly different resin from the one described above. They synthesised PANI, mixed it with camphorsulfonic acid (CSA) (1:3 by mass) and added the mixture to epoxy. For a PANI/CSA mass percentage higher than 70 wt%, the resin produced was no longer compatible with the moulding process because it was too viscous, but below 50 wt% the PANI tended to agglomerate, and the resistivity was then high. A thermogravimetric analysis (TGA) measured the total decomposition temperature of the PANI/epoxy resin at 617.1 °C compared to 500 °C for pure epoxy. The ultimate tensile strength of a PANI/epoxy composite was still $3\times$ lower than CF/epoxy. The lightning tests performed in these papers are at low current (1-10 kA) or high voltage (62 kV), but the results were not much analysed.

In 2018, *Kumar et al.* [18] extended the work of *Hirano et al.* and *Katunin et al.* by making a PANI-DBSA/CSA/DVB resin (45/2.5/52.5 wt%). CF/PANI laminates were then fabricated, and their through-thickness electrical conductivity was decreased by heat treatment. Thus, four panels with through-thickness electrical conductivities of 110, 80, 58 and 34 S/m were produced. They were each exposed to a lightning current of 43 kA. Figure 2.15 shows the damage to the panels. The higher the through-thickness conductivity, the lesser the extent of the delamination and the fibre breakage. CF/PANI 110 and 80 had a limited damage area of, respectively, 490.9 mm² and 706.9 mm² while CF/PANI 58 and 34 were more severely affected with 11,309.3 mm² and 16,513.2 mm², respectively.

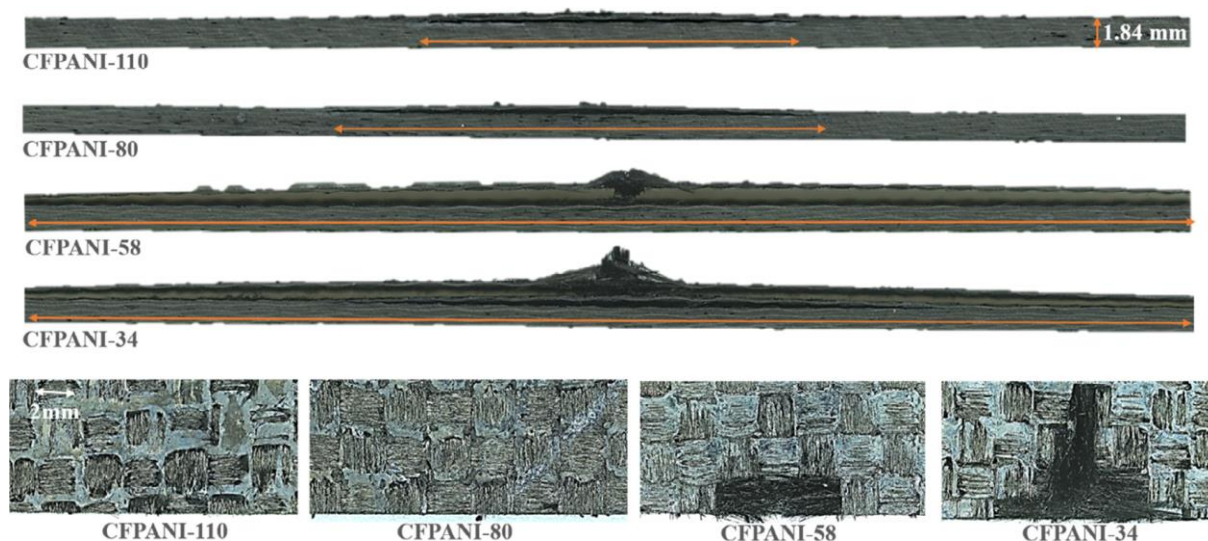


Figure 2.15: Cross-section and top views of the CF/PANI with various through-thickness conductivities after a 43 kA lightning strike test [18].

CF/PANI 110 retained its flexural strength at best with 92% while CF/PANI 34 retained only 73%. The reduction in flexural modulus is more significant and is estimated at 18% for CF/PANI 110. A comparison with a conventional or ECF-protected CFRP would have been appreciated to really evaluate the potential of the solution. With the same fibres and the same stacking sequence, the flexural strength of CF/epoxy before the lightning test was estimated at 610 MPa, which is only 37% and 22% higher than CF/PANI 110 and 34, respectively. This is an improvement over *Hirano et al.*'s laminate [64], which flexural strength was measured at 267 MPa.

In 2020, *Manomaisantiphap et al.* [67] manufactured hybrid laminates: the stack consisted of four plies of CF/PANI on top, an insulating adhesive and four plies of CF/epoxy. The PANI resin contained 43 wt% PANI/DBSA complex (1:2 ratio) mixed with DVB-CSA (55:2 ratio). Due to its structure, the laminate had very different properties when tested in flexure with the CF/PANI face in compression or in tension. In compression, the flexural strength was halved, whereas in tension it was only reduced by 8%. The laminate was struck by a current of 14 kA and a current of 40 kA. At 40 kA, the laminate retained only 70% of its flexural strength (with CF/PANI in compression).

Other groups replaced the epoxy resin with bismaleimide (BMI) [68], [43], a thermoplastic resin like PEEK [68] or PA6 [69] or a conductive epoxy with MWCnT [70].

Another group investigated the use of thin CF/PA6 plies as a replacement to the thicker traditional plies [69], [71]. The flexural strength retention after a 60 kA test was improved with the thin plies.

2.3.2.2 Interlayers

a) Hybrid

Zhao et al. [43] used films of chopped NCCF embedded in 20 g/m² BMI resin. These films were put between each ply of the CF/BMI laminate, including the top and bottom. After a DBC test, 0.28 mm deep damage, i.e. 2 layers, were reported, as well as a retention of 79.3% of the compressive strength. This performance is quite limited for an added mass of 340 g/m².

CnT papers were also considered as interlayers [72], [19], and a retention of 99% of the flexural strength after a 40 kA test was reported.

2.3.2.3 Nanofillers

Dong et al. [73] deposited 0.5 g/m² of nickel-plated MWCnT on carbon/epoxy fibre preregs. They placed 1, 2 or 3 plies containing these CnT on top of a 24-ply laminate. After testing at 30 kA, the addition of these conductive plies reduced the damage area, with 2,750 mm² for the unprotected CFRP, to 1,800 mm² for the laminate containing only one conductive ply and to 1,400 mm² for the laminate containing 3 conductive plies. The damage depth, however, remained constant at around 1.8 mm. These experimental results and a parallel simulation indicated the importance of the resin layer between the plies in the lightning strike resistance. If this layer was conductive (10 S/m against 0.1 S/m for a pristine CFRP), and found on at least the three first plies, the simulated damage would be almost non-existent.

Metallic [74] or hybrid [75] conductive wires connecting the plies were considered to improve the through-thickness conductivity and the interlaminar toughness and increase the LSP efficiency.

2.3.3 Commercialised lightning strike protection

Today, all commercialised LSP are metallic or hybrid sacrificial layers. Metallic meshes, with or without adhesive, are the materials sold by most companies, 8 according to *Kumar et al.* [36]. Metal coated CF in the form of nonwoven are the second choice with 4

companies [36], but only Veelo Tech. advertises its solution as LSP to this date. The other ones are primarily for EMI shielding application. Finally, LORD Corporation offers a conductive surfacing film that replaces the finishing layer by a conductive paint. This conductive film is made of silver particles and an epoxy resin and should pass Zone 1A tests with a 55% reduction in weight if compared to a traditional ECF solution. Unfortunately, no published data is available on this solution.

2.3.4 Conclusion and research objectives

All the solutions presented above are summarised at the end of this chapter in Table 2.2. In this table, all ECF and EAF that were tested with different waveforms are presented at first. Solutions presented after are compared to an equivalent test of ECF to estimate their potential. The results in green are similar or better than ECF. In red, the results are worst. Unfortunately, data on ECF response to 10, 32 or 60 kA currents or on mechanical properties retention of ECF for DBC and 40 kA tests are missing. Flexural property retention should be taken with a grain of salt because some authors used samples with the damaged zone in the middle and others cut the damaged zone in two, thus increasing the property retention.

Overall, several articles suggested solutions that could replace expanded copper foils: 14 sacrificial layers and only 1 laminate modification solution. Only one successful solution with paint was reported [17]. However, the areal density of this PANI-based adhesive, 357 g/m², is too high to be considered as a replacement for the ECF without further investigation.

Carbon nanomaterials, like reduced graphene oxide [46], or nickel coated nanotubes [50], [70], have proven their potential, just like silver nanoparticles dispersed in a CnT paper [48]. Yet, producing these LSP at an industrial scale was never questioned, the use of nanomaterials introducing higher cost and stricter health and safety norms.

Metal coated carbon fibres are a promising materials, considering the recent results from *Guo et al.* [56] and *Ming et al* [60]. Silver and nickel were the two metals considered. Their main properties are summarized in Table 2.1. On one hand, silver is more conductive and has a lower anodic index difference with graphite (anodic index of +0.25), resulting in a slower corrosion process if exposed. On the other hand, nickel is cheaper, lighter, and stable at higher temperature. Its latent heat of fusion and vaporization are also higher. Copper is displayed as reference. These properties can be an explanation for the lower LSP efficiency of silver electroless plating in comparison with copper electroless plating, as seen in Section 2.3.1.1.a,

or of silver coated nonwoven veils in comparison with nickel coated nonwoven veils, as seen in Section 2.3.1.1.c.

The project objectives are to develop a light, scalable and efficient lightning strike protection. This LSP should be efficient with paint. To facilitate the integration of the new LSP in the manufacturing process, only solutions on top of the laminate are considered. Nickel coated carbon fibre in a woven or nonwoven form could be this solution as they are:

- Light: the nonwoven plies tested in the literature have a dry weight of 70 g/m² but do not require as much resin as ECF. A woven NCCF ply could be used to replace the first layer of the CFRP, adding only the weight of the nickel to the laminate.
- Scalable: both are already commercially available in dry or prepreg rolls.
- Efficient: the results in the literature showed performance similar or better than the ECF on nonpainted panels.

The objective of this master thesis is to evaluate the lightning strike protection efficiency of nonwoven and woven nickel coated carbon fibres on nonpainted and painted carbon fibre reinforced polymers.

Table 2.1: Main properties of nickel, silver, and copper

Material	Electrical conductivity (<i>S/m</i>)	Density (<i>g/cm</i> ³)	Price (Jan. 22) (\$/ <i>kg</i>)	Anodic index (<i>V</i>) [76]	Molar heat capacity (<i>J/(mol.K)</i>)	Temperature (°C)		Latent heat (<i>kJ/mol</i>)	
						Fusion	Vaporisation	Fusion	Vaporisation
Nickel	1.44×10^7	8.91	24.3	−0.30	26.07	1,455	2,730	17.48	379
Silver	6.30×10^7	10.49	841.8	−0.15	25.35	962	2,162	11.28	254
Copper	5.96×10^7	8.96	9.76	−0.35	24.44	1,085	2,562	13.26	300.4

Table 2.2: Summary of the published LSP layers that were tested. In **green**, solutions that outperformed the ECF for the same LS test. In **red** the ones that did not. * = other test were conducted on similar materials or with lower current in the same article, but the best one is showed here. 3/4PB = 3/4 point bending test. Comp. = Compressive test

			Year	Author	Solution	Paint	Added mass (g/m ²)	LS Test	Damage area (mm ²)	Damage depth (mm)	Mechanical strength retention (%)	Type of test
On top of the laminate	Sacrificial metallic layer	Mesh	2011	Kawakami and Feraboli [29]	ECF	N	/	D	99	0	100	4PB
			2011	Kawakami and Feraboli [29]	ECF	Y	/	D	179	0	100	4PB
			2015	Han et al. [50]	ECF	N	460	D	/	/	/	/
			2018	Rajesh et al. [39]	ECF	N	370	40 kA	200	0	/	/
			2019	Guo et al. [35], [56], [63]	ECF	N	73.3 (dry)	D	/	<0.2	91.79	3PB
			2019	Guo et al. [35]	ECF	N	141.6 (dry)	D	/	<0.2	/	/
			2019	Guo et al. [35], [63]	EAF	N	78.1 (dry)	D	/	<0.2	94.45	3PB
			2019	Lombetti et al. [74]	ECF	N	100 (dry)	DBC	2,760	/	/	/
			2020	Zhao et al. [61]	ECF	N	275	DBC	/	0.25	/	/
			2020	Xia et al. [48]	ECF	N	73 (dry)	D	24,000	2	83.28	Comp.
			2021	Zhu et al. [51]	ECF	N	168.8	D	194.52	0.32	92.62	Comp.
			2021	Dydek et al. [49]	ECF	N	141 (dry)	DBC	1,440	0.6	/	/
		Nanoparticles	2018	Rajesh et al. [39]	Ag nparticles dispersed in PDOT:PSS	N	25.5	40 kA	2,100	0.95	/	/
		Continuous layer - electroless deposition	2018	Rajesh et al. [39]	Silver electroless deposition	N	52.5	40 kA	1,800	0.75	/	/
			2021	de Juan et al. [40]	Copper electroless deposition for 30min*	N	10.28	40 kA	2,434	/	/	/
		Continuous layer - spray	2018	Zhao et al. [43]	Aluminium spray	N	250	DBC	844	0.41	/	Comp.
			2018	Che et al. [44]	Cold tin spray	N	1,733.75	C	0	0	/	/
			2018	Rajesh et al. [39]	Cold copper-tin (10 wt% Cu) spray	N	2,850	40 kA	1,300	0	/	/
			2018	Wang et al. [41], [42]	Aluminium spray*	N	/	D	28,750	/	/	/
			2017	Zhang et al. [45]	Graphene film	N	200	DBC	877	0.35	/	/
	Sacrificial non-metallic layer	Graphene	2018	Wang et al. [46]	Reduced Graphene Oxide + epoxy film	N	30.6	40 kA	211	0.3	76.8	3PB
			2015	Han et al. [50]	MWCnT paper + epoxy/MWCnT adhesive*	N	745	40 kA	4,650	0.8	79.32	Comp.
		CnT	2019	Kumar et al. [19]	MWCnT paper	N	/	40 kA	314.16	/	79.90	F
			2019	Chu et al. [47]	SWCnT paper	N	40	DBC	1,500	0.8	75.6	3PB
			2020	Xia et al. [48]	SWCnT paper	N	40	D	14,145	2.41	80.35	Comp.
			2021	Dydek et al. [49]	SWCnT 'Tuball' paper*	N	41.5	DBC	2,475	0.85	/	/
			2021	Zhu et al. [51]	CnT paper	N	30	D	2,889.07	0.82	81.05	Comp.
		Conductive adhesive	2019	Kumar et al. [17]	PANI-based adhesive	Y	357	D	/	/	99	3PB
		Glass fibres	2018	Li et al. [52]	2 GF plies	N	1,352	32 kA	2,800	1.37	/	/

			Year	Author	Solution	Paint	Added mass (g/m ²)	LS Test	Damage area (mm ²)	Damage depth (mm)	Mechanical strength retention (%)	Type of test
On top of the laminate	Sacrificial hybrid layer	Metallic nanoparticles in CnT paper	2019	<i>Chu et al.</i> [47]	SWCnT paper	N	40	DBC	2,750	0.3	92.1	3PB
			2020	<i>Xia et al.</i> [48]	SWCnT paper	N	53.3	D	25,265	1.8	91.05	Comp.
		Metallic nanoparticles in CnF paper	2010	<i>Gou et al.</i> [62]	CnF paper with Nickel nanostrands*	N	/	D	1,496.77	1	90	3/4PB
			2011	<i>Chakravarthi et al.</i> [53]	Ni-SWCnT - Electroless plating	Y		DBC	517	/	/	/
		Spray of metal coated carbon nanomaterial	2018	<i>Rajesh et al.</i> [39]	Ag coated CnF in epoxy film	N	21.6	40 kA	2,750	1.3	/	/
			2006	<i>Haynes et al.</i> [55]	Nonwoven NCCF	N	100	D	/	/	/	/
		Metal coated nonwoven CF paper	2019	<i>Guo et al.</i> [56]	Nonwoven NCCF *	N	70	D*	/	0.2	98.33	3PB
			2019	<i>Zhang et al.</i> [57]	Nonwoven SCCF	N	150	D	1,660	0.2	/	/
			1993	<i>Henn et al.</i> [58]	NCCF woven fabric	N	190 (added Ni on CF ply)	A	/	/	/	/
		Metal coated CF woven ply	2009	<i>Mall et al.</i> [59]	12k NCCF woven fabric	N	/	D	/	/	50	Comp.
			2009	<i>Mall et al.</i> [59]	12k NCCF woven fabric + Randomly oriented SWCnT paper	N	/	D	/	/	70	Comp.
			2021	<i>Ming et al.</i> [60]	3k NCCF woven fabric via Automated Fibre placement	N	195	D	/	/	/	/
		Chopped metal coated CF paper	2018	<i>Zhao et al.</i> [43]	Chopped NCCF/BMI film	N	20	DBC	11,078	1.17	40.05	Comp.
		Metal coated nylon	2020	<i>Zhao et al.</i> [61]	3 layers of silver-plated nylon web + graphene doped epoxy film	N	133	DBC	7,562	0.52	/	/
			2021	<i>Zhu et al.</i> [51]	Nylon filters with nickel layer on both sides	N	149.7	D	1,652.82	0.55	95.82	Comp.
	Insulating layer + Sacrificial layer	GF ply	2019	<i>Guo et al.</i> [63]	ECF + GF ply	N	175 (dry)	D	/	/	95.5	3PB
			2019	<i>Guo et al.</i> [63]	EAF + GF ply	N	180 (dry)	D	/	/	97.15	3PB
		Insulating adhesive	2015	<i>Han et al.</i> [50]	MWCnT paper + epoxy adhesive*	N	745	D	4,460	0	97.62	Comp.
			2015	<i>Han et al.</i> [50]	MWCnT paper + epoxy/Boron nitride adhesive*	N	325	D	860	0	98.23	Comp.
			2020	<i>Zhao et al.</i> [61]	3 layers of silver-plated nylon web + graphene doped epoxy film + expanded graphite epoxy film	N	168	DBC	/	0.24	/	/

			Year	Authors	Solution	Paint	Added mass (g/m ²)	LS Test	Damage area (mm ²)	Damage depth (mm)	Mechanical strength retention (%)	Type of test
Inside the laminate	Resin modification	PANI	2016	Hirano et al. [64]	PANI-based resin : PANI/DBSA/DVB/PTSA (15/31/50/4 in wt%)	N	/	D*	741	/	90	4PB
			2017	Katunin et al. [66], [77]	PANI-based resin : PANI/CSA/Epoxy (2:10:5 in wt%)	N	40 (vs. CF twill)	10 kA*	/	/	/	/
			2018	Kumar et al. [18]	PANI-based resin : PANI-DBSA/CSA/DVB (45/2.5/52.5 in wt%)*	N	/	40 kA	490.9	/	92	3PB
			2020	Manomisantiphap et al. [67]	Hybrid laminate : half CF/PANI (PANI/DBSA/CSA/DVB, 14/29/2/55 in wt%) , half CF/epoxy	N	/	40 kA*	153.94	/	70	4PB
		BMI	2018	Kamiyama et al. [68]	CF/BMI	N	/	D*	9,500	/	/	/
		Thermoplastic	2017	Yamashita et al. [69], [71]	CF/PA6 using thick plies	N	/	60 kA*	2,890	0.528	65	4PB
			2018	Kamiyama et al. [68]	CF/PEEK	N	/	D*	10,390	/	/	/
		Conductive epoxy	2012	Logakis et al. [70]	CF/Epoxy filled with MWCnT + ECF*	N	/	DBC	/	/	/	/
	Thin-ply prepregs	2017	Yamashita et al. [69], [71]	CF/PA6 QI using thin plies	N	/	60 kA*	1,500	0.396	80	4PB	
		2017	Yamashita et al. [69], [71]	CF/PA6 ROS using thin plies	N	/	60 kA*	3,260	/	82	4PB	
		Interlayers	Non-metallic	2019	Zhang et al. [57]	SCCF nonwoven on top + SWCnT film in the first 13 interlayers	N	84	DBC	1,095	0.8	/
	2019			Kumar et al. [19]	MWCnT paper on top + first 3 interlayers	N	/	40 kA	/	/	99.67	F
	Hybrid		2018	Zhao et al. [43]	Chopped NCCF/BMI film on top + first interlayer	N	40	DBC	18,446	1.16	46.24	Comp.
			2018	Zhao et al. [43]	Chopped NCCF/BMI film on top + bottom + all interlayer	N	340	DBC	6,243	0.28	79.34	Comp.
	Nanofillers		2017	Dong et al. [73]	Ni-MWCnT deposited on the first 3 plies	N	1.5	30 kA	1,400	1.8	/	/
	Conductive wires	Metallic	2019	Lombetti et al. [74]	Copper wires between the 10 central plies of a 24-ply CFRP*	N	/	DBC	2,190	/	/	/
		Hybrid	2017	Rehbein et al. [75]	Silver coated nylon wires in CFRP*	N	175	DBC	6,500	/	/	/

CHAPTER 3 METHODOLOGY - EXPERIMENTAL PLAN

In this chapter, we present the methodology used to choose, characterise, and test the woven and nonwoven nickel coated carbon fibre (NCCF) as a lightning strike protection (LSP) for composite panels. Firstly, we introduce the materials and how we integrate them on composite panels. Secondly, we present the characterisation made before the lightning strike (LS) test on dry materials and undamaged panels. Thirdly, we explain the LS emulation setup. Finally, we describe the characterisation of the damage on the panels after the LS test.

3.1 Materials

We decided to test both nonwoven and woven NCCF technologies to protect the required materials: composite panels manufactured by Bell Textron. The quasi-isotropic laminates were manufactured by autoclave consolidation and contained 8 plies (layers) of HTS40 3k (3,000 filaments/fibre) plain weave (PW) fabric from Teijin that were preimpregnated with the 5276-1 epoxy from Solvay. Each ply weighed $\sim 195 \text{ g/m}^2$ and the stacking sequence was $[0^\circ/45^\circ/0^\circ/45^\circ]_s$. Nonwoven NCCF would be integrated on top of the first ply as a sacrificial conductive layer. Woven NCCF would replace the first CF/epoxy ply as structural and LSP layer.

3.1.1 Selection

We searched and selected the manufacturer of NCCF for this project between September 2020 and January 2021. NCCF were commercialised in different forms and by various companies:

- Spools: Teijin Carbon, Conductive Composites,
- Woven (W): Teijin Carbon (TC), Conductive Composites,
- Nonwoven (NW): Conductive Composites (CC), Technical Fibre Products, VeeloTech.

We contacted all these companies, but were only able to discuss with TC and CC.

TC offered 12k NCCF tows with 40 wt% of nickel and the weaving of the NCCF fabrics. However, we expected a 100% 12k NCCF PW fabric to be too heavy. TC offered to

manufacture hybrid PW fabric with 3k CF (8 tows/inch) and 12k NCCF (1.25 tow/inch). A fibre areal density of 300 g/m² was expected.

CC had developed a chemical vapor deposition (CVD) coating line to coat any kind of CF woven, nonwoven or tows with a chosen quantity of nickel. This technology allowed a nickel deposition on every filament, even within the fibre tows. They offered off-the-shelf nonwoven NCCF, with areal densities ranging from 11 to 70 g/m² and sheet resistivities from 0.5 to 0.02 Ω /sq, as well as 3k NCCF twill 2×2 fabrics with 22 wt% and 32 wt% of nickel, i.e., 250 and 287 g/m².

We chose to investigate the CC materials because their mass ranges were within our mass budget (targeted added mass ~100 g/m²) and their industrial process seemed scalable. Furthermore, they offered both nonwoven and woven materials, making it easier for the following discussions.

Unfortunately, VeeloTech did not answer our requests. Their nonwoven solutions were promising with higher specific conductivities than CC materials, unlike Technical Fibre Products nonwoven. All these data are summarised in Table 3.1. CC were the only company offering off-the-shelf woven NCCF materials.

We ordered four nonwoven NW0.5, NW0.3, NW0.1, NW0.04 and one woven W0.1 dry rolls from CC and integrated them as described after. They were named after the measured sheet resistivity of the dry rolls.

Table 3.1: Areal density and sheet resistivity ranges from commercialised nonwoven NCCF

Company	Areal density range (g/m ²)	Sheet resistivity range (Ω /sq)
Conductive Composites [78]	11-70	0.5-0.02
Technical Fibre Products [79]	4-80	3.6-0.8
VeeloTech [80]	20-80	0.04-0.002

3.1.2 Integration

Bell Textron had never manufactured laminates with these materials before, so a first round of integration test was carried out. As the materials were dry, we doubted their ability to stick to the lower CF/epoxy ply. Hence, Bell Textron considered adding one or two epoxy-based adhesive 299-947-104 Ty K Gr 5 layers. As shown in Figure 3.1, the W (a) was integrated

with an adhesive layer between the baseline and the W and one on top, or with just the first one. Two kinds of NW (b, c) were integrated with an adhesive layer between the baseline and the NW, or without. The laminates were cured with the LSP layer as described earlier. In total, twelve panels were manufactured (two per configuration).

The twelve panels were tested with our lighting strike emulator (see Section 4.1). After these preliminary tests, we decided to integrate the NW and W without adhesive, as shown in Figure 3.2. The dry W were added by manual wet lay-up on a 7-ply laminate already cured and without adhesive (c). They are named NC. The dry NW were added on top of the 8-ply prepreg stack without adhesive and cured with the laminate (d). They are named NS. Four NW veils with various sheet resistivities (0.5, 0.3, 0.1 and 0.04 Ω/sq) were integrated. The excess resin of the prepregs was expected to impregnate the NW veil. Reference panels were also manufactured: the baseline composite panels named CF (a) and the baseline protected by ECF named ECF (b). All solutions, except the NC were painted, with an epoxy-based paint, and a “P” is added before the acronym if the panel was painted.

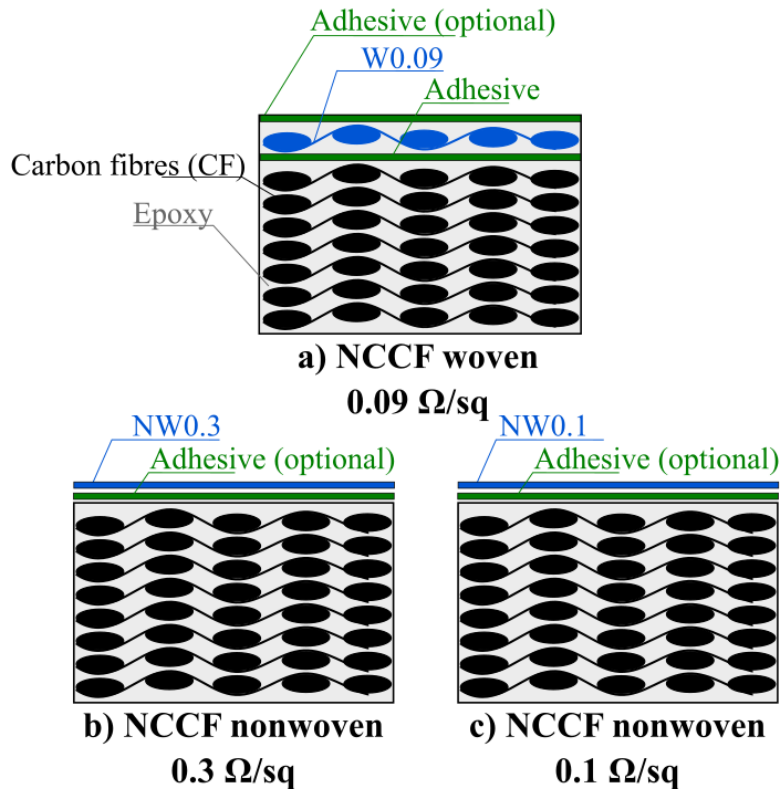


Figure 3.1: Integration test panels configuration. a) Woven NCCF integrated with one or two adhesive layers. b) Nonwoven NCCF 0.3 Ω/sq integrated with zero or one adhesive layer, like the NCCF NW 0.1 Ω/sq (c).

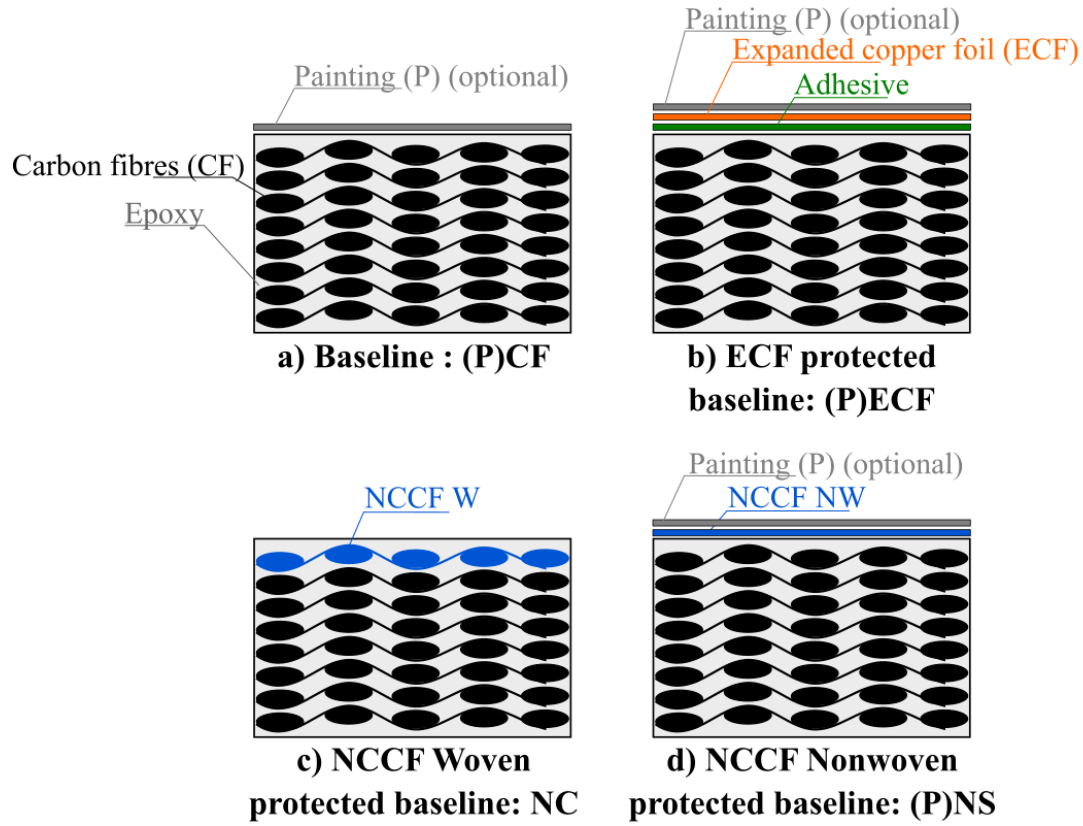


Figure 3.2: Test panels configuration for each LSP solution. a) Baseline panels with (PCF) or without (CF) a paint layer. b) Baseline panels protected by an expanded copper foil with (PECF) or without (ECF) a paint layer. c) Baseline panels protected by a woven NCCF fabric replacing the first carbon fibre ply without a paint layer (NC). d) Laminates protected by a nonwoven NCCF with (PNS) or without a paint layer (NS).

A distinction is made between NW/W and NS/NC. NW/W refer to the dry materials before integration and NS/NC refer to the protected panels, i.e., after integration of the NCCF-based materials.

For each solution, a $\sim 150 \times 180$ cm plate was manufactured and cut in 30.5×30.5 cm panels. The woven NCCF wet lay-up was made after the cutting. The panels were inspected by ultrasonic testing to detect defaults (more details in Section 3.4.2). Bell Textron manufactured at least seven nonpainted panels and seven panels covered for each solution.

3.2 Pre lightning strike test characterisation

3.2.1 Mass and thickness

Once received, and before any alteration, all materials were weighed with a Explorer Pro 6101 scale. Their thickness was measured with a Mitutoyo N°99MAA001M3 micrometer. The paint thickness was also measured with an optical microscope.

3.2.2 Scanning electron microscopy (SEM)

The nonwoven and woven NCCF were observed with a SM 7600 TFE scanning electron microscope coupled with an energy-dispersive X-ray (EDX). The samples were first encapsulated in epoxy then in non-conductive bakelite and sanded. The NW0.5 was coated with a 10 μm thick layer of carbon, but the carbon deposition damaged the epoxy cast. So, the other samples were coated with a 5 μm thick layer of chrome.

The SEM images were used to evaluate the thickness and the invasiveness of the nickel coating on the carbon fibres.

3.2.3 Simultaneous thermal analysis (STA)

We performed a thermal analysis on CF samples using a SDT Q600 V20.9 Build 20 simultaneous thermal analyser from TA Instruments that performed simultaneously a thermogravimetric analysis (TGA) and a differential scanning calorimetry (DSC). Each sample was heated at a constant heating rate (5, 10, 25 $^{\circ}\text{C}/\text{min}$) in an inert atmosphere. The TGA recorded the evolution of the sample mass and the DSC the evolution of the heat flow compared to a reference sample. The analysis of these two curves gave us information on the behaviour of the CF laminate at high temperature.

3.2.4 Emissivity

The emissivity ε of a material represents its ability to radiate energy. It is the ratio of the thermal radiation of the material surface to the radiation of an ideal black body at the same temperature with the same surface, hence $0 < \varepsilon < 1$. We measured the emissivity of the reference panels using a SOC-100 HDR reflectometer from Surface Optics Corporation. The sample was heated at different temperatures ranging from 30 $^{\circ}\text{C}$ to 100 $^{\circ}\text{C}$ and the emissivity

measured for infrared wavelengths ranging from 3.5 μm to 35 μm . The obtained values were used for the thermal camera observations during the LS tests (see Section 3.3.3).

3.2.5 Conductivity measurements

3.2.5.1 4-point probe method (4PPM)

The electrical conductivity is a common indicator for the LSP efficiency. For materials with a thin coating, the sheet resistivity ρ_s (in Ω or Ω/sq) is used for characterisation and measured using 4-point probe method.

As shown in Figure 3.3.a), four aligned electrodes, spaced by a distance s , are pressed against the material. The current is injected between the #1 and 4 electrodes, and the voltage is measured between the #2 and 3 electrodes. We calculate the sheet resistivity using:

$$\rho_s = C \frac{V_M}{I}, \quad (3.1)$$

where ρ_s is the sheet resistivity, I the injected current and V_M the measured voltage and C a correction factor depending on the sample geometry. For an infinite plane, $C = \frac{\pi}{\ln(2)} \approx 4.5324$ [81].

The 4PPM yields more accurate results than the traditional 2-point probe method (2PPM) [82], where the current is injected, and the voltage measured at the same points, as shown in Figure 3.3.b). Indeed, an electrical contact resistance exists between an electrode and the sample, but these contact resistances are not considered in the same way in those two methods.

In the case of the 2PPM, the voltage is measured at the terminals of the sample resistance and the two contact resistances R_{contact} through which the injected current is flowing. Hence:

$$V_M = V_s + 2 \times R_{\text{contact}} \times I.$$

In the case of 4PPM, the voltage measured V_M is the sum of the sample voltage V_s and the voltage in both contact resistances R_{contact} through which a small current $I_{\text{voltmeter}}$ flow. Hence:

$$V_M = V_s + 2 \times R_{\text{contact}} \times I_{\text{voltmeter}} \approx V_s.$$

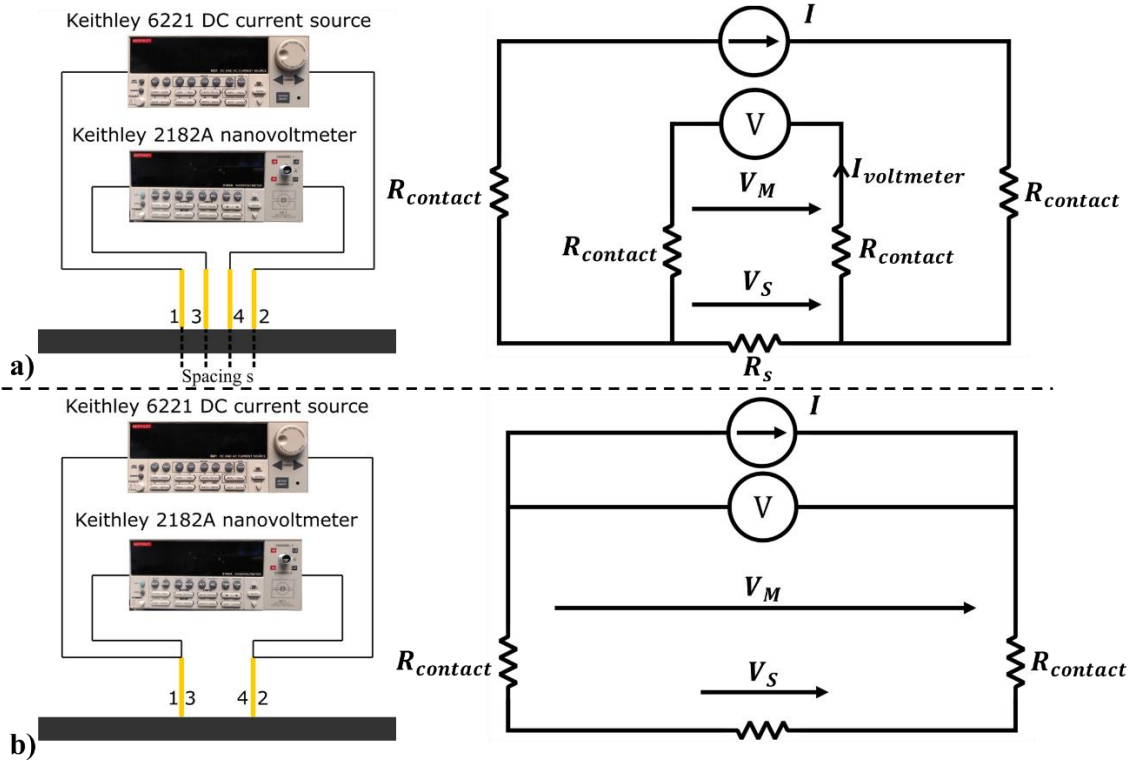


Figure 3.3: 4-point probe (a) and 2-point probe (b) methods with equivalent electrical diagram. For both methods, a current I is injected in the sample between electrodes #1 and 2 and the voltage measured between electrode #3 and 4. V_M is the measured voltage, V_S is the voltage across the sample, $R_{contact}$ are the contact resistances, through which a small current $I_{voltmeter}$ flow in a 4PPM.

Thus, the voltage measured with 4PPM is closer to the real voltage across the sample than with 2PPM.

3.2.5.2 4PPM setup

As shown in Figure 3.4, we fabricated the 4PPM setup with a 5 mm spacing using a breadboard, 4 spring loaded pins and a 3D-printed block with fused filament fabrication of polylactic acid. The pressure was applied using a C-clamp. We used Keithley 6221 current source to inject the current and Keithley 2182A nanovoltmeter to measure the voltage.

For each solution, three 7.5×7.5 cm samples were cut from undamaged sections of test panels, as shown in yellow in Figure 3.6.b and sanded with P120 sandpaper to remove the thin resin layer on top of the laminate.

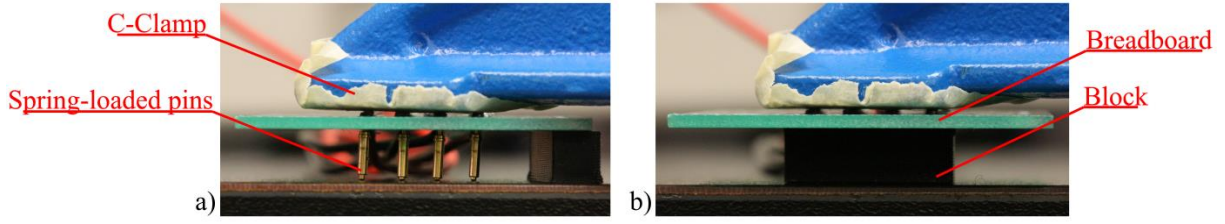


Figure 3.4: 4-point probe method setup. a) Without the block to show the spring loaded pins.
b) Real test conditions with the block and the C-clamp applying pressure.

We measured their sheet resistivity with the described setup. Dry nonwoven and woven samples of the same size were also measured. A correction factor $C = 4.3882$ was applied [81]. We measured the sheet resistivity on four different locations on each sample. A current sweep from 40 to 60 mA with 11 steps was injected in the sample, and the voltage measured 3 times at each step. Thus, for each solution, the value of the sheet resistivity was the average of 132 measurements.

3.3 Lightning strike test

3.3.1 Lightning strike emulator

The lightning strike test were performed with an emulator developed at Polytechnique Montreal and described in [83]. The LS emulator and an equivalent electrical circuit are shown in Figure 3.5. The capacitors C are charged at ~ 60 kV with the spark gap G open. The spark gap is then slowly closed. When the two graphite spheres are close enough, the circuit is closed, and the capacitor can discharge in the sample $\{L_s, R_s\}$. Without the diodes, the circuit is a RLC ($R_{damp} + R_s / L_G + L_s / C$) with a time to half peak of $12.3 \mu s$, while $\sim 70 \mu s$ was the target. Indeed, R_{damp} is high enough to make the current peak independent from the sample resistance R_s , but this also result in a too short time to half peak. To lengthen this time, a column of diodes is added in parallel of the sample. Thus, after the discharge of the capacitors in the sample, the RLC circuit becomes a RL (R_s / L_s) circuit with a longer decay time. However, the decay time becomes more dependent of the sample since R_{damp} is bypassed. The resulting current waveform is a modified waveform A [7] with a lower peak current of ~ 40 kA.

The current is injected via a 12.7 mm wide copper electrode located at 5 mm above the centre of the 30.5×30.5 cm (1×1 ft) sample. The sample is grounded by an aluminium frame on its 4 edges. The surface of the sample in contact with the frame is sanded before the test to minimise the contact resistance. Six panels per solution are typically struck.

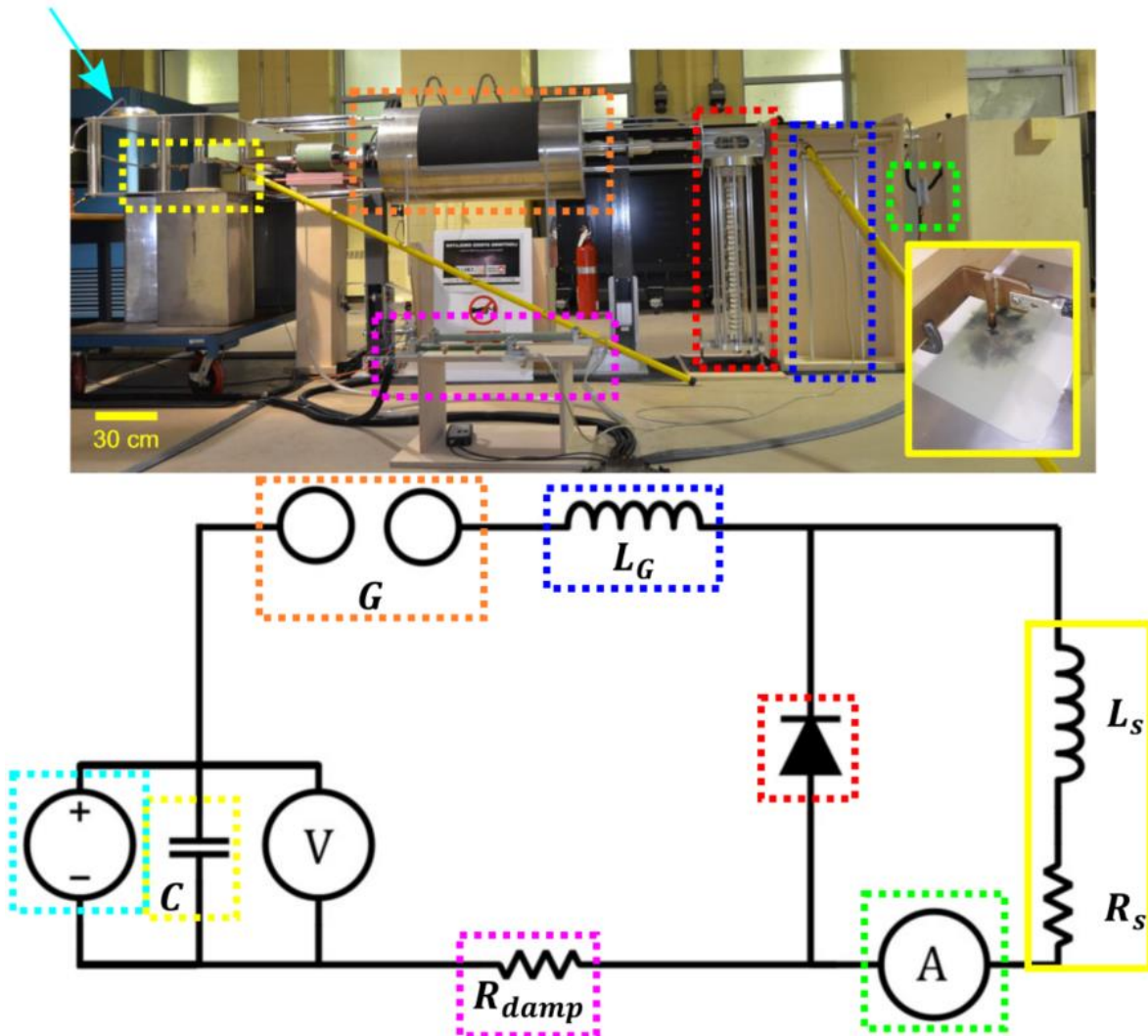


Figure 3.5: Lightning strike emulator and equivalent electrical circuit. Cyan dotted lines/arrow: Voltage source. Yellow dotted lines: capacitors. Orange: spark gap. Blue: adjustable inductance. Red: diode column. Purple: damping resistance. Green: Rogowski current waveform transducer. Yellow full line: sample and copper electrode. The voltage probe is not on the photo.

3.3.2 Voltage and current measurements

During each test, the voltage and current were recorded using a Lecroy Wavesurfer 422 oscilloscope. As shown in Figure 3.5, the voltage was measured at the capacitor terminals. The current intensity was measured after the sample using a Rogowski current waveform transducer CWT 600B from Power Electronic Measurements Ltd. This probe uses a coil closed upon itself around the wire. The change of current induces a voltage in the coil and an integrator integrates the induced voltage to reproduce the current waveform.

3.3.3 High-speed thermal camera

We used a Telops MS M350 high speed thermal camera to record the sample surface temperature for 4.5 s after the LS, at 350 images per second. As the temperature decreased quickly back to the room temperature, we selected a filter with the lowest lower bound: [10 °C, 338 °C]. The recording was triggered by the light flash. We used a 12 cm wide fan to evacuate the smoke above the panel as quickly as possible.

3.4 Post lightning strike test

3.4.1 Visual observation

After the LS, we described the damage modes of the sample and took photos of the panels. We were able to measure a rough estimate of the damaged area. For each solution, a sample was cut in the middle of the damage with a DeWalt D24000S wet circular saw, as shown in Figure 3.6.a. The cross-section view gave us information on the delamination, the size of the damage and its depth.

3.4.2 Ultrasonic testing (C-Scan)

Before the cross-section observation, all the struck panels were sent to Bell Textron for an ultrasonic testing (C-Scan), a non-destructive technique, on a Tecscan gantry system. The reflection, or pulse-echo, method is used. A transducer sends ultrasonic waves in the panel and the defects or interfaces reflect the waves. The reflected waves are received by the transducer and a 14 dB attenuation criteria is used to identify the damage area. The damage

can either be on the surface or within the laminate. The data were processed by Anamaria Serbescu.

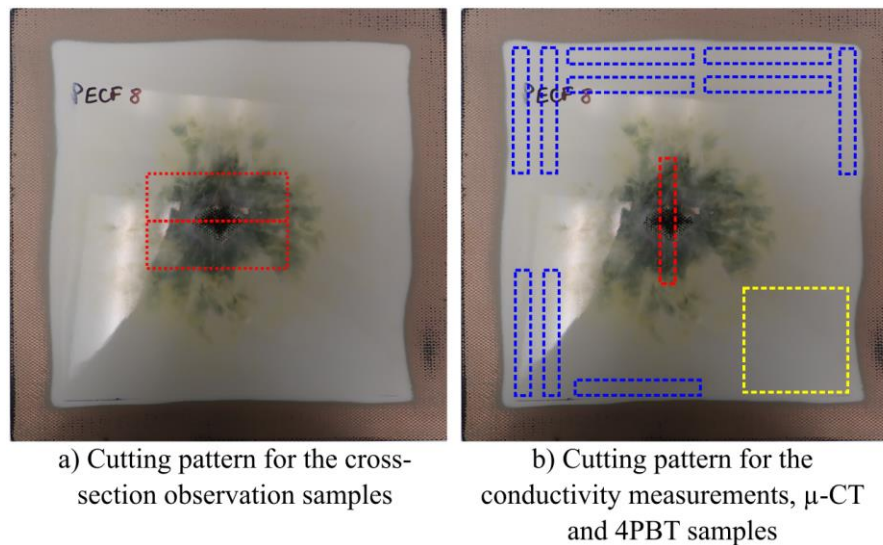


Figure 3.6: Cutting patterns on damaged samples. a) One sample per solution, cut with a circular saw for cross-section observation. b) Five samples per solution, cut with a water jet for the electrical conductivity measurements (yellow), μ -CT (red) and 4PBT (blue and red).

3.4.3 X-ray microtomography (μ -CT)

X-ray microtomography (μ -CT) observations were carried out using a Zeiss X Radia versa 520. A 12.7×90.0 mm sample was cut with a FLOW Mach 3 1313b water jet machine from the centre of one damaged panel per solution, with the damage centred, as shown in red in Figure 3.6. This sample was also used for the 4-point bending test. The μ -CT observation recreated a 3D-model of the damaged sample. These observations were made by Jean Langot.

3.4.4 4-point bending test (4PBT)

The retention of the ultimate flexural strength and the effective bending stiffness were evaluated with 4-point bending tests using the Instron 1362 MTS and according to the standard test method ASTM D6272 [84]. Five 12.7×90.0 mm samples were cut in both 0° and 90° directions with water jet from one undamaged panel per solution as reference. Then, using the sample observed with the μ -CT and four other samples cut the same way, the mechanical properties after the lightning strike were evaluated with the damaged side in tension, as shown in Figure 3.7.a). The thickness, or depth, of the sample D ranged from 1.69 to 1.95 mm, depending on the material. According to the standard test method, we used a

support span S to depth ratio of 32 and a support to load span L ratio of 3 so $L = 32 \times D$ and $S = 32 \times D/3$. Since $D < 3.2$ mm, the width of the sample was set to $W = 12.7$ mm. The flexural strength is inversely proportional to D^2 and the effective bending stiffness to D^3 . We used loading and support noses with a 5 mm diameter, even though the standard method indicated that 10 mm diameter noses were needed. Indeed, it was the largest noses available in the mechanical testing lab.

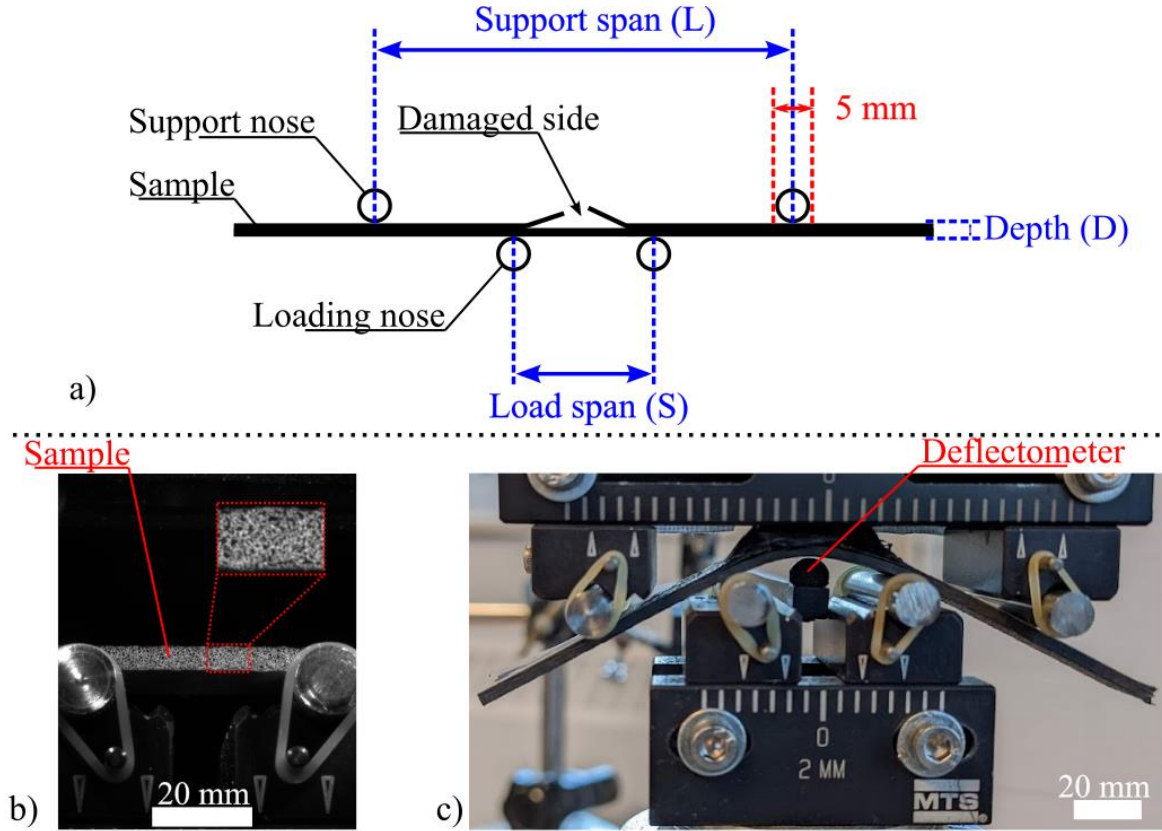


Figure 3.7: 4-point bending test method and set-up. a) Loading diagram. b) Image of a sample before the bending test with the painted pattern on its side surface for the DIC. c) Instron 1362 MTS fixture with the deflectometer installed.

We first used digital image correlation (DIC) to measure the deflection of the reference panels (CF, PCF, ECF, PECF). As shown in Figure 3.7.b, a pattern was painted on the sample side surface and the bending test was video recorded. We computed the displacement of the sample using the painted pattern.

A displacement gauge MTS opt 632.06H-30 was then used to measure the deflection of the other samples, as shown in Figure 3.7.c. These tests were conducted by Kambiz Chizari and Jean Langot and Jean Langot processed the data.

We calculated the ultimate flexural strength σ_u and the effective bending stiffness E_B using the load P at first maximum deflection at the centre of the specimen Def_{max} and m the slope of the tangent to the initial straight-line, as shown in Figure 3.8.

$$\sigma_u = \frac{P \times L}{W \times D^2} \left(1 + 4.70 \frac{Def_{max}^2}{L^2} - 7.04 \frac{Def_{max} \times D}{L^2} \right) \quad (3.2)$$

$$E_B = 0.21 \frac{L^3 \times m}{W \times D^3} \quad (3.3)$$

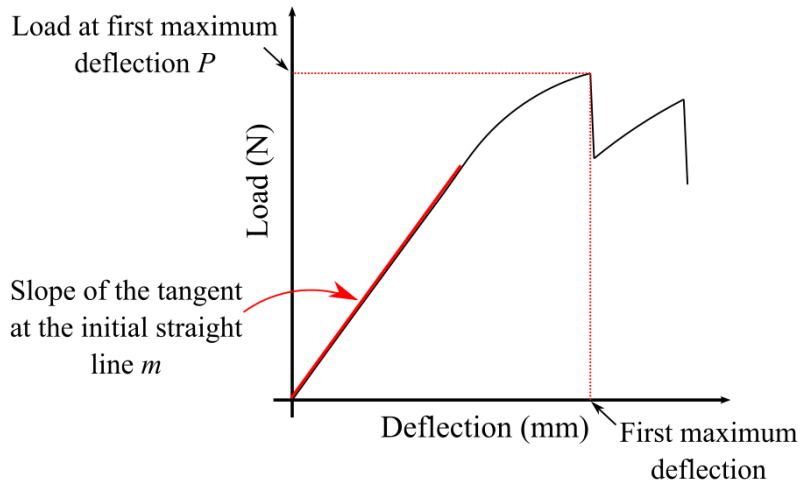


Figure 3.8: Deflection-load curve of a typical 4-point bending test. P is the load at first maximum deflection. m is the slope of the tangent at the initial straight-line.

As shown in blue in Figure 3.6.b), ten undamaged samples from the panels struck by lightning were also cut, tested and their mechanical properties compared to the undamaged panel to assess the variation of these properties among one solution.

The experimental plan presented above is summarised in Figure 3.9. For each solution, at least seven panels were used for the characterisation of the material before, during and after the LS test. Panel #1 was not struck by emulated lightning and acted as reference for the mechanical and electrical properties. CF1 was used for STA measurement. The emissivity of CF1, PCF1, ECF1 and PECF1 was measured. All the other six panels of each solution were struck by emulated lightning. We recorded the panel surface temperature with a thermal camera, as well as the current in the panel. All panels were then inspected by C-Scan and cut according to Figure 3.6. Panels #2 and 3 were used for conductivity measurements, panel #6 for μ -CT observation and panel #7 for cross-section observation. All panels except #7 were tested with 4PBT.

We developed this broad experimental plan to better understand the LSP efficiency of each solution. The results are presented in the next chapter.

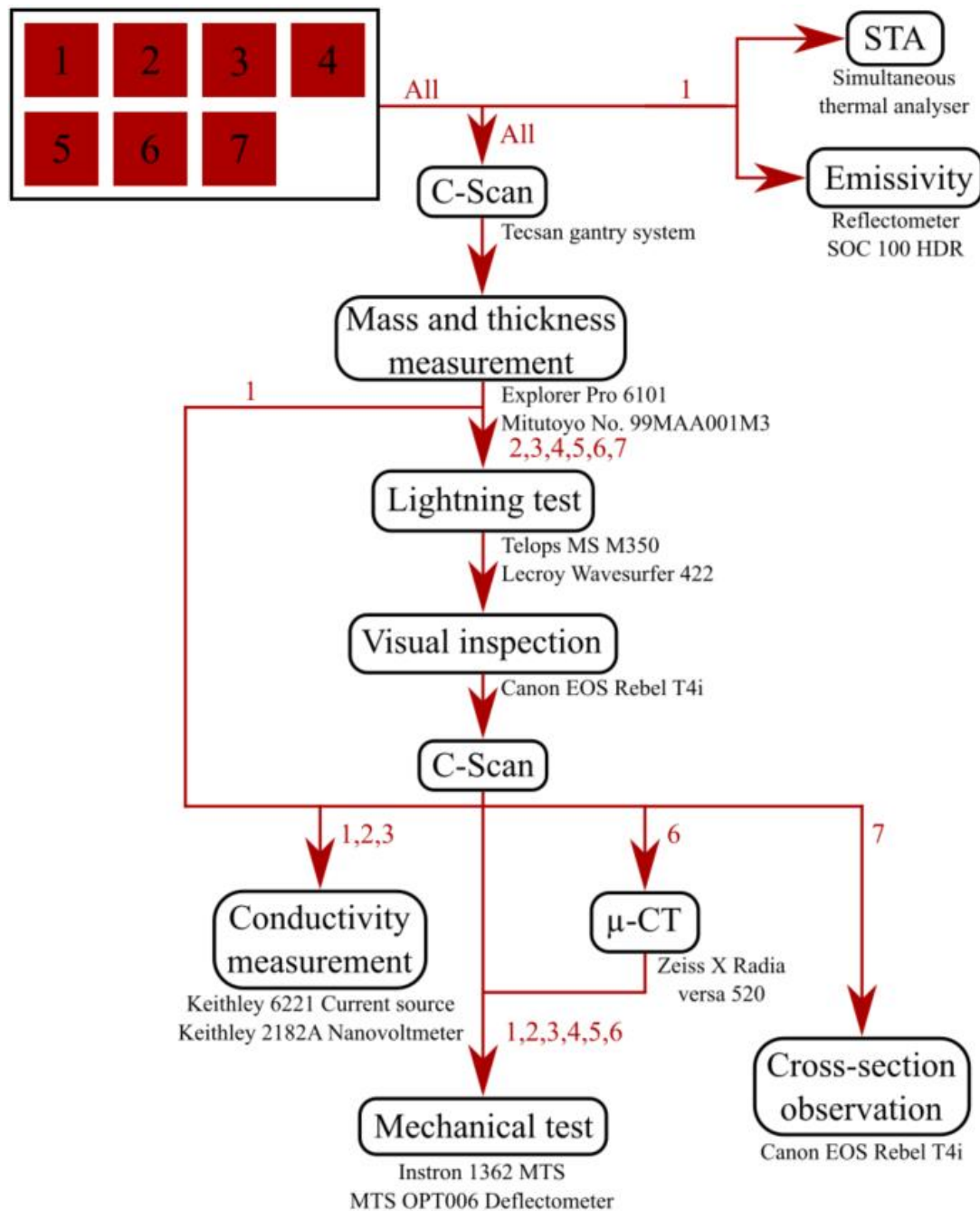


Figure 3.9: Experimental plan for each LSP solution. All panels: C-Scan post-production and mass/thickness measurement. Panel #1: undamaged, mechanical, and electrical properties. STA: only for CF1 and PCF1. Emissivity: only for CF1, PCF1, ECF1, PECF1. Panel #2-7: Struck by emulated lightning, C-Scan, conductivity measurement (#2-3), μ-CT (#6) and cross-section (#7) observation and 4PBT (#2-6).

CHAPTER 4 RESULTS

In this Chapter, we present the results of the experimental plan described previously, our understanding of the observed damage mechanisms and a discussion on the lightning strike protection efficiency of the different solutions.

An uncertainty is given when the measurements were made on different panels or samples. The uncertainties in the tables or in the figures represent 1 standard deviation.

4.1 Integration

4.1.1 Integration test

The 12 integration test panels were tested to assess of the best manufacturing process required for the NW and W samples, but also to test our experimental plan. The visual aspect of the panels after the emulated lightning strike (LS) test are shown in Figure 4.1. The copper tape and the sanded spots were used to measure the sheet resistivity of the samples, but this method proved to be time-consuming and was changed for the one presented in Section 3.2.5.

The NC with 1 adhesive layer (a) showed carbon fibre breakage on a 15×18 mm zone. The adhesive also evaporated on several locations around the damaged zone. The carbon fibre breakage zone for the NC with 2 adhesive layers (b) extended over a 20×24 mm area with fewer evaporation spots around the damage. No fibre breakage was observed on the NS0.04 without adhesive (c), but the nonwoven was damaged on several locations and the resin evaporated around the attachment point. The addition of an adhesive layer worsened the results for the NS0.04 (d). Fibre breakage was observed on a 19×23 mm area. The NS0.1 samples (not shown here) with and without adhesive showed similar damage than the NS0.04.

It seems that the insulating adhesive layer behaved like painting and caused severe damage. All the laminates with at least one layer of adhesive were damaged on the first carbon fibre plies, hence we chose not to use adhesive for the integration of the W and NW on the carbon fibre reinforced polymers.

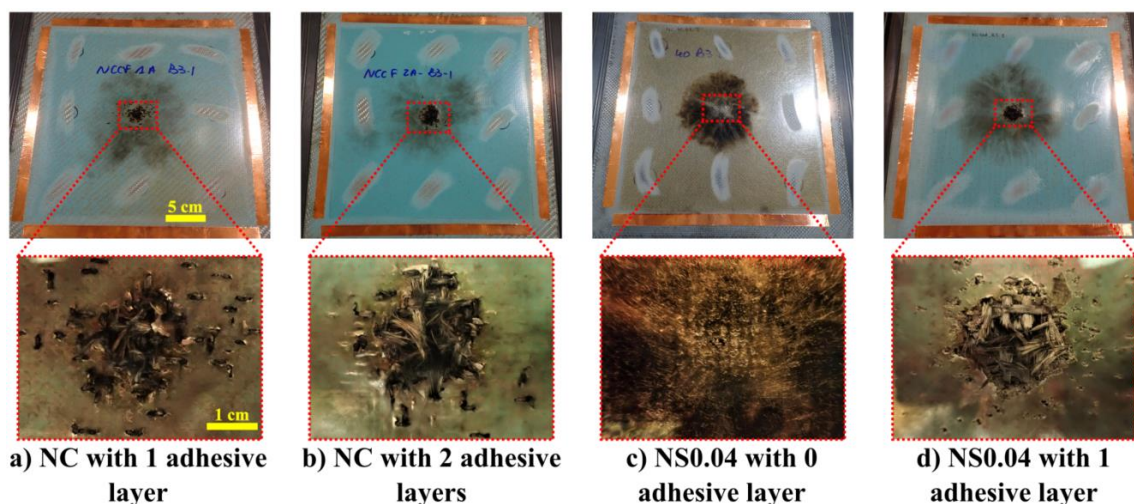


Figure 4.1: Full and zoomed views of the integration test panels after LS test

4.1.2 Final integration

The dry woven cloth (W0.09) was added by wet hand lay-up on a 7-ply laminate already cured. The W ply was glued to the laminate with resin, but the top of the panel was not covered with resin such that we could touch the nickel-coated carbon fibre (NCCF).

The dry nonwoven veils (NW0.5, NW0.3, NW0.1 and NW0.04) were added on top of the 8-ply prepreg stacks without adhesive and cured with the laminates. However, the more conductive the nonwoven was, the less flexible and permeable it was. The resin did not fully impregnate some regions of the NS0.3 and NS0.1 plates, as shown in Figure 4.2. The regions circled in red highlight the dry NCCF areas. On NS0.3, the spots were small (< 1 mm diameter) and we considered that they would not affect the representativity of the LS test. However, for NS0.1, the fibres were left dry on larger areas. So, after cutting, ~ 11 g/m² of resin was added on top of the majority of the NS0.1 panels reserved for painting to cover the regions with low resin impregnation. Considering that these regions were mainly located in the middle of the plate, NS0.04 panels were manufactured in smaller plates ($\sim 61 \times 61$ cm) to prevent poor resin impregnation, successfully. There was an issue with the integration process of the PNS0.04 panels as most panels were not enough compacted, as shown in Figure 4.3. This created regions with resin agglomeration and other with porosities. Overall, the impacted panel regions were thicker than the rest. A new batch of NS0.04 and PNS0.04 will be manufactured to confirm the obtained results.

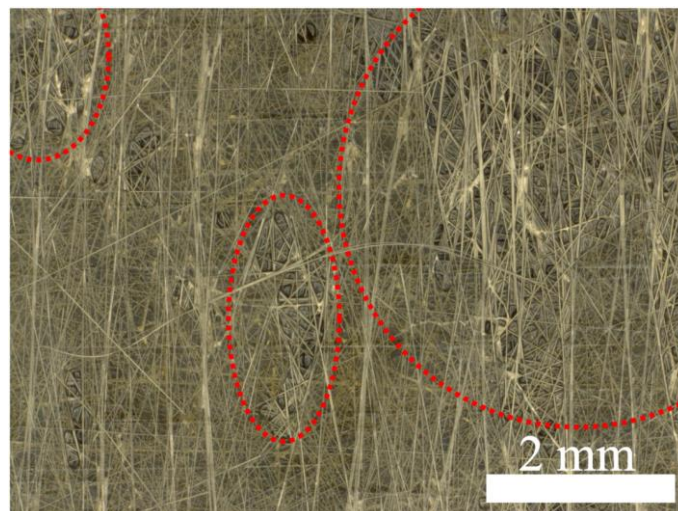


Figure 4.2: Top view of the surface of NS0.1 after curing. Circles in red: regions with a lack of resin impregnation in the nonwoven.

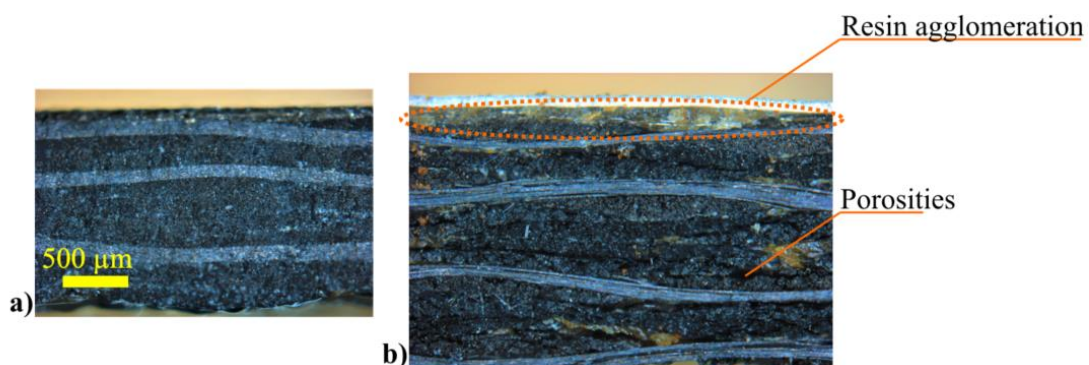


Figure 4.3: Same scale cross-section views of a) NS0.04 and b) PNS0.04. The PNS0.04 is thicker than the NS0.04 and has porosities and resin agglomeration regions. A poor compaction during the integration process is probably responsible.

4.2 Pre lightning strike test characterisation

4.2.1 Dry mass and thickness

Before integration, we measured the dry weight of the NCCF materials. As shown in Figure 4.4, the more conductive the NW was, the higher its areal density. NW0.5 and NW0.3 had similar areal density, respectively 18 and 19 g/m², NW0.1 weighed 43 g/m² and NW0.04 70 g/m² and no extra resin was used for their integration, except for PNS0.1. The woven NCCF weighed 295 g/m² and ~50 g/m² of resin were used for the wet lay-up process. As it replaced a 195 g/m² fabric, a ~150 g/m² added mass was expected. In comparison, the copper

areal density in the expanded copper foil was 142 g/m^2 , but a $220 \pm 24 \text{ g/m}^2$ adhesive was used to glue the copper mesh to the laminate.

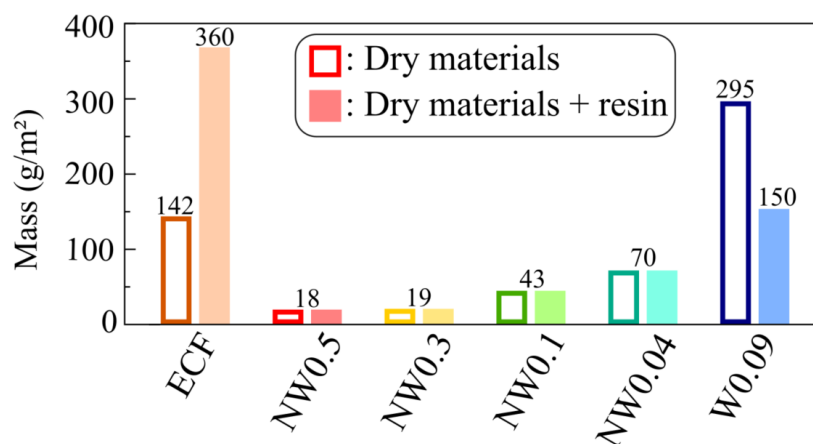


Figure 4.4: Measured dry mass of the LSP solutions and total mass of the LSP considering the dry material and the adhesive/resin. The NW were integrated with no extra resin. The ECF was integrated with a $220 \pm 24 \text{ g/m}^2$ adhesive. The W was integrated with $\sim 50 \text{ g/m}^2$ of resin.

As shown in Table 4.1, CF and all NS, except NS0.04, had a similar thickness close to 1.690 mm. NS0.04 had a lower thickness with 1.606 mm. ECF and NC were, respectively, 1.834 and 1.865 mm thick.

Concerning the painted panels, PCF was as thick as PNS0.04 with 1.731 mm. However, it was thinner than all the other PNS that were between 1.783 and 1.803 mm. PECF had an average thickness of 1.953 mm. We observed the paint layer with an optical microscope, as listed in the last column of Table 4.1. The paint thickness ranged from 0.068 mm for PCF to 0.102 mm for PNS0.01. The value for PNS0.04 was not yet available when this thesis was written.

The lower thicknesses of NS0.04, PCF and PNS0.04 were within the requirements of Bell Textron for their carbon fibre prepreps.

Table 4.1: Average thickness of the panels measured with a micrometer and paint thickness measured with the microscope observations

Solution	Panel thickness (mm)	Paint thickness (mm)
CF	1.694 ± 0.010	-
ECF	1.834 ± 0.016	-
NS0.5	1.695 ± 0.004	-
NS0.3	1.695 ± 0.012	-
NS0.1	1.689 ± 0.009	-
NS0.04	1.606 ± 0.012	-
NC0.09	1.865 ± 0.005	-
PCF	1.731 ± 0.179	0.068 ± 0.010
PECF	1.953 ± 0.030	0.072 ± 0.010
PNS0.5	1.788 ± 0.010	0.097 ± 0.013
PNS0.3	1.783 ± 0.023	0.074 ± 0.010
NS0.1	1.803 ± 0.024	0.102 ± 0.011
NS0.04	1.731 ± 0.036	N/A

4.2.2 Scanning electron microscopy (SEM)

We observed the dry woven and nonwoven NCCF with a SEM. As shown in Figure 4.5 and Figure 4.6, the chemical vapor deposition process from Conductive Composites deposited a uniform nickel coating on all carbon fibre filaments, even within the fibre bundle of the W. These filaments were near perfect cylinders with a $3.5 \mu\text{m}$ radius. The NW filaments had a non-conventional shape, like a cylinder pressed on one side, with an original radius of $3.5 \mu\text{m}$. To obtain this value, we measured the area of the filament, and assuming it was a cylinder, we calculated its original radius.

A $0.24 \mu\text{m}$ thick nickel layer was observed on the filament within the woven bundles. Hence, 37.4 wt% of the 295 g/m^2 W was nickel. For the nonwoven veils, the observed nickel layer thickness was 0.66, 1.32, 1.42 and $3.14 \mu\text{m}$ for NW0.5, NW0.3, NW0.1 and NW0.04, respectively.

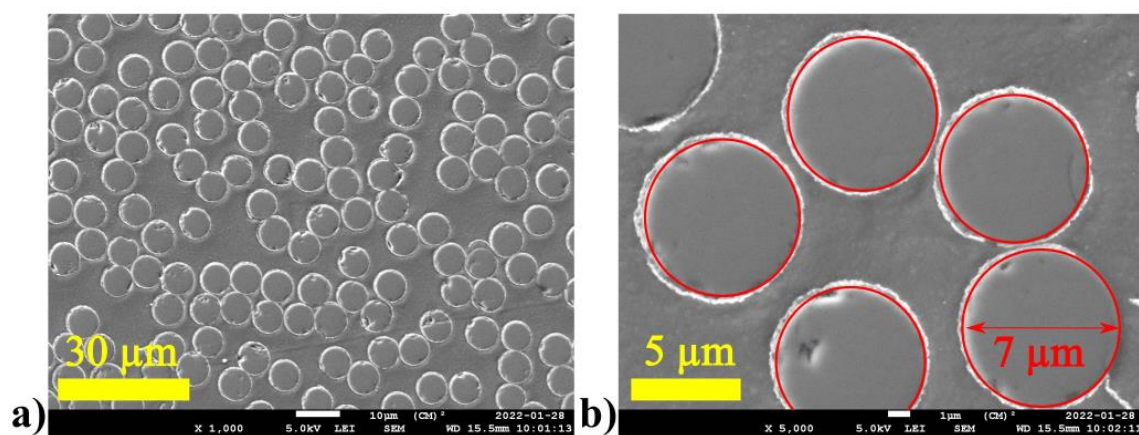


Figure 4.5: Scanning electron microscope observations of the nickel coating thickness on the woven NCCF. a) Uniform deposition of nickel among a fibre bundle. b) Close view of a NCCF filament. Filament mean diameter: 7 µm. Nickel coating thickness: 0.24 ± 0.05 µm.

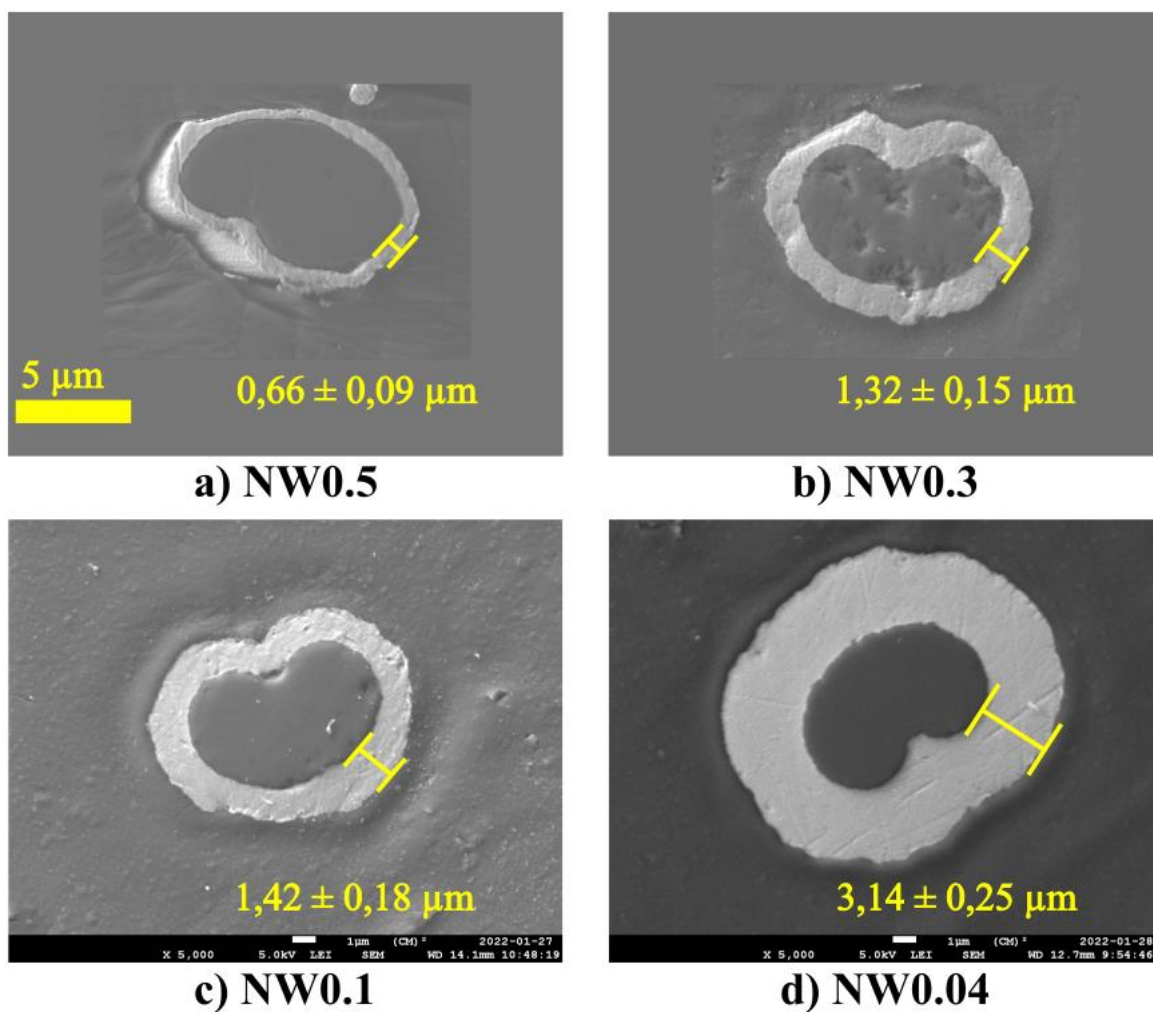


Figure 4.6: Scanning electron microscope observations of the nickel coating thickness on a filament of a nonwoven NCCF. a) NW0.5. b) NW0.3. c) NW0.1. d) NW0.04.

The NW0.3 nickel coating thickness was twice that of NW0.5, but their dry weights were similar with, respectively, 19 and 18 g/m². The NW0.1 nickel coating thickness was only 0.10 μ m thicker than NW0.3 in average, but its dry weight was twice that of NW0.3 with 43 g/m². With these observations, we were not able to explain the non-correlation between the dry weight and the nickel coating thickness. The number of coated filaments per unit area was the only parameter left to explain these gaps, but it was not measured.

Using the SEM images of the woven and nonwoven NCCF, we computed the energy needed for the dry LSP layer to go from 20 °C to vaporization. This energy gave us a information on the ability of the LSP layer to withstand the high energy impulse of the lightning strike. Hence, we used the latent heats of fusion and vaporization of nickel and copper, listed in table Table 2.1, the latent heat of sublimation of graphite [85], the temperatures of the phase transition as well as the heat capacity of each element. The energy stored for each element is listed in Table 4.2. Nickel stores 33% more energy than copper. However, both metals stored energy are negligible in comparison with graphite that stores at least 10 \times more.

We computed the amount of stored energy in each LSP layer, as shown in

Table 4.3. ECF stores 837.4 kJ/m², which is more than NW0.5 and NW0.3. NW0.3 is the NCCF-based LSP that stores the smallest amount of energy with 480.9 kJ/m². Indeed, its areal density is close to that from NW0.5, but it contains more nickel than NW0.5. The order is respected for all the other nonwoven: the lower the sheet resistivity is, the higher is the amount of stored energy. NC0.09 stores more than 17 \times the amount of energy of NW0.04 because it is 4 \times heavier and contains more graphite in mass percentage than any other NCCF-based LSP.

We will use the stored energy values in the last Section of this chapter, when discussing the LSP efficiency and the damage mechanisms of each solution.

We also used these observations to compute an equivalent electrical conductivity of each carbon fibre filament coated with nickel. The results are found in the Appendix D.

The results of the simultaneous thermal analysis and the emissivity measurements are presented in the Appendices B and C, as they were only used to interpret the thermal camera images.

Table 4.2: Stored energy between 20 °C and vaporisation per mass for copper, nickel and graphite

Element	Stored energy (kJ/g)
Cu	5,9136
Ni	7,9588
CF	90,3079

Table 4.3: Stored energy per area in each LSP layer

LSP	Areal density (g/m ²)	Element	Element mass percentage (%)	Element areal density (g/m ²)	Stored energy (kJ/m ²)
ECF	141.6	Cu	100	141.6	837.4
NC0.09	295	Ni	37	110.2	17565.0
		C	63	184.8	
NW0.5	17.9	Ni	62	11.1	705.4
		C	38	6.8	
NW0.3	19.1	Ni	79	15.1	480.9
		C	21	4.0	
NW0.1	42.5	Ni	883	35.3	932.2
		CF	17	7.2	
NW0.04	70.2	Ni	92	64.6	1017.6
		CF	8	5.6	

4.2.3 Conductivity measurements

We measured the sheet resistivity of the dry NCCF materials and of the integrated panels with a 4-point probe method. The results are shown in Figure 4.7. The sheet resistivity of the NCCF woven fabric was measured at 0.092 Ω/sq . The nonwoven veils had a sheet resistivity ranging from 0.430 Ω/sq (NW0.5) to 0.036 Ω/sq (NW0.04). The order was consistent with the nickel coating thickness observed with the SEM and the dry weight of the materials.

Once integrated, the sheet resistivity of NC was in the same range as the dry material at 0.106 Ω/sq . However, a decrease of the sheet resistivity from the dry materials was observed on all the integrated NS samples. For example, once integrated NS0.5 had a sheet resistivity of 0.175 Ω/sq while the dry NW0.5 had a sheet resistivity of 0.430 Ω/sq .

The reference panels had a sheet resistivity of $0.007 \Omega/\text{sq}$ for the ECF and $0.250 \Omega/\text{sq}$ for the CF. These results showcased the high electrical conductivity of a non-metallised carbon fibre woven fabric as well as the existing gap in the electrical conductivity between NCCF-based materials and pure copper mesh like the ECF, $5\times$ less resistive than NS0.04.

The difference in behaviour, when integrated, between the NS and NC could be explained by the different integration methods. The nonwoven veils were added on top of the carbon fibre prepregs and compacted. As shown in Figure 4.8, we observed contacts between the NCCF filaments and the first carbon fibre ply, allowing the laminate to participate in the electrical conduction when the current is injected on the LSP layer. The woven was added by wet lay-up on an already cured laminate and we did not observe a clear contact between the woven and the cured laminate. Hence, only the NCCF woven fabric participated in the electrical conduction.

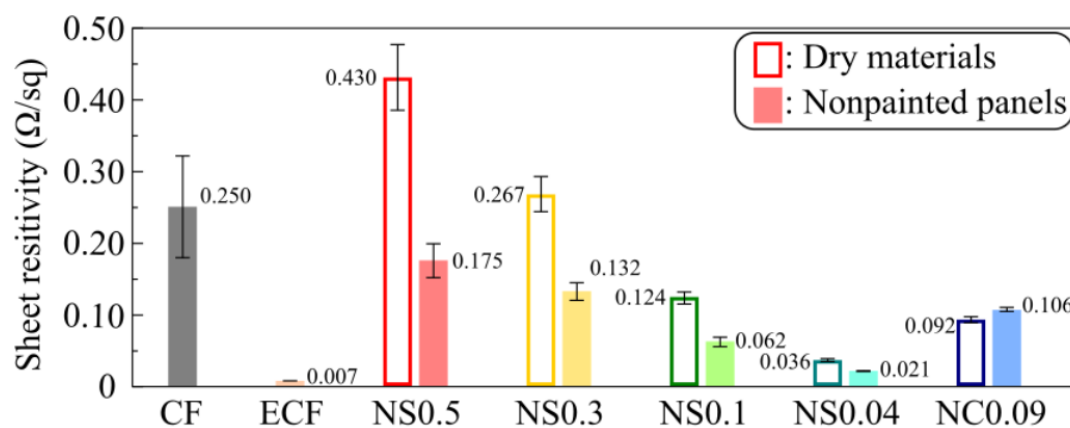


Figure 4.7: Sheet resistivity of the dry and integrated materials obtained with 4PPM method



Figure 4.8: NS0.1 cross-section observation with optical microscope ($\times 90$). Circled in red: NCCF in contact with the first carbon fibre ply.

Considering the sheet resistivity of the baseline CF and the sheet resistivity of the dry NW, we calculated the equivalent sheet resistivity of the integrated NS samples. We considered the dry NW and the CF in parallel with no contact resistance in between. Hence:

$$\frac{1}{\rho_{s,eq}} = \frac{1}{\rho_{s,NW}} + \frac{1}{\rho_{s,CF}}, \quad (4.1)$$

where $\rho_{s,eq}$ is the equivalent sheet resistivity, $\rho_{s,NW}$ is the dry NW sheet resistivity and $\rho_{s,CF} = 0.250 \pm 0.072 \Omega/\text{sq}$ is the sheet resistivity of CF. As shown in Figure 4.9, the equivalent sheet resistivity and the measured sheet resistivity of the NS samples are close. It confirms the contact observed between the nonwoven and the baseline laminate. The calculated value for NC0.09 is lower than the measured one. This confirms the absence of contact between the woven NCCF ply and the baseline laminate.

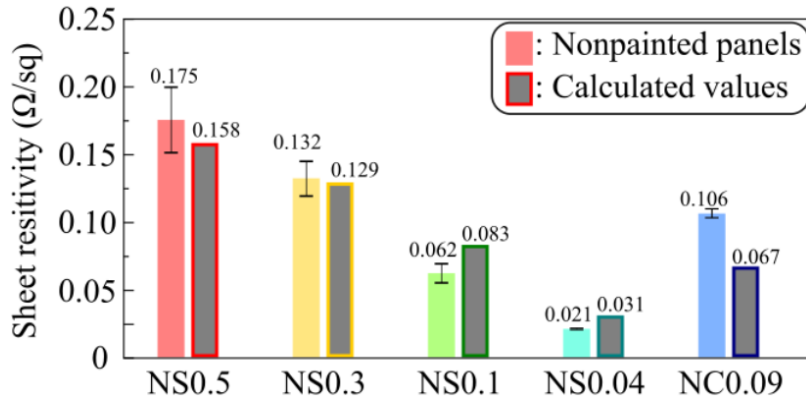


Figure 4.9: Measured sheet resistivity of the nonpainted panels and equivalent sheet resistivity of the panels considering the dry NCCF materials and the CF laminate in parallel with

$$\rho_{s,CF} = 0.250 \pm 0.072 \Omega/\text{sq}.$$

4.3 Lightning strike test

4.3.1 Voltage and current measurements

6 panels per solution were tested with the LS emulator located in Polytechnique Montreal. A typical current waveform injected in a composite panel is shown in Figure 4.10, and the waveform parameters for each solution are displayed in Table 4.4. The current quickly rose to its peak in $t_2 \approx 6.0 \mu\text{s}$, with only small variations among the different solutions. The peak current was measured between 35.1 and 37.0 kA in average. The decrease of the current was evaluated with the time to half peak t_2 , i.e., the time it takes for the current to reach half of its

peak value. This time depended on the value of the sample resistance R_s , as explained in Section 3.3.1. Hence, the more conductive the sample appeared to the LS emulator (i.e., the lower R_s was), the longer was t_2 . As shown in Table 4.4, t_2 was the highest for the ECF with 64.8 μs . CF and NC0.1 had a similar time to half peak with 35.5 and 35.8 μs respectively. The expected order for the NS samples was found: t_2 ranged from 39.8 μs (NS0.5) to 54.2 μs (NS0.04). For all the painted panels, t_2 had a decrease in the 9.5-13.2 μs range from the nonpainted panels, except for PNS0.1 and PNS0.04, with a $>19.8 \mu\text{s}$ decrease. Hence, PNS0.1 appeared less conductive to the LS emulator than the PNS0.3. This exception was attributed to the resin added after curing to these panels because of the poor resin impregnation, as explained earlier in Section 4.1.2.

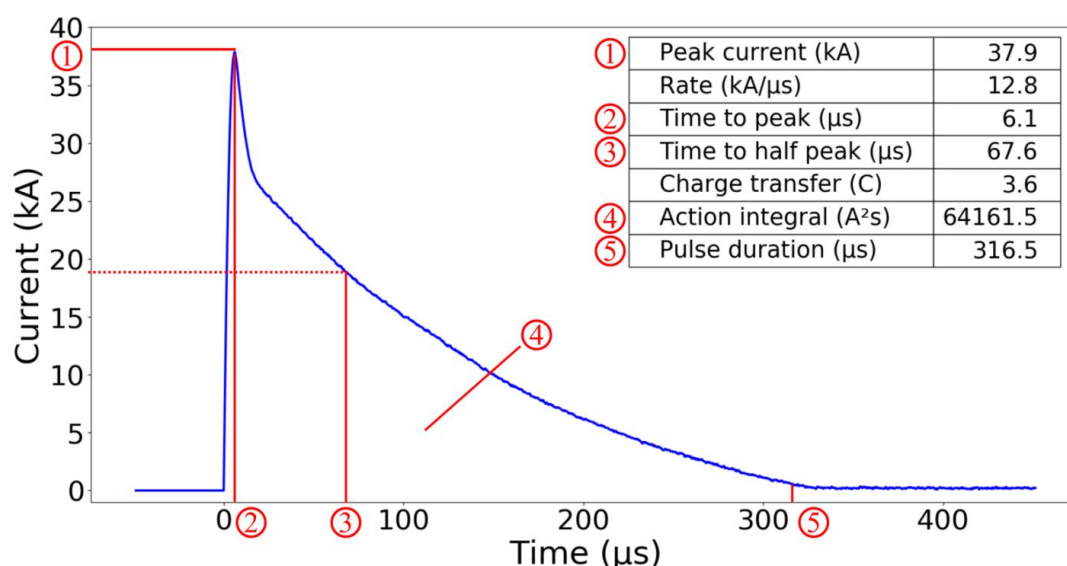


Figure 4.10: Typical test waveform produced by the lightning strike emulator developed at Polytechnique Montreal.

The action integral of the current waveform (see Section 2.1.2.3) was proportional to t_2 in the $24.2 - 59.4 \times 10^3 \text{ A}^2\text{s}$ range. For comparison, a waveform D has an action integral of $250 \times 10^3 \text{ A}^2\text{s}$. Hence, our panels were subjected to an emulated lightning strike 5 to 10 \times less energetic than the closest standard waveform. However, our results were still interpretable as we could compare the LSP efficiency of the NCCF materials with the reference panels ECF and CF.

Table 4.4: Waveform parameters of the tested panels

Solution	Peak current (kA)	Time to half peak (μs)	Action integral ($10^3 \text{ A}^2\text{s}$)
CF	35.1 ± 0.2	35.5 ± 0.8	30.4 ± 1.1
ECF	37.0 ± 1.3	64.8 ± 3.1	59.4 ± 6.3
NS0.5	36.4 ± 0.4	39.8 ± 0.8	35.5 ± 1.8
NS0.3	36.7 ± 0.1	40.8 ± 0.8	36.8 ± 0.9
NS0.1	36.7 ± 0.1	48.4 ± 0.7	42.9 ± 0.4
NS0.04	36.8 ± 0.3	54.2 ± 0.8	48.2 ± 1.3
NC0.09	36.7 ± 0.3	35.8 ± 1.1	31.8 ± 1.3
PCF	35.7 ± 0.8	25.0 ± 0.4	22.6 ± 1.1
PECF	36.2 ± 0.8	55.3 ± 0.7	50.2 ± 2.4
PNS0.5	36.3 ± 0.5	26.6 ± 1.1	24.2 ± 1.3
PNS0.3	36.7 ± 0.3	30.2 ± 0.7	27.4 ± 0.6
PNS0.1	36.7 ± 0.5	28.6 ± 0.7	26.5 ± 1.0
PNS0.04	36.7 ± 0.4	31.6 ± 0.6	29.1 ± 0.8

4.3.2 High-speed thermal camera

During each LS test, we recorded the temperature profile of the panel surface with a high-speed thermal camera using a $[10^\circ\text{C}, 338^\circ\text{C}]$ filter for 4.58 s after the LS. We used the emissivity measurements (see Appendix C), to correct the measured temperature.

The surface temperature of three different panels at different times after the LS are shown in Figure 4.11. We observed on all panels a high temperature area located around the attachment point that decreased with time. The other “hot spots” on the image in the first instants (0.08 and 0.30 s) are smoke or hot particles in the air. The green pixels on the image were saturated, i.e., they measured a temperature above 338°C . On the bottom of each images, the copper electrode used to inject the lightning current on the composite surface is visible. For most nonpainted panels, like CF (a) and NS0.5 (b), the smoke and flames dissipated quickly, and we were able to measure the temperature of the surface after 10 or 20 ms. For the painted panels, like PNS0.5 (c), the images were readable only after 0.8-1 s. Before that, smoke or flames were recorded around the attachment point.

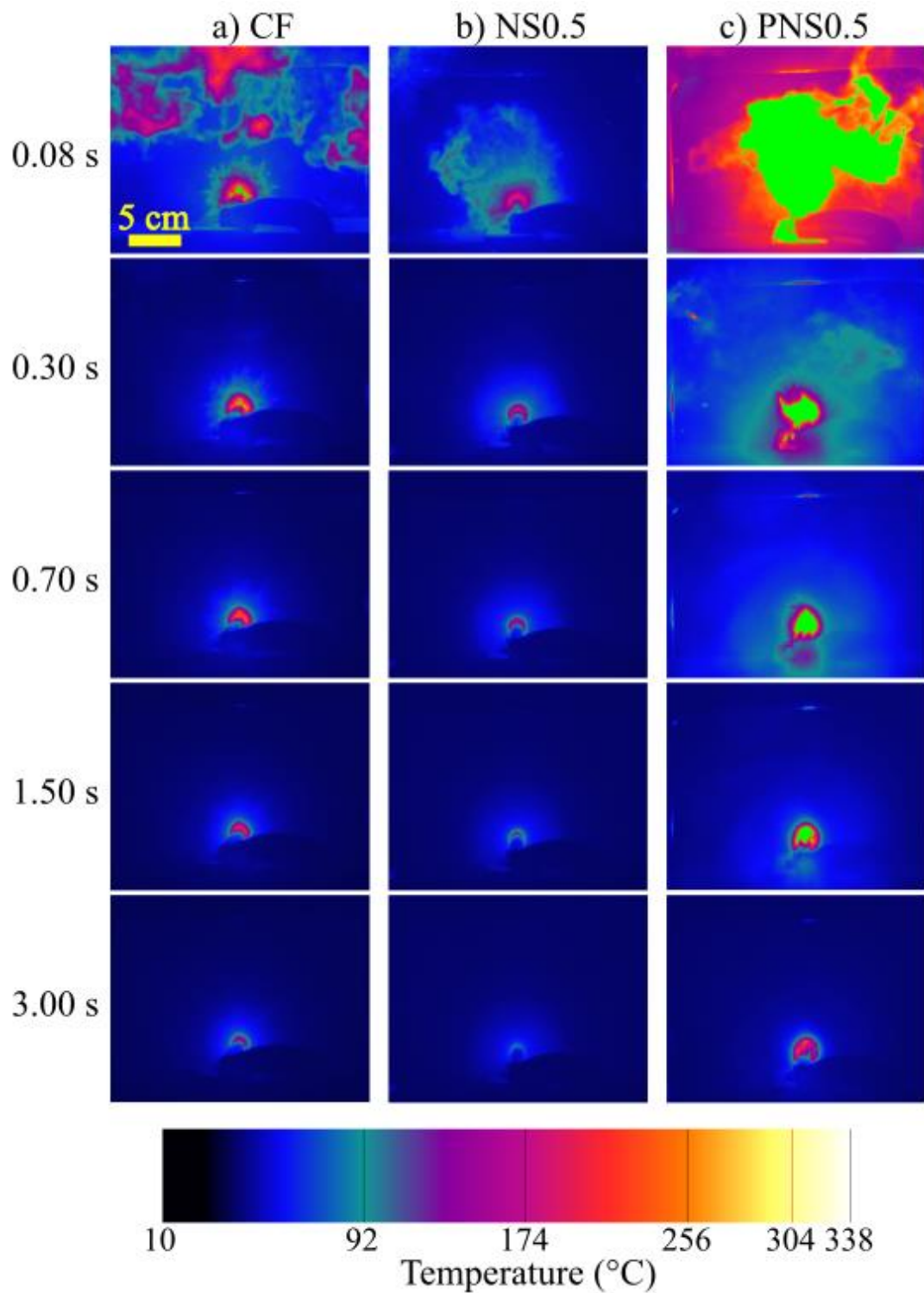


Figure 4.11: Surface temperature of composites panels recorded by the high-speed thermal camera 0.08, 0.30, 0.70, 1.50 and 3.00 s after the LS. a) CF. b) NS0.5. c) PNS0.5.

Several criteria were imagined to characterise the thermal damage: the evolution of the mean or maximum temperature of the panel, the evolution of the temperature at a specific point or the evolution of the area above a temperature threshold. We chose to investigate the last one

as most central pixels were saturated in the first instants after the LS, and sometimes up to 2 s for the painted panels. To choose the temperature thresholds, we thought of using the TGA results. They indicated an onset degradation temperature for the resin of ~ 370 °C and of ~ 250 °C for the paint. The first temperature was too high to be observed by the thermal camera, and we did not need to observe specifically the paint degradation. Hence, we set two temperature thresholds at 100 °C and 200 °C. The evolution of these areas for CF, PCF, NC0.09, NS0.5, NS0.3, PNS0.5 and PNS0.3 are shown in Figure 4.12. Each curve regroups the data of six panels per solution. We did not compute the data of NS0.1 and NS0.04 as the observed values were already low for NS0.5 and NS0.3.

In Figure 4.12.a) and Figure 4.12.b) we compared the behaviours of CF and NC0.09. Since some NC0.09 panels caught fire for a long duration and others only during the first instants, we separated the two groups. The CF panels behaved like the second group. The decrease of the area above 100 °C and 200 °C was exponential. For both temperatures, the area of NC0.09, was larger than CF. After 1 s, CF had an area above 100 °C of ~ 500 mm² and NC0.09 ~ 1000 mm². A higher ratio is observed for the area above 200 °C as CF had an area of ~ 100 mm² and NC0.09 of ~ 250 mm².

In Figure 4.12.c) and Figure 4.12.d) we compared CF with NS0.5 and NS0.3. The decrease is again exponential. After 1 s, both NS have roughly the same area above 100 °C: ~ 100 mm² which is $5\times$ lower than CF. When the smoke dissipated, the surface of the NS panels was already below 200 °C.

Finally, we compared the painted panels PCF, PNS0.5 and PNS0.3 in Figure 4.12.e) and Figure 4.12.f). The decrease was linear, at least the part we could observe. This could be explained by the presence of small flames near the attachment point for a longer duration than for CF. These flames maintained the surface temperature at a higher level. After 1 s, PCF and both PNS had an area above 100 °C of ~ 1000 mm², i.e., $10\times$ larger than NS and $2\times$ larger than CF. After 1 s, the area above 200 °C was ~ 400 mm² for PCF and both PNS while no pixels above 200 °C were recorded for the NS panels.

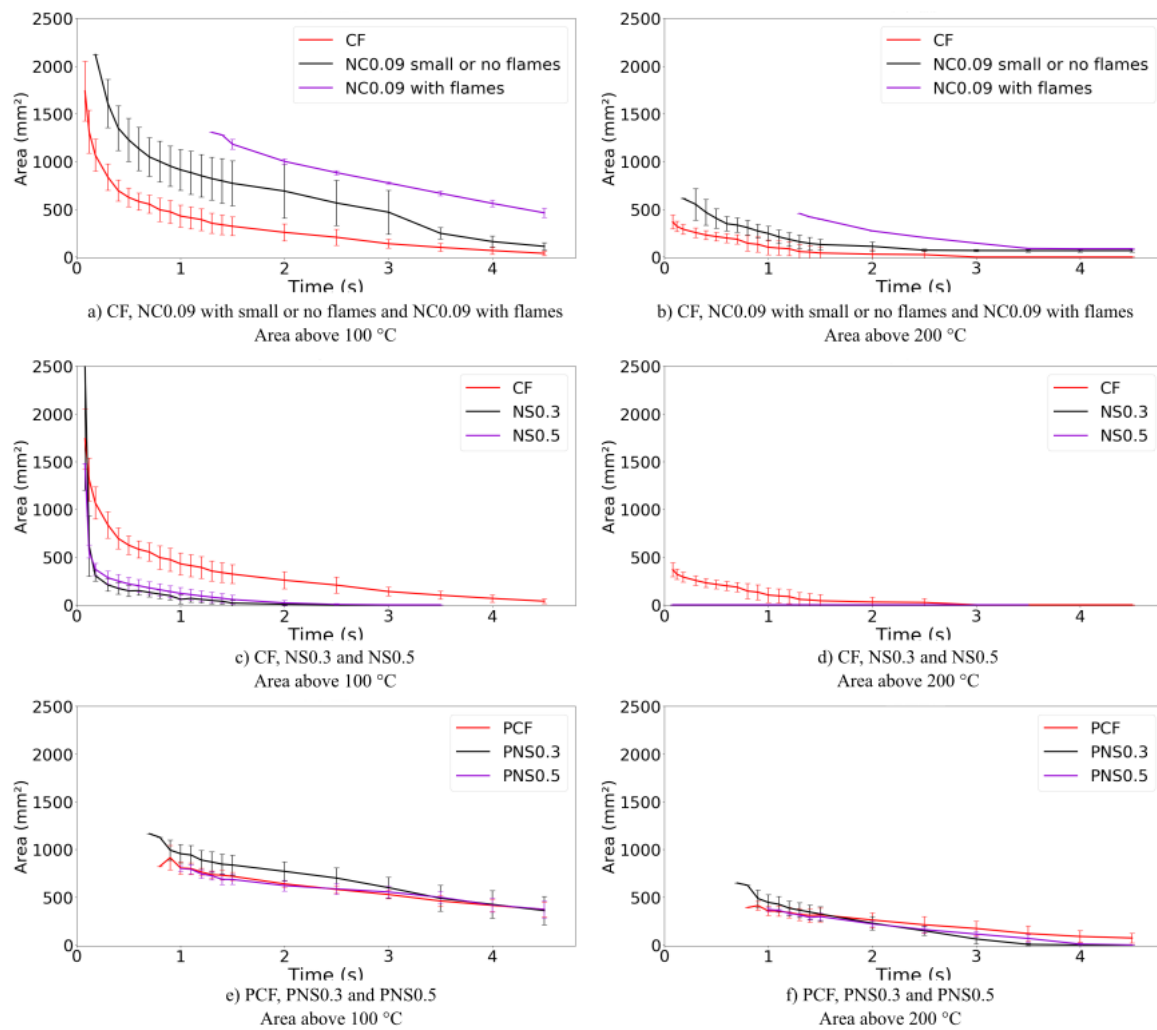


Figure 4.12: Areas above 100 °C (a, c, e) and 200 °C (b, d, f) observed with the high-speed thermal camera. a) and b): CF, NC0.09 panels with small or no flames observed and NC0.09 panels with flames observed. c) and d): CF, NS0.3 and NS0.5. e) and f): PCF, PNS0.3 and PNS0.5.

4.4 Post lightning strike test

4.4.1 Surface damage

After the LS tests, we inspected the damaged panels and tried to identify the first two damage modes, described by *Hirano et al.* [26]: resin pyrolysis area and fibre breakage area. The last one, delamination area, will be identified in the next section.

Top views and close-up views of one damaged nonpainted panel per solution are shown in Figure 4.13. The baseline CF panels, shown in Figure 4.13.a), were severely damaged. The fibre breakage region had a diamond shape with 16 mm long diagonals. The fibres were lifted as if they were broken after an explosion within the laminate. The resin was pyrolyzed on a wider area. No fibre breakage was observed on the ECF, as shown in Figure 4.13.b). The copper foil was evaporated near the attachment point and damaged on a wider area shaped like a diamond, with 30 mm and 35 mm long diagonals

More disparities were observed among the NC0.09 panels. Indeed, some panels had broken fibres on a similar area than the CF, as shown in Figure 4.13.c), while others had no broken fibres. These disparities could be explained by the manual wet lay-up process used to integrate the woven NCCF: some panels most likely had more resin than others. The nickel coating was evaporated on all the damaged fibres as well as on multiple spots around the attachment point.

The damage on the NS panels were circular and less severe than NC0.09 or CF, as shown in Figure 4.13.d)-g). Broken carbon fibres from the structural plies were observed on most NS0.5 and NS0.3 panels with, respectively, a ~10 and ~9 mm wide damaged area. The nonwoven veil was damaged and evaporated on the NS0.5, NS0.3 and NS0.1 panels near the attachment point. The resin pyrolysis area decreased with the conductivity of the NW, with a diameter of 26, 20, 17 and 12 mm, for NS0.5, NS0.3, NS0.1 and NS0.04, respectively. The damage to the sacrificial layer followed a checkerboard pattern: the nonwoven layer was more damaged where the warp and weft carbon fibre yarns crossed. Indeed, the contacts between the first carbon fibre ply and the LSP layer, observed in Section 4.2.3, occurred mostly in these locations. Because of the contact resistance, the Joule heating was more intense in these spots and the nonwoven layer was more damaged.

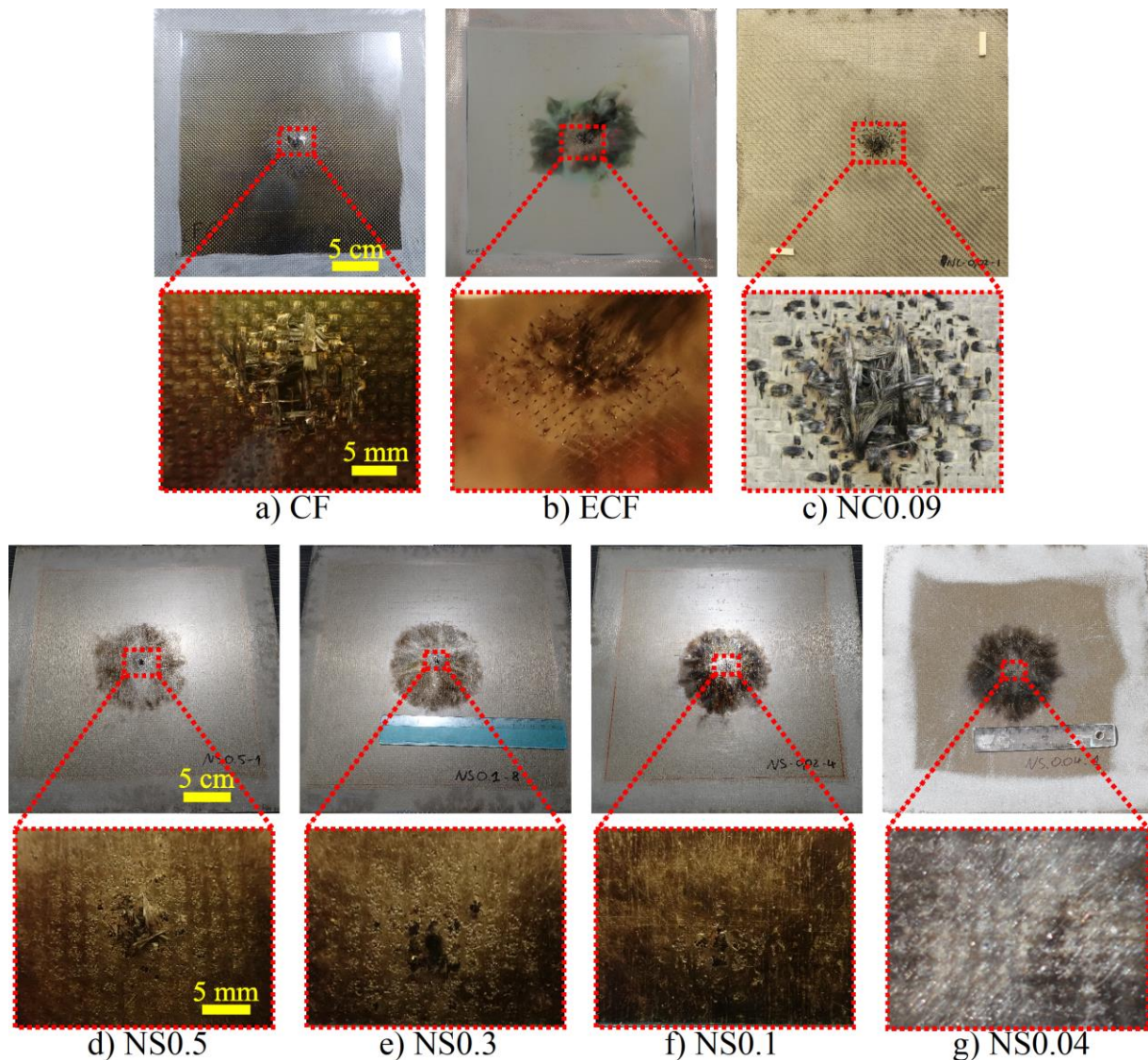


Figure 4.13: Top and close-up views of one damaged nonpainted panel per solution. a) CF. b) ECF. c) NC0.09. d) NS0.5. e) NS0.3. f) NS0.1. g) NS0.04.

All painted panels were more severely damaged than their nonpainted equivalent, except for the ECF solution, as shown in Figure 4.14. The PCF panels, shown in Figure 4.14.a), had a larger diamond-shaped fibre breakage area than CF, with ~ 30 mm long diagonals, i.e. a $4\times$ larger damaged area. The paint previously covering the damaged area was vaporised or projected, as many loose paint flakes were found on the panels after the LS test. This projection could be explained by the overpressures created below the paint layer, as explained in Section 2.2.1.3. The damage on the PECF, shown in Figure 4.14.b), were similar to the one reported earlier for the ECF: the copper foil damage followed a diamond-shaped pattern with 30 mm and 35 mm long diagonals.

No painted panels protected by a woven NCCF cloth were tested. As shown in Figure 4.14.c)-f), the damage to the PNS panels consisted of a circular fibre breakage area, surrounded by a region without paint, revealing the nonwoven veil and the resin pyrolysis area. Loose paint flakes were found on the panel after the LS test, like on the PCF panels. However, more paint was removed from the panels, maybe because its adhesion with the nonwoven veil was poorer than with the carbon fibre ply. The heating of the LSP layer, due to the Joule effect, might also have damaged the paint layer, favouring its evaporation or projection. All the PNS0.5, PNS0.3 and PNS0.1 panels had a similar fibre breakage area with a ~23 mm diameter. The PNS0.04 panels fibre breakage area was smaller than the other PNS panels with a ~20 mm diameter.

4.4.2 Internal damage

The surface damage analysis gave us information on the first two damage modes: resin pyrolysis area and fibre breakage area. In this section, we focused on the last one: the delamination area. We also observed the depth of the damage. We used three methods to characterise the internal damage: an ultrasonic scan (C-Scan), a visual cross-section observation, and a μ -CT scan. For the last two methods, only one sample per solutions was observed. In Table 4.5, we compare the internal damage area observed with the first two methods and the depth of the damage observed with the last two methods.

4.4.2.1 C-scan

All the pixels near the attachment point showing an attenuation of 14 dB, or higher, were considered as damaged. Unfortunately, no distinction between fibre breakage, delamination or smaller defects is done.

The C-Scan of one damaged nonpainted panel per solution are shown in Figure 4.15. CF, NC0.09 and all the NS panels had a circular-shaped damage. NS0.04 panels were barely damaged. The ECF had a diamond-shaped damage, as shown in Figure 4.15.b). A significant damaged area was visible on all panel, except NS0.04. It shows that, even if no fibre breakage was observed on the surface, like for the ECF panels, the laminate can still be internally damaged.

The C-Scan of one damaged painted panel per solution are shown in Figure 4.16. The PECF panels appeared almost undamaged on the C-Scan. The PNS panels had wider circular

damage than their nonpainted counterparts. The ultrasonic scans confirmed an important internal damage of the PNS panels that was implied by the important fibre breakage observed on the surface of the PNS panels, and the flames observed on the thermal camera. The C-Scan of PNS0.04 showed huge disparities. Three panels had a small circular damage, as shown in Figure 4.16.f), while the three others had an unconventional damage shape, as shown in Figure 4.16.g): a damaged centre, an undamaged ring around it and around this ring some damaged areas like petals.

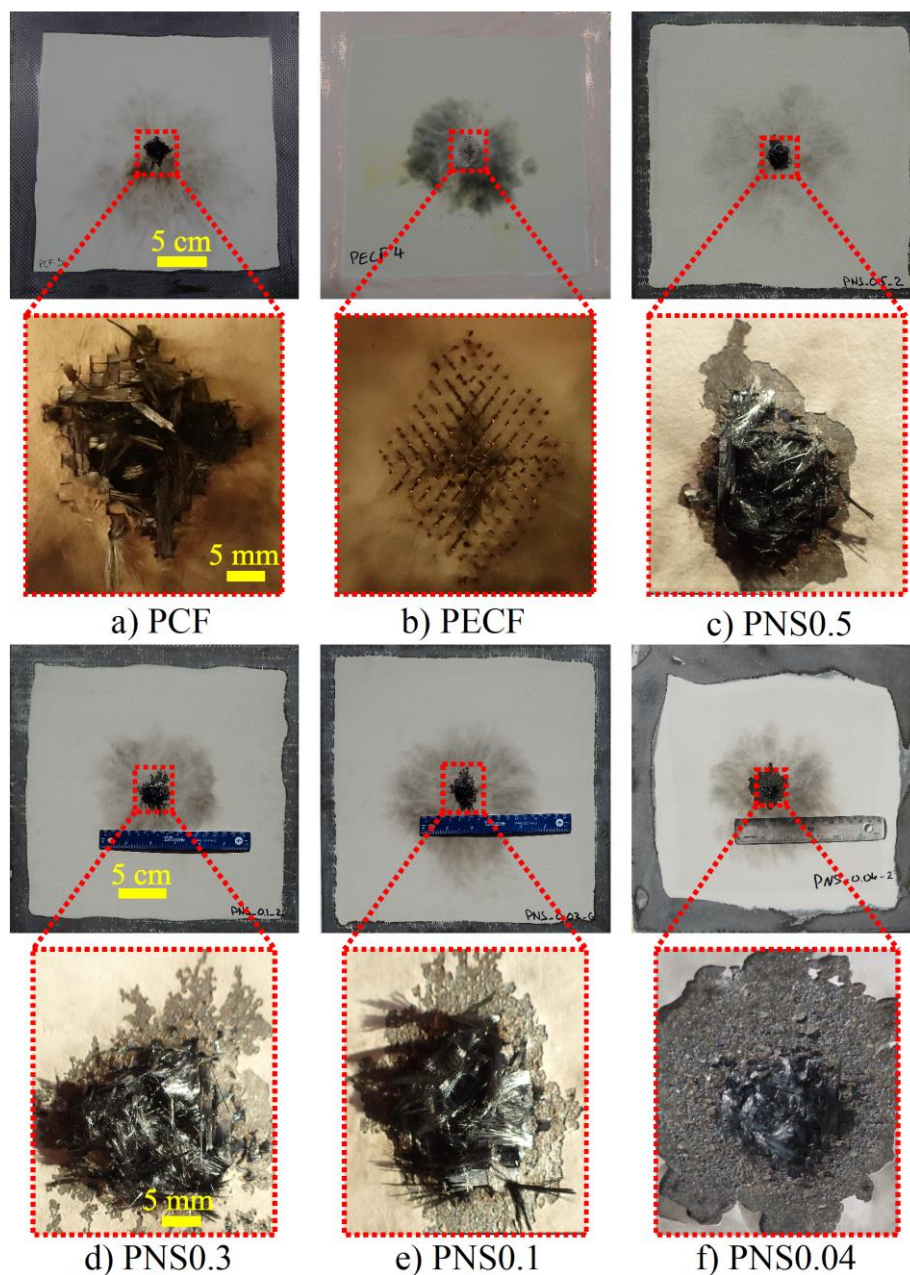


Figure 4.14: Top and close-up-views of one damaged painted panel per solution. a) PCF. b) PECF. c) PNS0.5. d) PNS0.3. e) PNS0.1. f) PNS0.04.

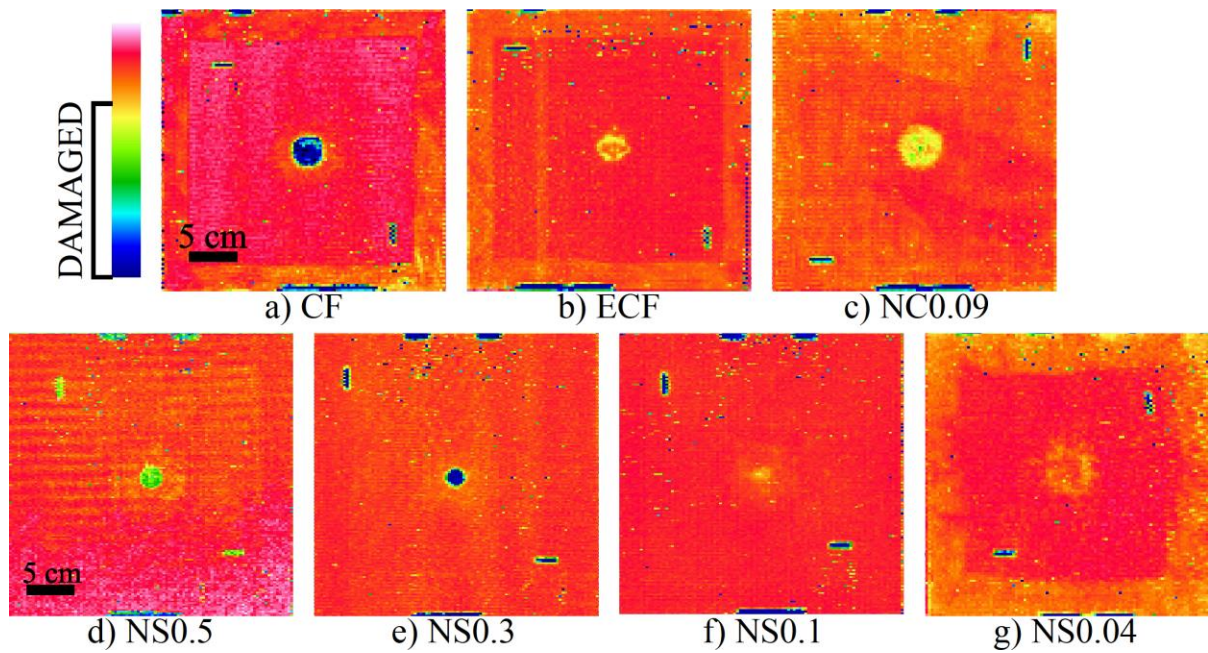


Figure 4.15: C-Scan of one damaged nonpainted panel per solution. a) CF. b) ECF. c) NC0.09. d) NS0.5. e) NS0.3. f) NS0.1. g) NS0.04.

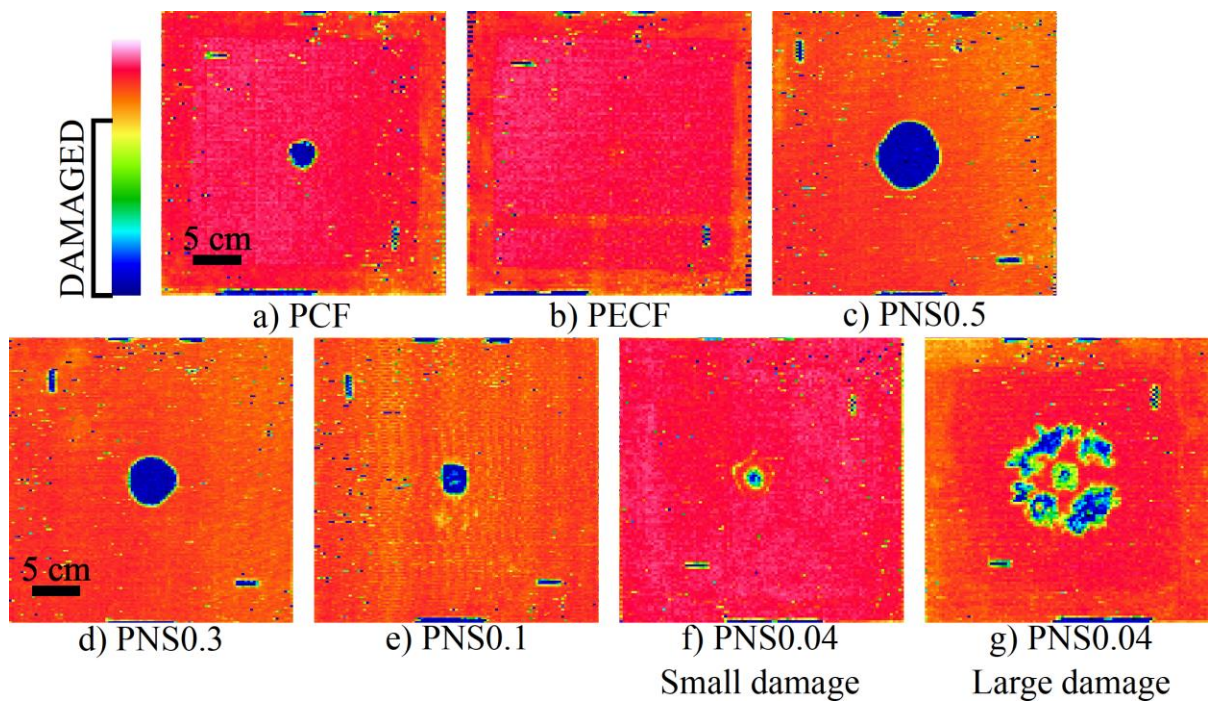


Figure 4.16: C-Scan of one damaged painted panel per solution. a) PCF. b) PECF. c) PNS0.5. d) PNS0.3. e) PNS0.1. f) PNS0.04 with a small damage. g) PNS0.04 with a large damage.

The damaged area measured by C-Scan are shown in Figure 4.17. The CF panels were the most damaged among the nonpainted panels with a damaged area of $956 \pm 86 \text{ mm}^2$. For the NC panels, we measured a damaged area of $669 \pm 603 \text{ mm}^2$ with the C-Scan (#2, 3 and 4

below 310 mm², the others, like the one in Figure 4.15.c), above 970 mm²). These measurements confirm the disparities observed visually. The damaged area measured for NS0.5, NS0.3 and NS0.1 were between 500 and 700 mm², with no clear difference between the three solutions. Despite the limited damage observed on the surface, i.e., a small resin pyrolysis area and an even smaller fibre breakage area, it seems that the internal structure of the panels was damaged by the LS. The NS0.04 panels were the least damaged ones among the nonpainted panels, with an average damaged area of 23 ± 22 mm², 20× less than the ECF panels at 460 ± 35 mm².

Surprisingly, the PCF panels had a smaller damaged area than CF panels, while the surface damage tended to show the opposite. The PECF panels had, in average, a 4× smaller damaged area than the ECF, as if the paint protected the internal structure of the laminate. The PNS panels had a 2 to 3.5× larger damaged area than their nonpainted counterparts, but it seemed that the damaged area decreased with the sheet resistivity of the laminate. This trend was not visible with the surface damage observations or the thermal camera images.

We added resin to the majority of the PNS0.1 panels, which could explain the larger disparities observed on the C-Scan data, in comparison to PNS0.5 and PNS0.3. Half of the panels had a damaged area below 800 mm² (#5, 6 and 7 with 796, 569 and 735 mm²) and the other half above 1200 mm² (#2, 3 and 4 with 2369, 1879 and 1238 mm²). The different damage patterns observed for PNS0.04 were visible in the measured damaged areas. The first three panels had damage areas below 450 mm², i.e., in the same range as ECF, while the other three panels had damaged areas of 2630, 6000 and 7200 mm², i.e., the largest damaged areas measured with C-Scan. These last three panels were not considered for the calculation of the average damaged area showed in Figure 4.17. The unconventional damage shape could be explained by the poor integration process and the porosities observed in the PNS0.04 panels. However, these porosities were observed on all panels but only three panels had unconventional C-Scan results.

We found no clear correlation between the areas measured with the thermal camera and the damaged areas measured with the C-Scan. For example, for the NS and PNS panels: the NS do have a smaller damaged area than CF, but the damaged areas for PNS are larger than PCF, which is the opposite of what was observed on the thermal camera images.

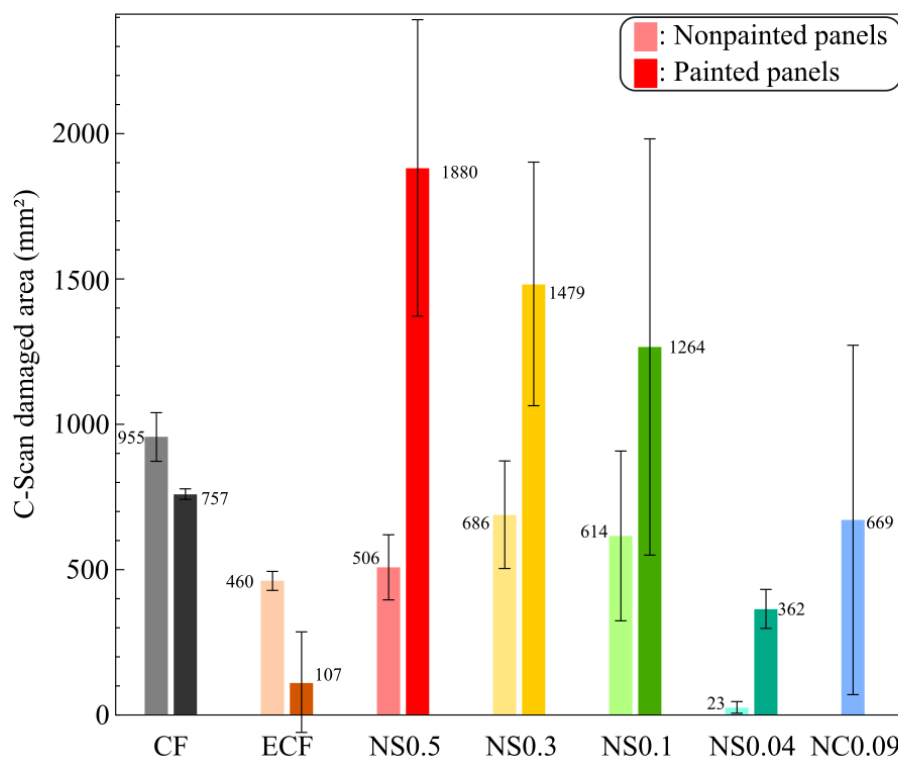


Figure 4.17: Damaged area of the nonpainted and painted panels measured with C-Scan using a 14 dB attenuation criteria

4.4.2.2 Visual cross-section observation

In Figure 4.18 we show the internal damage of the nonpainted panels observed in the cross-section. The CF panel (a) was severely damaged by the LS. The fibres of the first ply were broken and a 32.2 mm wide delamination between the first three plies was observed. On the ECF panel (b), the only visible damage was the evaporated copper mesh near the attachment point.

Both the NS0.5 (c) and NS0.3 (d) panels were delaminated between the first two carbon fibres/epoxy plies on a 23 and 19.6 mm length respectively, without fibre breakage. However, broken fibres were observed on others NS0.5 and NS0.3 panels, like in Figure 4.13. The cross-section observation of the NS0.1 (e) and NS0.04 (g) panels revealed no significant internal damage. It seems that the internal damage significance decreases with the sheet resistivity of the laminate protected by the nonwoven NCCF. The NC panel (g) was delaminated between the woven NCCF and the first carbon fibre ply on a 31.3 mm length, without fibre breakage. However, this panel was less damaged than other NC panels. Indeed, broken carbon fibres were observed on the surface of other NC panels.

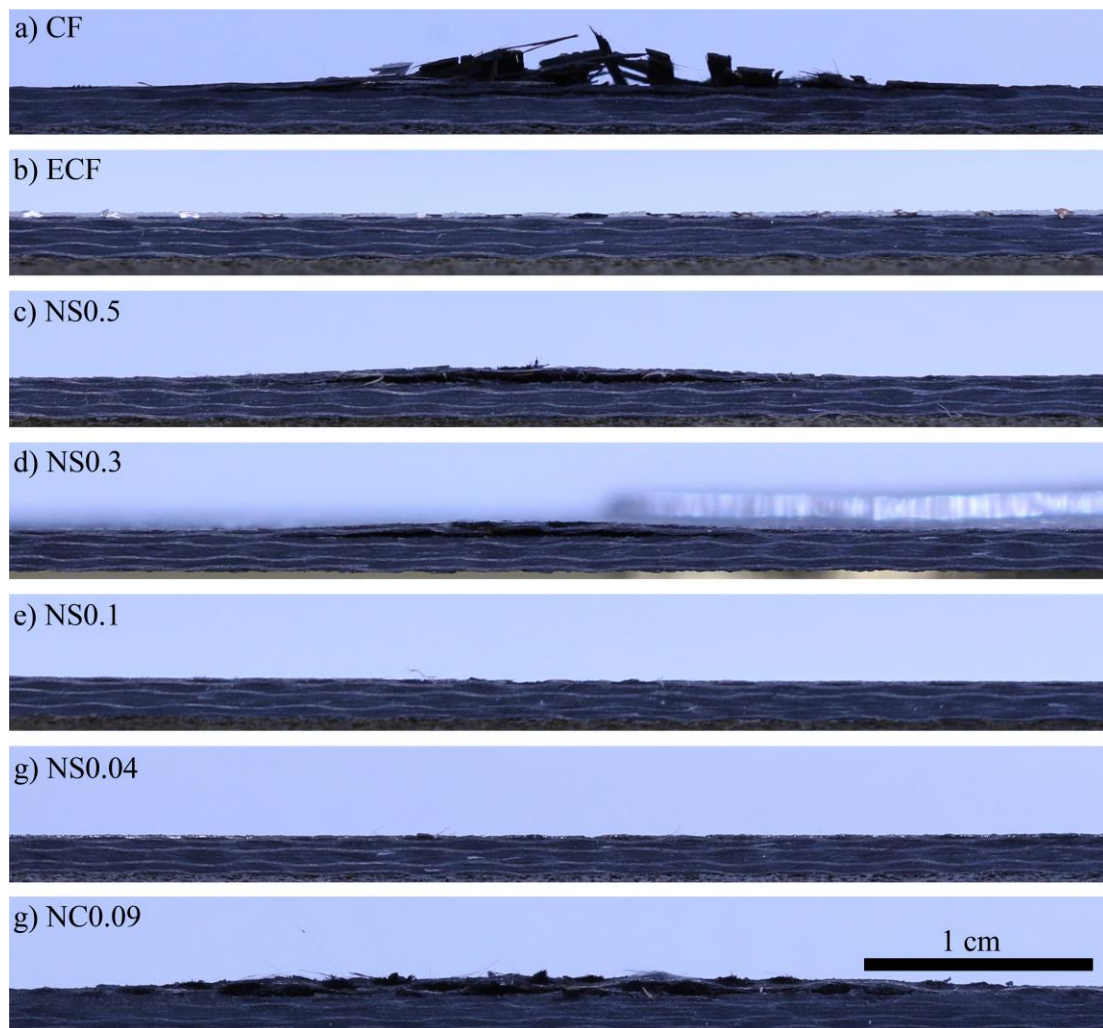


Figure 4.18: Damaged nonpainted panels cross-section observation. a) CF. b) ECF. c) NS0.5. d) NS0.3/ e) NS0.1. f) NS0.04. g) NC0.09. CF: Fibre breakage + delamination. NS0.5, NS0.3 and NC: delamination. ECF: evaporated copper foil. NS0.1 and NS0.04: no visible damage.

The delamination without fibre breakage observed on some NS0.5, NS0.3 and NC0.09 panels could be caused by the resin pyrolysis between the plies that increased the internal pressure of the laminate. This pressure was high enough to lift the first ply but too low to burst the carbon fibres.

The internal damage of the painted panels are shown in Figure 4.19. The PCF panel (a) was the most damaged panel. The carbon fibres of the first four plies were broken and a 44.4 mm wide delamination was observed between the second and third plies, as well as other smaller delamination between the first five plies. Like on the ECF panel, the evaporated copper foil near the attachment point was the only damage observed on the PECF panel (b).

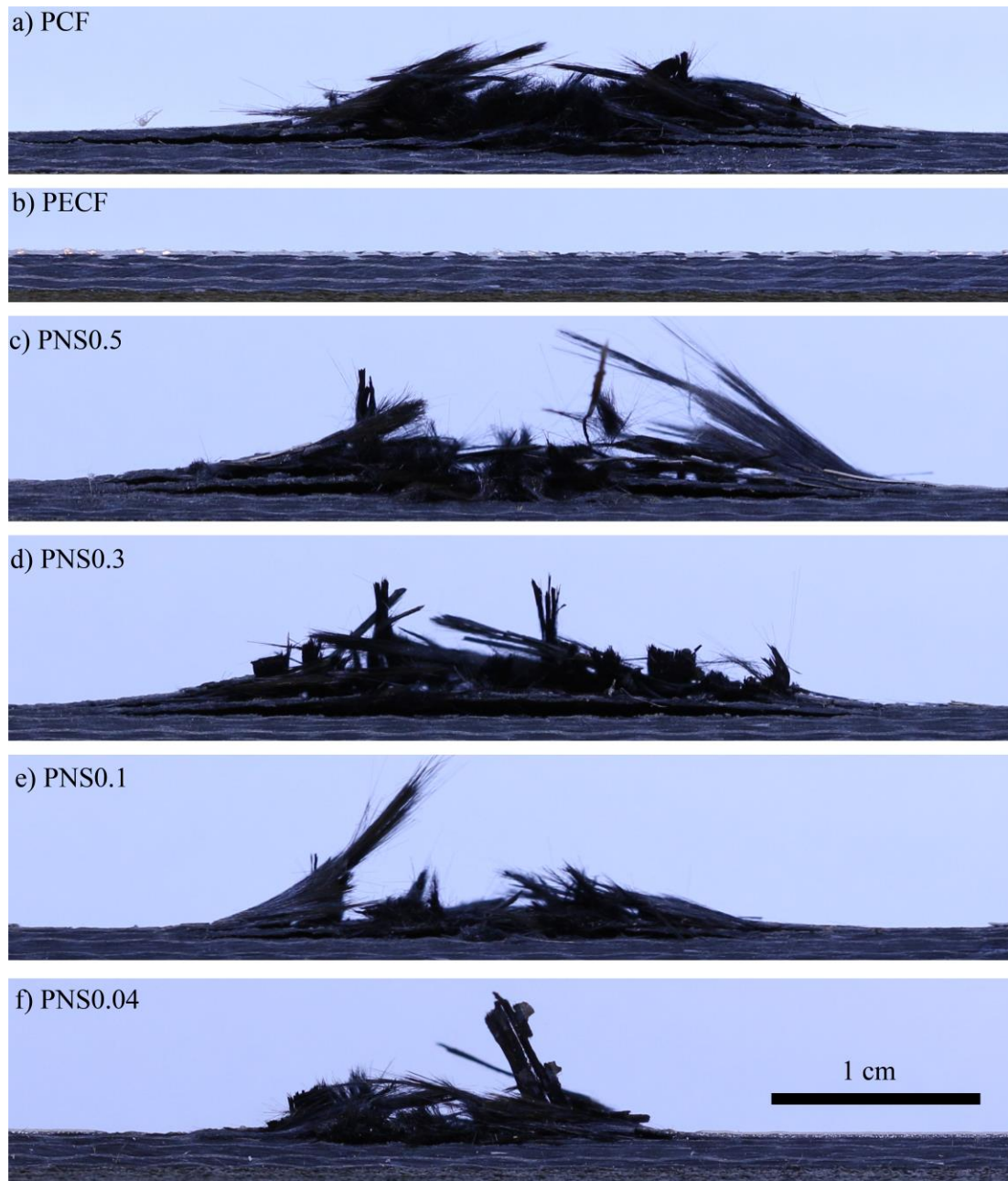


Figure 4.19: Damaged painted panels cross-section observation. a) PCF. b) PECF. c) PNS0.5. d) PNS0.3. e) PNS0.1. f) PNS0.04. PCF, PNS0.5, PNS0.3, PNS0.1, PNS0.04: Fibre breakage + delamination. PECF: evaporated copper foil.

All the PNS panels (c-e) had broken fibres and were delaminated, but the damage were smaller than for the PCF panel. The more conductive the nonwoven was, the less deep and wide was the damage. We measured delamination of 40.2, 35.2 and 30.1 mm long for the PNS0.5, PNS0.3 and PNS0.1 panels, respectively. On the PNS0.5 panel (c), the carbon fibres of the first three plies were broken. On the PNS0.3 (d), PNS0.1 (e) and PNS0.04 (f) panels the carbon fibres were broken on the first two plies. The broken carbon fibres of the painted

panels were lifted. This observation confirmed the damage mechanism of painted panels explained in Chapter 2: the pyrolysis gas were trapped inside the laminate, below the paint layer. When the internal pressure was too high, the laminate imploded. The carbon fibres of the first plies were broken in the centre of the damaged area and the first plies were lifted, inducing delamination on a wider area.

4.4.2.3 X-ray microtomography (μ -CT)

The μ -CT scan was performed on one 12.7×90.0 mm sample per solution. The scan reconstructed a 3D model of the sample in which we could move and observe the different cross-sections. As metals interact with the μ -CT, they appear brighter than other materials on the images, making the interpretation of the ECF and PECF samples complex. To obtain the damaged depth in terms of ply and compare it with the visual observation results, we measured the maximum damage depth and compared it with the thickness of an undamaged section. This gave us a percentage of damaged section that we converted in a number of plies.

In Figure 4.20, we show the top and cross-section views obtained for NS0.5 (a) and NS0.1 (b). On the NS0.5 sample top view, we observed that the nonwoven NCCF veil was vaporised and that carbon fibres were broken on at least the first ply of the laminate. A delamination was observed on both cross-section views (circled in yellow) and a damage depth of 1 to 2 plies was observed. The same type of damage was observed on NS0.3. On the NS0.1 sample, we observed the checkerboard damage pattern of the nonwoven but no fibre breakage or delamination. However, some cracks were visible on the cross-section view between the first two carbon fibre ply. These cracks were not visible on the visual cross-section observations.

The images of the other samples are not shown. Indeed, they bring almost the same information as the cross-section visual observations, revealing only small cracks below the first non-delaminated ply on all NS and PNS samples. These cracks were not considered in the damaged depth calculation.

In Table 4.5, we compare the results of the internal damage obtained with three different methods. For the C-Scan, the diameter of the internal damage was calculated from the average damaged area for the circular-shaped damage. For ECF and PECF we considered a diamond-shaped area. For all panels protected by a nonwoven NCCF, the C-Scan damaged area was larger than the one observed visually. The damaged area observed visually, i.e., the delamination area, decreased with the sheet resistivity of the protection layer. Indeed, the

lower the sheet resistivity was, the less the current was conducted by the baseline laminate and the smaller the overpressures created by the resin pyrolysis.

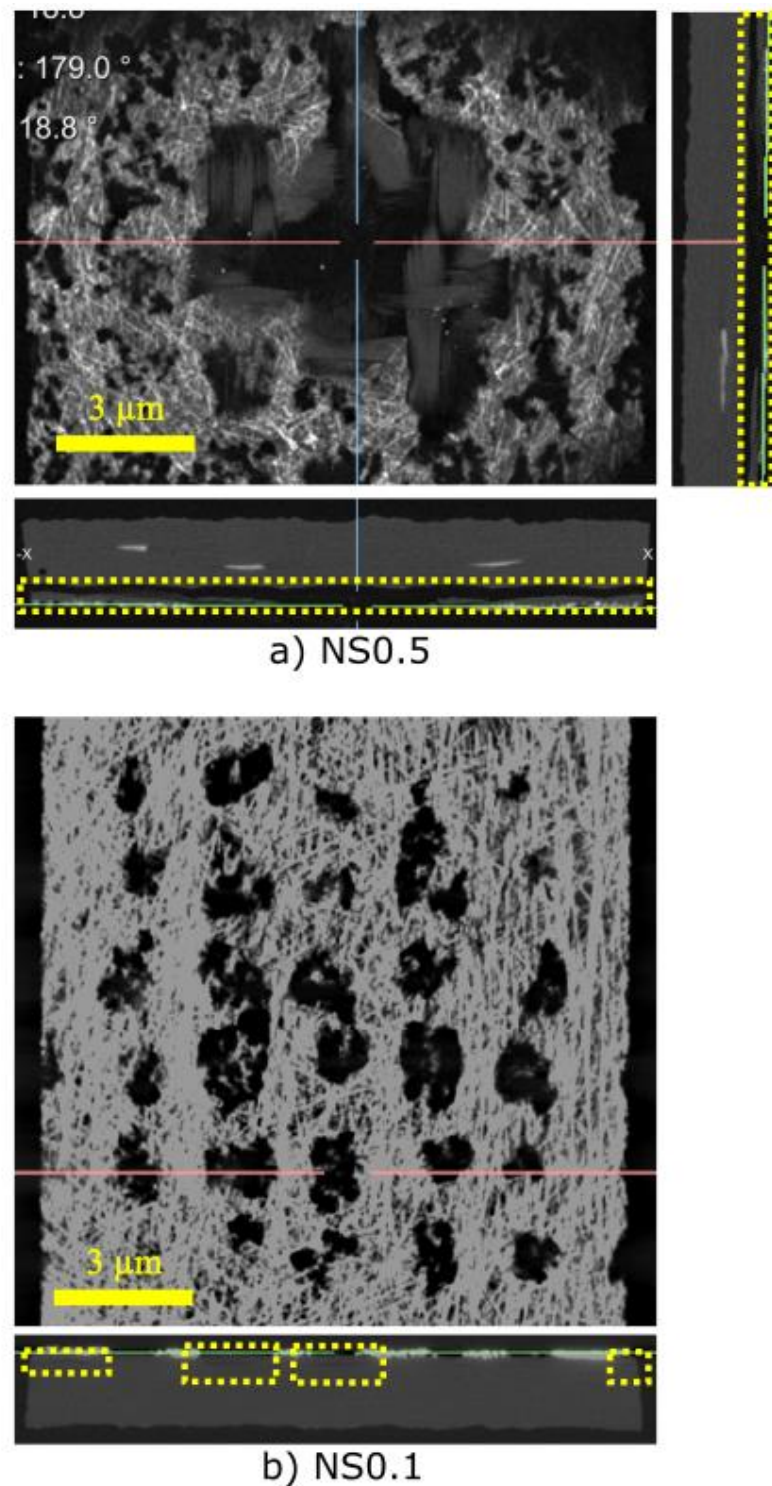


Figure 4.20: X-ray microtomography observations of a) NS0.5 panel with a top and two cross-section views. b) NS0.1 panel with a top and one cross-section view. Circled in yellow:
a) delamination, b) small cracks between the first two plies.

Table 4.5: Diameter of the internal damage, in mm, and damage depth, i.e., the number of damaged plies, of each solution after LS test. Measured with C-Scan, cross-section observation (visual) and X-ray microtomography (μ -CT). * = Diamond-shaped damage, the values are the length of the diagonals not the diameter.

Solution	Diameter of internal damage (mm)		Damage depth (number of ply)	
	Visual	C-Scan	Visual	μ -CT
CF	32.2	34.9	2	2-3
ECF	0	28×33*	0	0
NS0.5	23	25.4	1	1
NS0.3	19.6	29.6	1	1
NS0.1	0	28.0	0	1
NS0.04	0	5.4	0	0
NC0.09	31.3	29.2	2	3
PCF	44.4	31.0	5	5
PECF	0	14×16*	0	0
PNS0.5	40.2	48.9	4	5
PNS0.3	35.2	43.4	3	2-3
PNS0.1	30.1	40.1	3	2-3
PNS0.04	18.4	21.5	2	2-3

We were not able to explain the damaged area observed with the C-Scan and the lack of correlation with the other measurements. For example, on the NS0.1 panels, only small cracks were seen with the μ -CT scan, but the panels appeared damaged on a 28.0 mm wide area on the C-Scan and the observed resin pyrolysis area on the surface was ~17 mm wide. On the contrary, the PCF samples had a much wider internal damage than measured with the C-Scan.

The damage depth measured by visual observation and μ -CT scan were in the same range for almost every solution. Since only one panel per solution was observed for each method, we do not have enough information to discuss about the differences observed. However, we can assume that, for each solution, the other four panels had a damage depth in the range shown in this table. For the NS and PNS panels, the damage depth decreased with the sheet resistivity of the LSP layer, most likely for the same reason as the damaged area.

When comparing the surface and internal damage observed in Sections 4.4.1 and 4.4.2 with the thermal camera data detailed in Section 4.3.2, we observed that all panels showing carbon fibre breakage in the first plies caught fire after the LS test. It lasted a short duration (few 10s of ms) for the CF, NS0.5, NS0.3 and some NC0.09 panels, or a longer one (0.8-1 s) for the rest of the NC0.09 panels, and for the PCF and PNS panels. We attributed these flames to some compounds from the pyrolysates, the gas produced by the resin pyrolysis, that ignited in contact with the oxygen [25]. The larger the internal damage, the larger the quantity pyrolysates and the longer the fire lasted. These flames maintained a high temperature close to the panel surface, and most likely increased the significance of the damage hundreds of milliseconds after the LS.

4.4.3 4 points bending test

As explained in Section 3.4.4, we measured the mechanical properties of each solution before and after the LS test with a 4-point bending test (4PBT) with the damaged side in tension. The flexural strength and the effective bending stiffness of each solution before and after the emulated lightning strike test were calculated using equations (3.2) and (3.3). The results are listed in Table 4.6. The properties are normalised with the thickness of the 8 structural plies: 1.61 mm for (P)NS0.04 and 1.69 mm for all other panels. As explained in Section 3.2.1, the CF/epoxy prepregs used for the integration of (P)NS0.04 were thinner than all the other.

Before the LS test, the baseline laminate had a flexural strength of 753.7 MPa and an effective bending stiffness of 37.7 GPa. The addition of a NCCF-based LSP or the ECF had no significant effect on the mechanical properties of the laminate.

The poor integration process of PNS0.04 had a significant effect on its mechanical properties, as it decreased by 17% and 37% for, respectively, the effective bending stiffness and the flexural strength. A new batch of (P)NS0.04 panels will be manufactured to confirm the results observed in this master thesis.

The mechanical properties in the 0° and 90° directions were the same, as the laminate were quasi-isotropic.

Table 4.6: Flexural strength and effective bending stiffness before and after LS for each solution. The results for all materials are normalised with the thickness of the structural plies: 1.61 mm for NS0.04 and PNS0.04 and 1.69 mm for all the other panels.

Solution	Effective bending stiffness (GPa)			Flexural strength (MPa)		
	Before LS	After LS	Retention (%)	Before LS	After LS	Retention (%)
CF	37.7 ± 3.4	19.7 ± 0.7	52.2	753.7 ± 23.3	426.2 ± 43.2	56.5
ECF	38.5 ± 2.2	36.0 ± 2.6	92.5	773.4 ± 46.0	639.4 ± 149.5	82.7
NS0.5	41.3 ± 0.8	35.5 ± 1.1	86.1	811.1 ± 20.9	561.9 ± 9.2	69.3
NS0.3	40.3 ± 0.8	35.8 ± 2.0	88.8	789.5 ± 17.3	554.7 ± 19.9	70.3
NS0.1	38.2 ± 0.7	38.9 ± 1.1	100	771.4 ± 48.9	648.8 ± 20.1	84.1
NS0.04	39.7 ± 1.0	41.1 ± 2.5	100	733.4 ± 32.9	707.4 ± 57.0	96.5
NC0.09	43.7 ± 1.8	25.7 ± 4.2	58.8	798.7 ± 26.6	500.9 ± 39.6	62.7
PCF	39.1 ± 13.9	12.1 ± 1.2	30.9	834.0 ± 57.7	206.3 ± 32.9	24.7
PECF	38.0 ± 2.1	35.1 ± 1.2	92.4	756.9 ± 49.3	623.0 ± 79.8	82.3
PNS0.5	42.0 ± 1.2	12.3 ± 1.3	29.3	823.7 ± 54.3	197.8 ± 28.0	24.0
PNS0.3	41.4 ± 1.4	17.1 ± 1.7	41.3	823.0 ± 26.9	301.2 ± 72.6	36.6
PNS0.1	40.9 ± 1.5	17.7 ± 1.9	43.2	807.1 ± 34.7	328.3 ± 41.7	40.7
PNS0.04	33.2 ± 6.5	20.0 ± 1.0	60.4	462.2 ± 117.4	319.9 ± 40.0	69.2

As the flexural strength and the effective bending stiffness were not in the same range for all solutions, we chose to compare the retention of these mechanical properties after the LS test, as shown in Figure 4.21 and Figure 4.22. CF retained 57% of its flexural strength and 52% of its effective bending stiffness. The reference LSP solution, ECF, retained 83% and 93%, respectively. Hence, despite the absence of internal damage observed with the μ -CT or visually in Section 4.4.2, the damaged ECF panels showed reduced mechanical properties. NC0.09 did not perform better than CF, as its mechanical properties retention were in the same range as the baseline laminate.

NS0.5 and NS0.3 performed similarly with better results than CF. They retained 69% and 70% of their flexural strength and 86 and 89% of their effective bending stiffness, respectively. Indeed, the flexural strength is more sensitive to delamination than the effective bending stiffness [86]. For those two solutions, the first carbon fibre ply was only damaged on some locations and the main internal damage was a delamination between the first two plies.

NS0.1 and NS0.04 had the same or higher flexural strength retention as ECF with 84% and 97%, respectively, and a better effective bending stiffness retention with 100%. The flexural strength decrease could be attributed to the small cracks, or pre-delamination, observed with the μ -CT.

When the panels were painted both mechanical properties were decreased for all solutions, except for PECF, which retained the same properties as ECF. The low damaged area of PECF measured with the C-Scan was not visible on the mechanical properties retention. PCF retained only 27% of its flexural strength and 33% of its effective bending stiffness. PNS0.5 had worst properties than PCF. The difference between PNS0.5 and PNS0.3 increased when the paint was added, as PNS0.3 retained 37% of its flexural strength and 42% of its effective bending stiffness, when PNS0.5 retained only 29% and 24%. Even the mechanical properties retention of the PNS0.1 were divided by 2 when compared with its nonpainted counterparts. Paint seemed to have a smaller effect on PNS0.04 with a 28% decrease. For both the NS and PNS panels, the less electrically resistive the panels were, the higher their mechanical properties retention.

These poor mechanical properties can be explained by the broken carbon fibres of the first plies, as seen in Figure 4.19. As there can be no mechanical charge transfer in a ply if the carbon fibres are not continuous and the resin is evaporated, only a reduced number of plies participate in the mechanical effort, and the mechanical properties decrease.

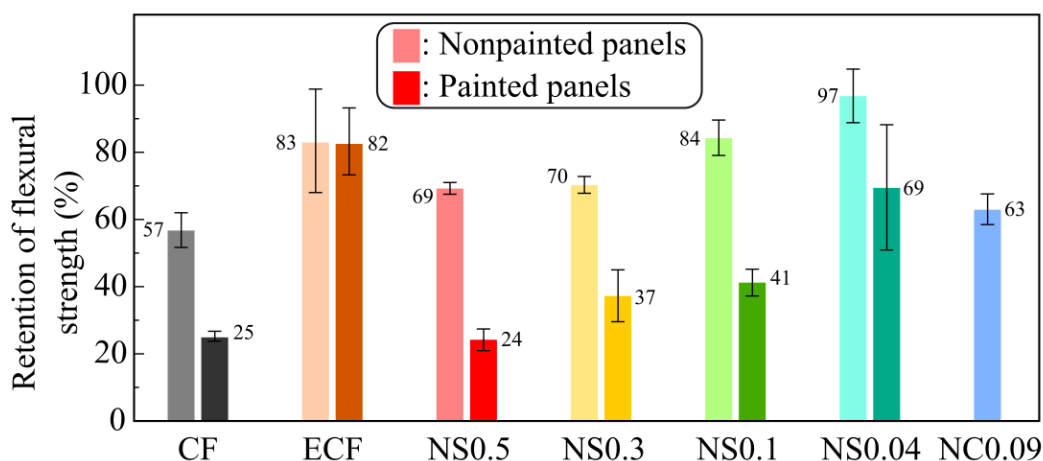


Figure 4.21: Flexural strength retention of nonpainted and painted panels after LS test. Measured with a 4-point bending test.

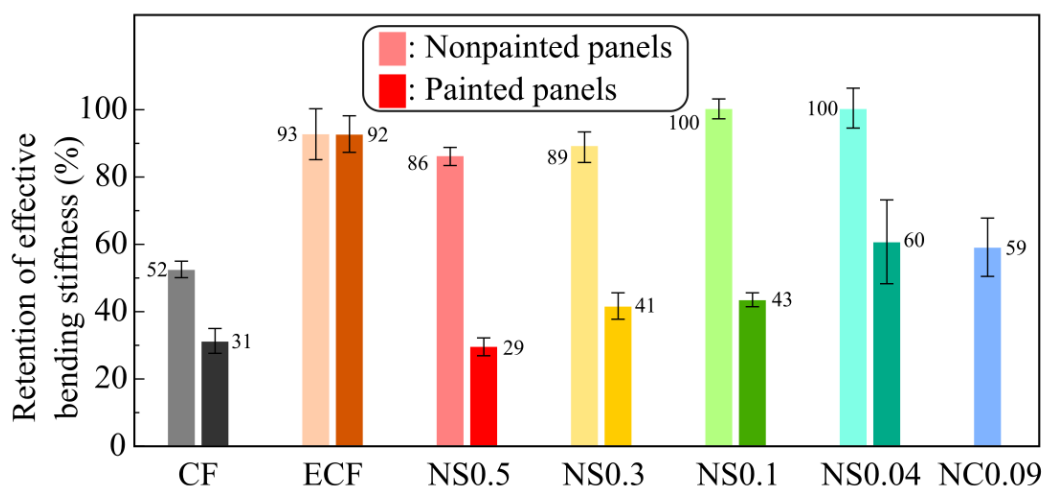


Figure 4.22: Effective bending stiffness retention of nonpainted and painted panels after LS test. Measured with a 4-point bending test.

4.5 Cost

Finally, we compared the price of each LSP layer in Figure 4.23, in terms of percentage of the expanded copper foil reference price. NW0.3 was bought as a NW0.1, but the measured sheet resistivity was higher than expected. Hence, another NW0.1 roll was bought. The woven NCCF costed $1.54\times$ the price of the ECF. All nonwoven solutions were cheaper than the ECF.

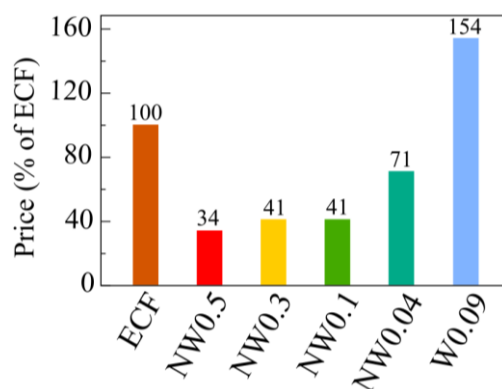


Figure 4.23: Price of the LSP layers, in terms of percentage of the expanded copper foil reference price. NW0.3 was bought as a NW0.1, but the measured sheet resistivity was higher than expected.

4.6 Damage mechanisms and discussion on LSP efficiency

The damage mechanisms describe in these sections are hypothetical. They are based on the literature and our understanding of the phenomena.

4.6.1 ECF and PECF

For the ECF and PECF panels, it seemed that the current injected on the panel surface was only conducted by the copper mesh and never penetrated in the baseline laminate, possibly because of the thin resin layer below the mesh. The copper mesh and the surrounding resin were locally vaporised, but the baseline laminate was left almost intact. Hence, the ECF and PECF panels owed their LSP efficiency to a highly conductive mesh that dispersed the lightning strike energy and allowed the exit of the pyrolysis gas. However, a portion of the copper network was vaporised to absorb the remaining LS energy.

4.6.2 NS and CF

The nonwoven NCCF has a lower sheet resistivity than the copper foil. Hence, it can not disperse the LS energy as easily as the copper foil. However, it can absorb more energy from the lightning strike. After the nickel melting and vaporising, that already absorbed a portion of the LS energy, the carbon fibre network is still intact. This network is conductive and can withstand temperatures higher than 3,000 °C. Furthermore, the sublimation of the carbon fibres requires a lot of energy, at least 10× more than copper or nickel, as explained in Section 4.2.2. Hence, the conductive network provided by the nonwoven veil can not be as easily destroyed by the Joule effect as the copper foil. *Guo et al.*[56] reported that the carbon fibre network of a nonwoven NCCF veil was intact after a 100 kA strike.

The damage mechanism of the NS panels is illustrated in Figure 4.24. The current was injected on a large section and conducted by the nonwoven NCCF veil and the first layers of the laminate, without damaging too much the veil or the carbon fibre plies, as shown in Figure 4.24.a). This repartition of current contained the temperature elevation, and the pyrolysis of the resin in the structural plies was limited. More importantly, the pyrolysates could escape the laminate, building only small or no overpressure, as illustrated in Figure 4.24.b). The lower the sheet resistivity of the veil was, the more the current was conducted in the LSP layer, reducing the apparition of overpressure in the depth and the damage to the laminate. Hence, a small fibre breakage area was observed on NS0.5 and NS0.3 (c-3), no fibres were

broken on NS0.1 (c-2) and NS0.04 and the LSP was barely vaporised on NS0.04 (c-1). The damage observed and the mechanical properties retention are in agreement with the results reported by *Haynes et al.* [55] and *Guo et al.* [56].

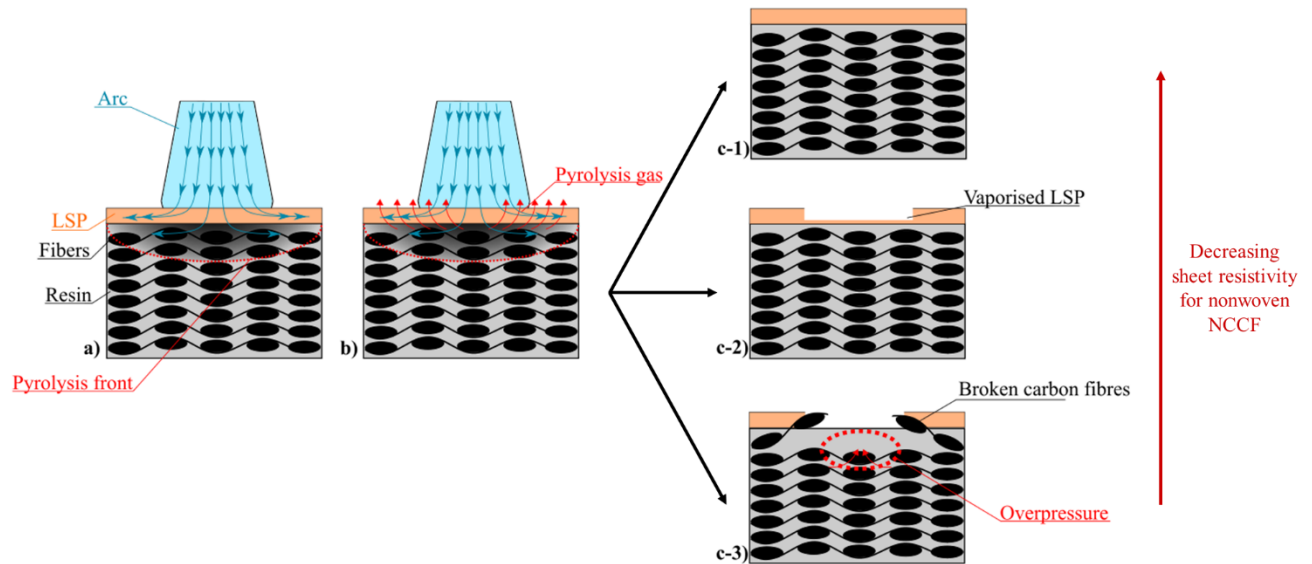


Figure 4.24: Damage mechanism of nonpainted panels and three damage types. a) The lightning current is injected on a large section and conducted by the LSP layer and the laminate. The lower the sheet resistivity of the nonwoven NCCF is, the more the current is conducted by the LSP. b) The pyrolysates from the pyrolyzed resin in the LSP layer or within the first plies are able to escape the panel creating small or no overpressure. c-1) 1st damage type: LSP barely vaporised: NS0.04. c-2) 2nd damage type: LSP vaporised: NS0.1 and ECF. c-3) 3rd damage type: Broken carbon fibres: NS0.5/0.3, CF and NC0.09.

Hence, the NS panels owed their LSP efficiency to a conductive network that dispersed a portion of the LS energy and absorbed the remaining energy while keeping a conductive network. The resin pyrolysis in the first plies caused some fibre breakage, delamination, and cracks, but was reduced for the panels with lower sheet resistivity.

CF panels behaved like NS, but without a LSP layer. Hence, the current was conducted deeper in the laminate and the first plies exploded, as shown in Figure 4.24.c-3).

4.6.3 PNS and PCF

The potential damage mechanism of PNS is illustrated in Figure 4.25. The lightning current penetrated the paint layer with dielectric breakdowns, as shown in Figure 4.25.a). The arc root radius was smaller than for the NS panels [12], [31], increasing the current density at the

attachment point. Despite its capacity to withstand high temperatures, the nonwoven NCCF veil most likely instantly vaporised near the attachment point. A more significant part of the current was injected deeper, in the structural plies, as illustrated in Figure 4.25.b). The resin pyrolyzed, but in deeper regions than without paint. This increased depth combined with the impermeable paint layer reduced the chance for the pyrolysis gas to escape the laminate, as shown in Figure 4.25.c). More overpressures were created, the first carbon fibre plies and the nonwoven layer burst, lifting the carbon fibres and ejecting paint flakes, as shown in Figure 4.25.d-2). The pyrolysis gas ignited in the contact with oxygen, maintaining a high temperature near the damaged area for 1-2 s, which might be enough to worsen the damage. The same behaviour was observed on PCF.

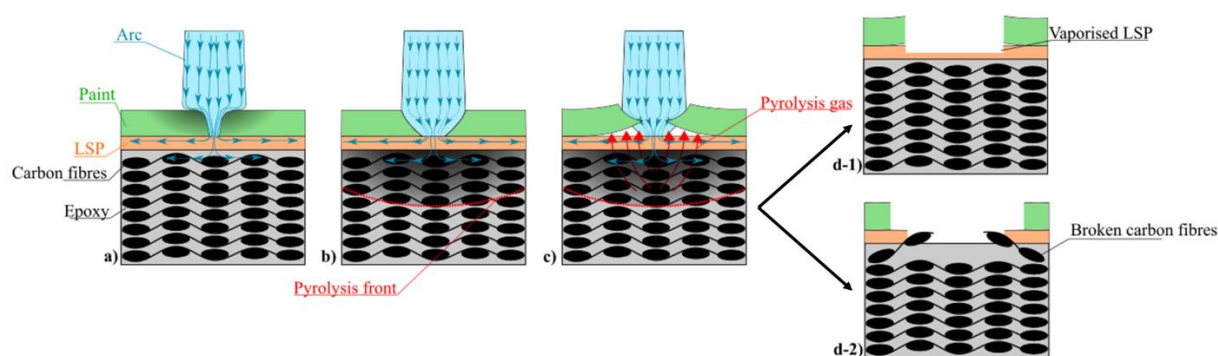


Figure 4.25: Damage mechanism of painted panels and two damage types. a) The lightning current penetrates through the paint via dielectric breakdowns. The paint around the point of attachment is evaporated. b) The lightning current is injected on a small section. The current density is higher than on NS panels, which increase the damage to the LSP layer. The current is conducted by a combination of the LSP and the laminate. c) The pyrolyses from the pyrolyzed resin in the LSP layer or within the first plies cannot escape the panel because of the impermeable paint layer creating overpressures that burst the first layers and the paint. d-1) 1st damage type: Vaporised LSP: PECEF. d-2) Broken carbon fibres: All other panels.

4.6.4 Different behaviour of the painted panels

The addition of a paint layer on the NS panels radically changed the damaged mechanism of the laminate, unlike for the ECF panels. We were not yet able to explain this phenomenon. However, we were able to make a few hypotheses:

- The electrical arc attachment behaviour might not be the same for PNS and PECEF. To answer this question, we observed the attachment of electrical arcs on the panel

surface at high voltage and low current, as presented in Appendix E. No important results for the discussion were obtained. The same observations at high current could lead to a better understanding of the lightning arc interaction with the composite surface.

- The sheet resistivity of the LSP layer might be an the most important parameter when the panel is painted. The LS energy has to be dispersed in the LSP layer and not deeper in the laminate to prevent the apparition of pyrolysis gas. In that case, the absence of electrical contact between the LSP layer and the baseline laminate might help increase the LSP efficiency, as the Joule effect would mostly take place in the LSP layer (see Appendix A 5.6.1.2).
- The architecture of the LSP layer might be a relevant parameter for painted panels, as it might need to provide exits for the resin pyrolysis gas, like the mesh pattern of the expanded copper foil. On the contrary, the nonwoven veil might be too impermeable. A grid pattern also provides higher local concentrations of electrical conductor, influencing the attachment of the electrical arc and the current conduction.
- The resistance to ablation of the LSP layer in the first instants of the LS might also be a key parameter. When the current density is at its highest value, the nonwoven veil most likely vaporises, allowing the current to propagate deeper. If the LSP withstand the first instant of the LS, it can conduct more LS energy and prevent the conduction in the deeper plies. But the opposite behaviour is also possible: the nonwoven veil does not vaporise as quickly as the ECF. Hence, it does not absorb enough energy from the lightning strike to prevent further damage.

4.6.5 NC

According to our observations, we could assume that the NC panels had a damage mechanism close to the one explained in Figure 4.24, with the 3rd damage type (c-3). The current was injected on a large section and was mostly conducted by the LSP layer. The temperature rose quicker than on NS panels, and the resin used for the wet lay-up pyrolyzed. On some panels, the overpressures were limited. On others, it burst the woven NCCF cloth. The mechanical properties retention are in agreement with the ones reported by *Mall et al.* [59]. Hence, despite a lower sheet resistivity than NS0.5 and NS0.3 and the highest stored energy of all LSP layers, the NC panels had a much lower LSP efficiency than any NS panels.

We could find two reasons to explain this lower efficiency. Firstly, the integration process of the NC panels led to the presence of an insulating resin layer between the LSP layer and the rest of the laminate, confirmed by the sheet resistivity measurements. Hence, the woven NCCF cloth conducted at first the current by itself. The resin rich layer, in contact with the NCCF cloth, pyrolyzed and overpressures could have been created. Secondly, the woven NCCF cloth was expected to act as a LSP layer and a structural ply, while the nonwoven NCCF veil acted only as a LSP layer. Hence, a damage to the nonwoven veil was acceptable if the baseline laminate was protected, but the woven cloth could not be damaged, as it still needed to act as a structural ply. Therefore, it is hard to conclude on the LSP efficiency of the woven NCCF cloth.

CHAPTER 5 CONCLUSION

5.1 Summary of the results

This work presented the study of the lightning strike protection efficiency of NCCF-based LSP without and with paint. Five materials were tested: a 295 g/m² NCCF Twill 2×2 cloth with 37.4 wt% of nickel and four nonwoven NCCF veils weighing 18 to 70 g/m². The woven cloth was integrated on a cured 7-ply laminate by manual wet lay-up with ~50 g/m² of resin, but was not painted.

The panels protected by the expanded copper foil had the same behaviour without and with paint: only the copper mesh was locally evaporated, leaving the baseline laminate intact. The mechanical properties retention was of 83% for the flexural strength and 94% for the effective bending stiffness.

The woven NCCF cloth did not protect the baseline laminate. Indeed, the same damage were observed on CF and NC panels with broken carbon fibres and a large delamination. Despite its lower sheet resistivity and higher stored energy, NC retained only 62% of its flexural strength while CF flexural strength retained by 58%. The woven NCCF was 54% more expensive than ECF but weighed only 147 g/m² as it replaced a 195 g/m² carbon fibre ply.

This work is the first to investigate the LSP efficiency of painted nonwoven NCCF veils on CFRP. The veils showed two very distinctive behaviours without and with paint, but in both cases the lower was the sheet resistivity of the panel, the higher its LSP efficiency. The integration method was problematic for large plates but worked on smaller ones. We observed no reduction of the mechanical properties before the LS test.

Without paint, the damage ranged from small fibre breakage and delamination (NS0.5 and NS0.3) to resin pyrolysis and small damage to the nonwoven with a checkerboard pattern (NS0.1 and NS0.04). NS0.04 showed the best mechanical properties retention with 97% for the flexural strength and 100% for the effective bending stiffness, while being 80% lighter than the ECF and 29% less expensive. With paint, the damage were more severe. The top second or third carbon fibre plies were damaged with important delamination and fibre breakage. The mechanical properties retention after the LS test were better than PCF but were at least 10% lower than PECF for all PNS.

In the end, the panels with the lowest sheet resistivity, NS0.1 and NS0.04, matched or exceeded the LSP efficiency of ECF without paint, while being at least 80% lighter and 29% less expensive. The integration process was validated on small plates but reserves were expressed concerning its viability for larger or non-planar assemblies. Indeed, the impregnation of the dry veil by the excess resin of the prepregs is more complex in that case. Unfortunately, the addition of paint drastically decreased the nonwoven NCCF performance, while the expanded copper foil maintained its high protection efficiency. The distinctive behaviour of the copper mesh is left to be fully understood in order to be reproduced with lighter materials.

5.2 Future work

Several new avenues will or could be explored in the framework of this project to keep on increasing the protection efficiency of the nonwoven NCCF-based LSP.

The first one is to stack two, or more, nonwoven veils on top of the laminate as they are much lighter than the expanded copper foil. The stacking would decrease the sheet resistivity of the laminate and increase the amount of material to vaporise.

Another avenue to be explored would be to reproduce the grid pattern of the expanded copper foil with the nonwoven NCCF veil. By doing a grid shape we could stack more veils, increase locally the density of electrical conductor and the permeability of the LSP layer, and hopefully increase the protection efficiency.

A numerical simulation of the lightning strike on protected CFRP panels could help understand the importance of the different parameters of the LSP layer for the LSP efficiency: thickness, sheet resistivity, thermal conductivity, heat capacity, architecture, etc.

To increase the scalability of this LSP solution nonwoven NCCF prepregs should be tested and their LSP efficiency evaluated. Finally, tests with standard waveforms should be undertaken to validate the results obtained with our in-house LS emulator.

5.3 Outcomes

Part of this work could be used for other applications than the lightning strike protection of composite materials. Indeed, the addition of a conductive layer on top of a CFRP panel can be required for EMI shielding or for the de-icing of aircraft or wind turbines by resistive heating.

The main outcome of this work is the experimental plan developed during this project to characterise the LSP layer and the lightning strike damage. Indeed, it could be applied to investigate any LSP solutions. The combination of diagnostics before, during and after the lightning strike bring enough information to compare the different solutions, understand the difference in their behaviour and evaluate their LSP efficiency. Our team is already investigating other nonwoven NCCF-based LSP, as well as silver coated milled carbon fibres dispersed in paint. A lighter alternative to the expanded copper foil, matching its LSP efficiency on painted panels, would certainly be certified and used on most commercial aircraft. A reduction of 100 g/m² in the LSP layer would reduce the weight of a Boeing 787 by at least 250 kg. This would slightly increase the fuel efficiency of commercial aircraft and help the aviation sector reach its carbon neutral trajectory.

REFERENCES

- [1] ICAO, 'Historic agreement reached to mitigate international aviation emissions - CORSIA', *ICAO*, Oct. 03, 2016. <https://www.icao.int/Newsroom/Pages/Historic-agreement-reached-to-mitigate-international-aviation-emissions.aspx> (accessed Apr. 08, 2022).
- [2] 'Our Commitment to Fly Net Zero by 2050', *International Air Transport Association*. <https://www.iata.org/en/programs/environment/flynetzero/> (accessed Apr. 07, 2022).
- [3] M. A. Uman and V. A. Rakov, 'The interaction of lightning with airborne vehicles', *Prog. Aerosp. Sci.*, vol. 39, no. 1, pp. 61–81, Jan. 2003, doi: 10.1016/S0376-0421(02)00051-9.
- [4] V. Maur and V. I. Mazur, *Principles of lightning physics*. Bristol, UK: IOP Publishing, 2016.
- [5] I. Gallimberti, G. Bacchiega, A. Bondiou-Clergerie, and P. Lalande, 'Fundamental processes in long air gap discharges', *Comptes Rendus Phys.*, vol. 3, no. 10, pp. 1335–1359, Dec. 2002, doi: 10.1016/S1631-0705(02)01414-7.
- [6] E. Rupke, 'Lightning Direct Effects Handbook', p. 119.
- [7] Aircraft Lightning Environment and Related Test Waveforms. SAE Aerospace ARP 5412B. 2013
- [8] A. Nag and V. A. Rakov, 'Compact intracloud lightning discharges: 2. Estimation of electrical parameters', *J. Geophys. Res.*, vol. 115, no. D20, p. D20103, Oct. 2010, doi: 10.1029/2010JD014237.
- [9] J.-P. Moreau, J.-C. Alliot, and V. Mazur, 'Aircraft lightning initiation and interception from in situ electric measurements and fast video observations', *J. Geophys. Res.*, vol. 97, no. D14, p. 15903, 1992, doi: 10.1029/92JD01077.
- [10] P. Lalande, A. Bondiou-Clergerie, and P. Laroche, 'Analysis of Available In-Flight Measurements of Lightning Strikes to Aircraft', Jun. 1999, pp. 1999-01–2397. doi: 10.4271/1999-01-2397.
- [9] Aircraft Lightning Zoning. SAE Aerospace ARP 5414A. 2005
- [12] L. Chemartin *et al.*, 'Direct Effects of Lightning on Aircraft Structure: Analysis of the Thermal, Electrical and Mechanical Constraints', no. 5, p. 15, 2012.
- [13] 'Boeing 787 specifications', *Boeing*. <https://www.boeing.com/commercial/787/> (accessed Jan. 22, 2022).
- [14] P. Lalande and A. Delannoy, 'Numerical Methods for Zoning Computation', no. 5, p. 11, 2012.
- [15] N/A, 'Table A10. Properties of Metals Used in Cables and Conductors', [Online]. Available: <https://app.knovel.com/hotlink/itble/rcid:kpIPSDEG02/id:kt011JFGHA/industrial-power-systems/table-a10-properties>
- [16] C. Han, B. Sun, and B. Gu, 'Electric potential distributions in carbon fiber/epoxy plain-woven laminates with different current directions', *Compos. Struct.*, vol. 270, p. 114059, Aug. 2021, doi: 10.1016/j.compstruct.2021.114059.

- [17] V. Kumar *et al.*, 'Polyaniline-based all-polymeric adhesive layer: An effective lightning strike protection technology for high residual mechanical strength of CFRPs', *Compos. Sci. Technol.*, vol. 172, pp. 49–57, Mar. 2019, doi: 10.1016/j.compscitech.2019.01.006.
- [18] V. Kumar *et al.*, 'Effect of through-thickness electrical conductivity of CFRPs on lightning strike damages', *Compos. Part Appl. Sci. Manuf.*, vol. 114, pp. 429–438, Nov. 2018, doi: 10.1016/j.compositesa.2018.09.007.
- [19] V. Kumar *et al.*, 'Interleaved MWCNT buckypaper between CFRP laminates to improve through-thickness electrical conductivity and reducing lightning strike damage', *Compos. Struct.*, vol. 210, pp. 581–589, Feb. 2019, doi: 10.1016/j.compstruct.2018.11.088.
- [20] S. Bard, F. Schönl, M. Demleitner, and V. Altstädt, 'Copper and Nickel Coating of Carbon Fiber for Thermally and Electrically Conductive Fiber Reinforced Composites', *Polymers*, vol. 11, no. 5, p. 823, May 2019, doi: 10.3390/polym11050823.
- [21] Aircraft Lightning Test Methods. SAE Aerospace ARP 5416A. 2013
- [22] R. Muñoz, S. Delgado, C. González, B. López-Romano, D.-Y. Wang, and J. LLorca, 'Modeling Lightning Impact Thermo-Mechanical Damage on Composite Materials', *Appl. Compos. Mater.*, vol. 21, no. 1, pp. 149–164, Feb. 2014, doi: 10.1007/s10443-013-9377-9.
- [23] S. L. J. Millen and A. Murphy, 'Modelling and analysis of simulated lightning strike tests: A review', *Compos. Struct.*, vol. 274, p. 114347, Oct. 2021, doi: 10.1016/j.compstruct.2021.114347.
- [24] B. A. Newcomb and H. G. Chae, '21 - The properties of carbon fibers', in *Handbook of Properties of Textile and Technical Fibres (Second Edition)*, A. R. Bunsell, Ed. Woodhead Publishing, 2018, pp. 841–871. doi: 10.1016/B978-0-08-101272-7.00021-3.
- [25] J. Langot, 'Multi-physics modeling of aerospace composites exposed to fire'.
- [26] Y. Hirano, S. Katsumata, Y. Iwahori, and A. Todoroki, 'Artificial lightning testing on graphite/epoxy composite laminate', *Compos. Part Appl. Sci. Manuf.*, vol. 41, no. 10, pp. 1461–1470, Oct. 2010, doi: 10.1016/j.compositesa.2010.06.008.
- [27] J. Sun, X. Yao, X. Tian, J. Chen, and Y. Wu, 'Damage Characteristics of CFRP Laminates Subjected to Multiple Lightning Current Strike', *Appl. Compos. Mater.*, vol. 26, no. 3, pp. 745–762, Jun. 2019, doi: 10.1007/s10443-018-9747-4.
- [28] A. Bigand, C. Espinosa, and J. M. Bauchire, 'Equivalent mechanical load model methodology to simulate lightning strike impact on protected and painted composite structure', *Compos. Struct.*, vol. 280, p. 114886, Jan. 2022, doi: 10.1016/j.compstruct.2021.114886.
- [29] H. Kawakami and P. Feraboli, 'Lightning strike damage resistance and tolerance of scarf-repaired mesh-protected carbon fiber composites', *Compos. Part Appl. Sci. Manuf.*, vol. 42, no. 9, pp. 1247–1262, Sep. 2011, doi: 10.1016/j.compositesa.2011.05.007.
- [30] F. Moupfouma, 'Aircraft Structure Paint Thickness and Lightning Swept Stroke Damages', *SAE Int. J. Aerosp.*, vol. 6, no. 2, pp. 392–398, Sep. 2013, doi: 10.4271/2013-01-2135.
- [31] R. S. Martins, 'Experimental and theoretical studies of lightning arcs and their interaction with aeronautical materials'.

- [32] M. Gagné and D. Therriault, 'Lightning strike protection of composites', *Prog. Aerosp. Sci.*, vol. 64, pp. 1–16, Jan. 2014, doi: 10.1016/j.paerosci.2013.07.002.
- [33] '3M™ Scotch-Weld™ Composite Surfacing and Lightning Protection Film AF 536', 3M. https://www.3m.co.uk/3M/en_GB/aerospace-emea/af536/ (accessed Jan. 19, 2022).
- [34] B. Zhang, V. R. Patlolla, D. Chiao, D. K. Kalla, H. Misak, and R. Asmatulu, 'Galvanic corrosion of Al/Cu meshes with carbon fibers and graphene and ITO-based nanocomposite coatings as alternative approaches for lightning strikes', *Int. J. Adv. Manuf. Technol.*, vol. 67, no. 5–8, pp. 1317–1323, Jul. 2013, doi: 10.1007/s00170-012-4568-3.
- [35] Y. Guo, Y. Xu, Q. Wang, Q. Dong, X. Yi, and Y. Jia, 'Enhanced lightning strike protection of carbon fiber composites using expanded foils with anisotropic electrical conductivity', *Compos. Part Appl. Sci. Manuf.*, vol. 117, pp. 211–218, Feb. 2019, doi: 10.1016/j.compositesa.2018.11.022.
- [36] V. Kumar *et al.*, 'Factors affecting direct lightning strike damage to fiber reinforced composites: A review', *Compos. Part B Eng.*, vol. 183, p. 107688, Feb. 2020, doi: 10.1016/j.compositesb.2019.107688.
- [37] C. Karch and C. Metzner, 'Lightning protection of carbon fibre reinforced plastics — An overview', in *2016 33rd International Conference on Lightning Protection (ICLP)*, Estoril, Sep. 2016, pp. 1–8. doi: 10.1109/ICLP.2016.7791441.
- [38] Y. Wang, 'Multiphysics analysis of lightning strike damage in laminated carbon/glass fiber reinforced polymer matrix composite materials: A review of problem formulation and computational modeling', *Compos. Part Appl. Sci. Manuf.*, vol. 101, pp. 543–553, Oct. 2017, doi: 10.1016/j.compositesa.2017.07.010.
- [39] P. S. M. Rajesh, F. Sirois, and D. Therriault, 'Damage response of composites coated with conducting materials subjected to emulated lightning strikes', *Mater. Des.*, vol. 139, pp. 45–55, Feb. 2018, doi: 10.1016/j.matdes.2017.10.017.
- [40] S. de Juan, E. Gordo, A. Jiménez-Morales, and F. Sirois, 'Response of electroless copper coated CFRP laminates to emulated lightning strikes', *Compos. Part Appl. Sci. Manuf.*, vol. 140, p. 106184, Jan. 2021, doi: 10.1016/j.compositesa.2020.106184.
- [41] F. S. Wang, Y. Y. Ji, X. S. Yu, H. Chen, and Z. F. Yue, 'Ablation damage assessment of aircraft carbon fiber/epoxy composite and its protection structures suffered from lightning strike', *Compos. Struct.*, vol. 145, pp. 226–241, Jun. 2016, doi: 10.1016/j.compstruct.2016.03.005.
- [42] F. Wang, X. Ma, Y. Zhang, and S. Jia, 'Lightning Damage Testing of Aircraft Composite-Reinforced Panels and Its Metal Protection Structures', *Appl. Sci.*, vol. 8, no. 10, p. 1791, Oct. 2018, doi: 10.3390/app8101791.
- [43] Z. J. Zhao *et al.*, 'Development of electrically conductive structural BMI based CFRPs for lightning strike protection', *Compos. Sci. Technol.*, vol. 167, pp. 555–562, Oct. 2018, doi: 10.1016/j.compscitech.2018.08.026.
- [44] H. Che *et al.*, 'Metallization of Carbon Fiber Reinforced Polymers for Lightning Strike Protection', *J. Mater. Eng. Perform.*, vol. 27, no. 10, pp. 5205–5211, Oct. 2018, doi: 10.1007/s11665-018-3609-y.

- [45] B. Zhang, S. A. Soltani, L. N. Le, and R. Asmatulu, 'Fabrication and assessment of a thin flexible surface coating made of pristine graphene for lightning strike protection', *Mater. Sci. Eng. B*, vol. 216, pp. 31–40, Feb. 2017, doi: 10.1016/j.mseb.2017.02.008.
- [46] B. Wang, Y. Duan, Z. Xin, X. Yao, D. Abliz, and G. Ziegmann, 'Fabrication of an enriched graphene surface protection of carbon fiber/epoxy composites for lightning strike via a percolating-assisted resin film infusion method', *Compos. Sci. Technol.*, vol. 158, pp. 51–60, Apr. 2018, doi: 10.1016/j.compscitech.2018.01.047.
- [47] H. Chu, Q. Xia, Z. Zhang, Y. Liu, and J. Leng, 'Sesame-cookie topography silver nanoparticles modified carbon nanotube paper for enhancing lightning strike protection', *Carbon*, vol. 143, pp. 204–214, Mar. 2019, doi: 10.1016/j.carbon.2018.11.022.
- [48] Q. Xia, H. Mei, Z. Zhang, Y. Liu, Y. Liu, and J. Leng, 'Fabrication of the silver modified carbon nanotube film/carbon fiber reinforced polymer composite for the lightning strike protection application', *Compos. Part B Eng.*, vol. 180, p. 107563, Jan. 2020, doi: 10.1016/j.compositesb.2019.107563.
- [49] K. Dydek *et al.*, 'Effect of SWCNT-Tuball Paper on the Lightning Strike Protection of CFRPs and Their Selected Mechanical Properties', *Materials*, vol. 14, no. 11, p. 3140, Jun. 2021, doi: 10.3390/ma14113140.
- [50] J. Han *et al.*, 'The combination of carbon nanotube buckypaper and insulating adhesive for lightning strike protection of the carbon fiber/epoxy laminates', *Carbon*, vol. 94, pp. 101–113, Nov. 2015, doi: 10.1016/j.carbon.2015.06.026.
- [51] H. Zhu, K. Fu, B. Yang, and Y. Li, 'Nickel-coated nylon sandwich film for combination of lightning strike protection and electromagnetic interference shielding of CFRP composite', *Compos. Sci. Technol.*, vol. 207, p. 108675, May 2021, doi: 10.1016/j.compscitech.2021.108675.
- [52] Y. Li, T. Xue, R. Li, X. Huang, and L. Zeng, 'Influence of a fiberglass layer on the lightning strike damage response of CFRP laminates in the dry and hygrothermal environments', *Compos. Struct.*, vol. 187, pp. 179–189, Mar. 2018, doi: 10.1016/j.compstruct.2017.12.057.
- [53] D. K. Chakravarthi *et al.*, 'Carbon Fiber-Bismaleimide Composites Filled with Nickel-Coated Single-Walled Carbon Nanotubes for Lightning-Strike Protection', *Adv. Funct. Mater.*, vol. 21, no. 13, pp. 2527–2533, Jul. 2011, doi: 10.1002/adfm.201002442.
- [54] X. Cauchy, J.-E. Klemberg-Sapieha, and D. Therriault, 'Hybrid Carbon-Silver Nanofillers for Composite Coatings with Near Metallic Electrical Conductivity', *Adv. Eng. Mater.*, vol. 20, no. 12, p. 1800541, Dec. 2018, doi: 10.1002/adem.201800541.
- [55] K. K. Haynes, V. Company, and A. Mazas, 'NONWOVEN VEIL TECHNOLOGY FOR LIGHTNING STRIKE PROTECTION', p. 8.
- [56] Y. Guo, Y. Xu, Q. Wang, Q. Dong, X. Yi, and Y. Jia, 'Eliminating lightning strike damage to carbon fiber composite structures in Zone 2 of aircraft by Ni-coated carbon fiber nonwoven veils', *Compos. Sci. Technol.*, vol. 169, pp. 95–102, Jan. 2019, doi: 10.1016/j.compscitech.2018.11.011.
- [57] J. Zhang, X. Zhang, X. Cheng, Y. Hei, L. Xing, and Z. Li, 'Lightning strike damage on the composite laminates with carbon nanotube films: Protection effect and damage mechanism', *Compos. Part B Eng.*, vol. 168, pp. 342–352, Jul. 2019, doi: 10.1016/j.compositesb.2019.03.054.

- [58] A. Henn et R. Schmitt. « Nickel-Plated Carbon Fabric for Aircraft Composites », *Advanced Materials: Performance Through Technology Insertion.*, vol. 38, p. 1876–1881, 1993.
- [59] S. Mall, B. L. Ouper, and J. C. Fielding, ‘Compression Strength Degradation of Nanocomposites after Lightning Strike’, *J. Compos. Mater.*, vol. 43, no. 24, pp. 2987–3001, Nov. 2009, doi: 10.1177/0021998309345337.
- [60] Y. Ming *et al.*, ‘3D printed nickel-plated carbon fiber mesh for lightning strike protection’, *Mater. Lett.*, vol. 294, p. 129809, Jul. 2021, doi: 10.1016/j.matlet.2021.129809.
- [61] Z. Zhao *et al.*, ‘Light weight non-metallic lightning strike protection film for CFRP’, *Mater. Today Commun.*, vol. 25, p. 101502, Dec. 2020, doi: 10.1016/j.mtcomm.2020.101502.
- [62] J. Gou, Y. Tang, F. Liang, Z. Zhao, D. Firsich, and J. Fielding, ‘Carbon nanofiber paper for lightning strike protection of composite materials’, *Compos. Part B Eng.*, vol. 41, no. 2, pp. 192–198, Mar. 2010, doi: 10.1016/j.compositesb.2009.06.009.
- [63] Y. Guo *et al.*, ‘Implementation of fiberglass in carbon fiber composites as an isolation layer that enhances lightning strike protection’, *Compos. Sci. Technol.*, vol. 174, pp. 117–124, Apr. 2019, doi: 10.1016/j.compscitech.2019.02.023.
- [64] Y. Hirano *et al.*, ‘Lightning damage suppression in a carbon fiber-reinforced polymer with a polyaniline-based conductive thermoset matrix’, *Compos. Sci. Technol.*, vol. 127, pp. 1–7, Apr. 2016, doi: 10.1016/j.compscitech.2016.02.022.
- [65] A. Katunin, K. Krukiewicz, R. Turczyn, P. Sul, A. Łasica, and M. Bilewicz, ‘Synthesis and characterization of the electrically conductive polymeric composite for lightning strike protection of aircraft structures’, *Compos. Struct.*, vol. 159, pp. 773–783, Jan. 2017, doi: 10.1016/j.compstruct.2016.10.028.
- [66] A. Katunin, K. Krukiewicz, R. Turczyn, P. Sul, and K. Dragan, ‘Lightning strike resistance of an electrically conductive CFRP with a CSA-doped PANI/epoxy matrix’, *Compos. Struct.*, vol. 181, pp. 203–213, Dec. 2017, doi: 10.1016/j.compstruct.2017.08.091.
- [67] S. Manomaisantiphap, V. Kumar, T. Okada, and T. Yokozeki, ‘Electrically conductive carbon fiber layers as lightning strike protection for non-conductive epoxy-based CFRP substrate’, *J. Compos. Mater.*, vol. 54, no. 29, pp. 4547–4555, Dec. 2020, doi: 10.1177/0021998320935946.
- [68] S. Kamiyama, Y. Hirano, T. Okada, and T. Ogasawara, ‘Lightning strike damage behavior of carbon fiber reinforced epoxy, bismaleimide, and polyetheretherketone composites’, *Compos. Sci. Technol.*, vol. 161, pp. 107–114, Jun. 2018, doi: 10.1016/j.compscitech.2018.04.009.
- [69] S. Yamashita, Y. Hirano, T. Sonehara, J. Takahashi, K. Kawabe, and T. Murakami, ‘Residual mechanical properties of carbon fibre reinforced thermoplastics with thin-ply prepreg after simulated lightning strike’, *Compos. Part Appl. Sci. Manuf.*, vol. 101, pp. 185–194, Oct. 2017, doi: 10.1016/j.compositesa.2017.06.002.
- [70] E. Logakis and A. A. Skordos, ‘LIGHTNING STRIKE PERFORMANCE OF CARBON NANOTUBE LOADED AEROSPACE COMPOSITES’, p. 6, 2012.

- [71] S. Yamashita, T. Sonehara, J. Takahashi, K. Kawabe, and T. Murakami, 'Effect of thin-ply on damage behaviour of continuous and discontinuous carbon fibre reinforced thermoplastics subjected to simulated lightning strike', *Compos. Part Appl. Sci. Manuf.*, vol. 95, pp. 132–140, Apr. 2017, doi: 10.1016/j.compositesa.2017.01.010.
- [72] J. Zhang, X. Zhang, X. Cheng, Y. Hei, L. Xing, and Z. Li, 'Lightning strike damage on the composite laminates with carbon nanotube films: Protection effect and damage mechanism', *Compos. Part B Eng.*, vol. 168, pp. 342–352, Jul. 2019, doi: 10.1016/j.compositesb.2019.03.054.
- [73] Q. Dong *et al.*, 'Lightning Damage of Carbon Fiber/Epoxy Laminates with Interlayers Modified by Nickel-Coated Multi-Walled Carbon Nanotubes', *Appl. Compos. Mater.*, vol. 24, no. 6, pp. 1339–1351, Dec. 2017, doi: 10.1007/s10443-017-9589-5.
- [74] D. M. Lombetti and A. A. Skordos, 'Lightning strike and delamination performance of metal tufted carbon composites', *Compos. Struct.*, vol. 209, pp. 694–699, Feb. 2019, doi: 10.1016/j.compstruct.2018.11.005.
- [75] J. Rehbein, P. Wierach, T. Gries, and M. Wiedemann, 'Improved electrical conductivity of NCF-reinforced CFRP for higher damage resistance to lightning strike', *Compos. Part Appl. Sci. Manuf.*, vol. 100, pp. 352–360, Sep. 2017, doi: 10.1016/j.compositesa.2017.05.014.
- [76] 'Galvanic series chart', *Australian Stainless Steel Development Association (ASSDA)*, Jan. 25, 2020. <https://www.assda.asn.au/technical-info/technical-faqs/galvanicdissimilar-metal-corrosion>
- [77] A. Katunin, K. Krukiewicz, R. Turczyn, P. Sul, and M. Bilewicz, 'Electrically conductive carbon fibre-reinforced composite for aircraft lightning strike protection', *IOP Conf. Ser. Mater. Sci. Eng.*, vol. 201, p. 012008, May 2017, doi: 10.1088/1757-899X/201/1/012008.
- [78] 'NiCVD coated fibers - Conductive Composites', *Conductive Composites*. <https://www.conductivecomposites.com/AdvancedMaterials/Fibers> (accessed Feb. 10, 2020).
- [79] 'Nonwoven for electrical conductivity - Technical Fibre Products', *TFP Global*. <https://www.tfpglobal.com/products/composite-materials/electrical-conductivity> (accessed Feb. 10, 2022).
- [80] 'VeeloVeil - VeeloTech', *VeeloTech*. <https://www.veelotech.com/veelo-veil> (accessed Feb. 10, 2022).
- [81] F. M. Smits, 'Measurement of Sheet Resistivities with the Four-Point Probe', *Bell Syst. Tech. J.*, vol. 37, no. 3, pp. 711–718, May 1958, doi: <https://doi.org/10.1002/j.1538-7305.1958.tb03883.x>.
- [82] J. Janesch, 'Two-Wire vs. Four-Wire Resistance Measurements: Which Configuration Makes Sense for Your Application?', *Keithley Instrum.*, p. 3.
- [83] P. S. M. Rajesh, 'RESPONSE OF COMPOSITE PANELS WITH CONDUCTIVE COATINGS SUBMITTED TO EMULATED LIGHTNING STRIKES'.
- [84] D20 Committee, 'Test Method for Flexural Properties of Unreinforced and Reinforced Plastics and Electrical Insulating Materials by Four-Point Bending', ASTM International. doi: 10.1520/D6272-17E01.

- [85] G. Glockler, 'The Heat of Sublimation of Graphite and the Composition of Carbon Vapor', *J. Chem. Phys.*, vol. 22, no. 2, pp. 159–161, Feb. 1954, doi: 10.1063/1.1740023.
- [86] Z. Liu, P. Li, and N. Srikanth, 'Effect of delamination on the flexural response of [+45/−45/0]_{2s} carbon fibre reinforced polymer laminates', *Compos. Struct.*, vol. 209, pp. 93–102, Feb. 2019, doi: 10.1016/j.compstruct.2018.10.049.
- [87] F. A. Fisher and J. A. Plumer, 'Lightning Protection of Aircraft', p. 570.
- [88] Y. Murooka, 'A SURVEY OF LIGHTNING INTERACTION WITH AIRCRAFT IN JAPAN', *J. Atmospheric Electr.*, vol. 12, no. 1, pp. 101–106, 1992, doi: 10.1541/jae.12.101.
- [89] P. Lalande, A. Bondiou-Clergerie, and P. Laroche, 'Computations of the Initial Discharge Initiation Zones on Aircraft or Helicopter', Jun. 1999, pp. 1999-01–2371. doi: 10.4271/1999-01-2371.
- [90] A. Broc *et al.*, 'A lightning swept stroke model: A valuable tool to investigate the lightning strike to aircraft', *Aerosp. Sci. Technol.*, vol. 10, no. 8, pp. 700–708, Dec. 2006, doi: 10.1016/j.ast.2005.10.008.
- [91] S. Yamashita, Y. Hirano, T. Sonehara, J. Takahashi, K. Kawabe, and T. Murakami, 'Residual mechanical properties of carbon fibre reinforced thermoplastics with thin-ply prepreg after simulated lightning strike', *Compos. Part Appl. Sci. Manuf.*, vol. 101, pp. 185–194, Oct. 2017, doi: 10.1016/j.compositesa.2017.06.002.
- [92] Y. Hirano, T. Sonehara, J. Takahashi, K. Kawabe, T. Murakami, and Shinichiro Yamashita, 'Residual mechanical properties of carbon fibre reinforced thermoplastics with thin-ply prepreg after simulated lightning strike', *Compos. Part Appl. Sci. Manuf.*, vol. 101, pp. 185–194, Oct. 2017, doi: 10.1016/j.compositesa.2017.06.002.

APPENDIX A EXHAUSTIVE LITTERATURE REVIEW

5.4 Statistics on lightning strikes to aircraft

Several studies on lightning-aircraft interaction were conducted between the 1950s and 1990s to understand the condition that favours lightning strikes to aircraft [87], [88]. The altitude, the temperature and the meteorological conditions were reported for each strike endured by the aircraft.

According to *Fisher and Plumer* [87], and as shown in Figure 0.1, the vast majority of the strikes happened below 7 km at temperatures between -5°C and 0°C . The cruise altitude of turboprop and turbojet aircraft are between 8 and 10 km, but almost no strikes were recorded at these altitudes, as can be seen on the four studies on the left. When we compare the strike altitude to the typical charge distribution in a thundercloud, we understand that strikes occurring below 3 km are most likely cloud-to-ground flashes, whereas those occurring above 3 km are intra- or intercloud flashes. Since most helicopters fly at altitudes lower than 7 km, they are always subjected to a lightning hazard.

For more than 80% of the cases, the discharge took place when the aircraft was inside the cloud. It seems that the flight conditions had almost no impact on the probability of strike: around 70% of them happened during climbing or descending phase whereas 30% of them happened during the hold phase and just a few on the ground.

Therefore, for modern jet planes we can consider that most of the strikes happen during climbing or ascending but not during the cruise phase. Finally, *Uman and Rakov* [3] estimated that a commercial plane was struck every 3,000 hours of flight. That is around one time per year per commercial aircraft.

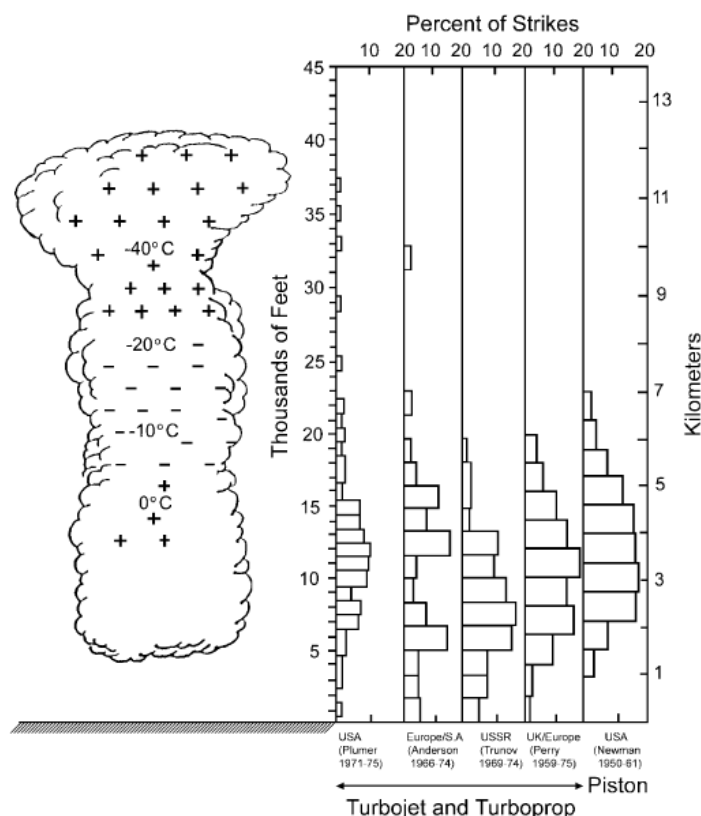


Figure 0.1: Data from five studies summarised by *Fisher and Plumer* [87] and adapted by *Uman and Rakov* [3]. On the left, the typical electric charge distribution in a thundercloud is represented. On the right, the strike altitude distribution of five studies conducted between 1950 and 1975 is displayed.

5.5 Details on aircraft zoning

As mentioned previously, the different parts of an aircraft structure will not be exposed to the same conditions. Indeed, the sharp ends have a higher probability of being the first point of attachment than the top of the wings or the fuselage [14], [89]. However, the latter two areas will have a greater chance to house re-attachment points due to the sweeping effect [14], [90]. In the framework of the European FULMEN program, models developed by ONERA and the University of Padova were used to determine the location of the initial entry and exit points of a lightning strike on a given aircraft [89]. For a given ambient field direction, the entry and exit points are spots where a leader can have a stable propagation and where the electric field is higher than the critical electric field. As expected, the pointier the structure edge is, the higher is the probability of initial attachment.

A complete model for the zoning of aircraft was published by *Lalande and Delannoy* [14], combining the model of attachment with a model of the sweeping effect. They were able to determine, for a given aircraft and electric field direction, the location of the initial attachment points and the sweeping path on the aircraft structure. They combined this model with a probabilistic distribution of the time of arrival of the subsequent strokes to get the probability of location of each stroke on the aircraft structure.

5.6 Lightning strike protection review

5.6.1 On top of the laminate

The LSP located on the top of the CFRP are meant to prevent the lightning current to penetrate. The first and most investigated type is a conductive layer that will be damaged during the lightning strike, sacrificing itself to protect the CFRP. The second type has an insulating layer incorporated between the sacrificial conductive layer and the CFRP.

5.6.1.1 Sacrificial conductive layer

a) Metallic

Mesh

Details in Section 2.3.1.1.

Nanoparticles

Metal nanoparticles can be used to make the finishes conductive. *Rajesh et al.* [39] studied the LSP efficiency of several silver-based solutions. For one of them, they dispersed silver nanoparticles in poly(3,4-ethylenedioxythiophene) polystyrene sulfonate (PEDOT:PSS). The mixture was then sprayed onto the surface of the laminate. However, the damage reported for this material was equivalent to that of CFRP with a damage area of 2142 mm² and depth of 0.94 mm.

Continuous layer – Electroless deposition

Other research groups have sought to coat the laminate with a continuous metallic layer by either electroless deposition or spray coating.

Rajesh et al. [39] investigated the electroless deposition of silver on the CFRP. They deposited a 5 μm thick layer, but this solution did not show a very good LSP capacity at 40 kA. A damage depth of 0.75 mm was reported, which is only 0.08 mm less than for an unprotected CFRP. *de Juan et al.* [40] focused on the electroless deposition of copper. The 0.602 and 1.148 μm thick coatings provided a reduction in the damage area by a factor of, respectively, 2.5 and 2.7 compared to the unprotected CFRP after a 40 kA test. By linear approximation, a coating of 7.07 μm and 63 g/m^2 would be required to achieve no damage, although being 64% lighter than a standard 195 g/m^2 ECF.

Both silver and copper deposit had a sheet resistivity of 0.3 Ω/sq , but the first one had a lesser LSP efficiency.

Continuous layer – Spray

Zhao et al. [43] coated their CFRP with a 250 g/m^2 aluminium spray. The damage reported after a DBC test were small: 0.41 mm in depth and 844 mm^2 in area with 90% retention of compressive strength.

Two cold metal sprays have been considered by *Rajesh et al.* and *Che et al.* [39], [44] as LSP. Tin and copper-tin powders (10 wt% Cu) were sprayed on the surface of CFRP. Both solutions were undamaged by exposure to a waveform C. The copper-tin solution was also exposed to a 40 kA lightning strike, and no damage in the depth was reported (compared to 0.83 mm for the pristine CFRP). However, the estimated areal density for these solutions is 1733.25 and 2850 g/m^2 , respectively. *Wang et al.* [41], [42] studied a 0.1 or 0.2 mm thick aluminium spray, covering totally or locally the laminate. After tests with a waveform D, damage covering 23% of the laminate surface were reported for the 0.2 mm spray covering the totality of the laminate, while an ECF reduced the damage area to 14.75%. The same damage depth is reported for all the solutions tested, but no mechanical analysis can conclude on the actual LSP efficiency.

b) Non-metallic

Graphene

Details in Section 2.3.1.1.

Carbon nanotubes

A 60 μm thick, 40 g/m^2 SWCnT paper was manufactured by *Chu et al.* [47]. Its electrical conductivity of 3.23 S/m allowed it to retain 75.6% of the ultimate load after a Zone 2A (DBC) lightning test, whereas the pristine CFRP retained only 65.9%. *Xia et al.* [48] tested the same material at 100kA. The compression tests indicated a retention of 80.35% of the ultimate strength for the SWCnT paper, while unprotected CFRP retained only 60.45%. In these two papers, solutions incorporating silver particles into the CnT paper by two different methods were also studied (see Section 2.3.1.1.c).

More recently, *Dydek et al.* [49] studied SWCnT in the form of two bucky papers: TP1 (90 wt% SWCnT, 27.4 μm thick and 41.5 g/m^2) and TP2 (75 wt% SWCnT, 51.5 μm thick and 45 g/m^2). The addition of TP1 paper to the surface of a CFRP increased its resistance to impacts. However, TP2 had a very small influence on these properties. This increase did not limit the damage after a DBC lightning test. Indeed, the damage area was 2,475 mm^2 for TP1, while the unprotected CFRP showed damage area over 5,950 mm^2 and an ECF limited it to 1,440 mm^2 .

Han et al. [50] used MWCnT to make a 70 μm thick paper with a conductivity of 5.7×10^3 S/m. They glued this paper to a CFRP using three epoxy-based adhesives of various conductivities. In this section, we look at the most conductive one. The epoxy was mixed with 1 wt% MWCnT and its conductivity increased by 7 orders of magnitude to 0.4 S/m, but its dielectric strength in oil was reduced by a factor of 48 to 2.1 kV/mm. A laminate protected by a 500 μm thick MWCnT paper sheet and conductive adhesive was struck by a 40 kA current. The damage reported are similar to that of the unprotected CFRP, with a damage depth of 0.8 mm (compared to 0.9 mm) and a 10% higher compressive strength retention. *Kumar et al.* [19] stuck a 150 μm thick MWCnT paper to a CFRP without adhesive. Only a delamination between the first two plies over a diameter of 10 mm (compared to 30 mm for pristine CFRP) was reported. The post 40 kA lightning mechanical properties of protected and unprotected CFRP were similar.

Zhu et al. [51] used a commercially available 60 μm thick and 30 g/m^2 BP sheet as a LSP. After testing at 100 kA, the damage to the laminate were quite severe, with a damage area of 2,889.07 mm^2 and a depth of 0.82 mm allowing 81.05% of the compressive strength to be maintained. At the same time, the ECF maintained 92.62% for much lesser damage: 194.52 mm^2 and 0.3 mm.

Conductive adhesive

Details in Section 2.3.1.1.

Glass fibres layers

Li et al. [52] studied the addition of two glass fibre plies on top of the laminate to limit lightning damage and water penetration into the composite. After testing at 32 kA, they found that the two plies increased the damage depth already observed on the CFRP from 0.82 mm to 1.37 mm. The GFRP layer, which is relatively insulating compared to the carbon fibres, has the same effect as a layer of paint by trapping the gases from the pyrolysis of the resin, creating more overpressure and bigger damage than without it.

Despite their relatively high electrical conductivity, SW and MW CnT papers alone were not yet able to significantly protect the CFRP from lightning damage. RGO provided good results with a small added mass. Conductive PANI adhesive had a great LSP efficiency on a painted CFRP panel, with no improvement in the added mass in comparison with standard ECF. The PANI adhesive is, so far, the only published alternative to ECF for painted panels.

c) Hybrid

Carbon materials are not able to protect the laminate alone, but their high specific electrical conductivity encourages their use combined with that of metals. Carbonous papers can be enriched with metallic nanoparticles. Carbon nanomaterials or carbon fibres can also be coated with metal, providing a strong yet conductive backbone. Nylon was also considered to replace carbon. Silver and nickel are the two most used metals in these studies.

Metallic nanoparticles in carbon nanotube paper

Chu et al. [47] deposited silver nanoparticles (diameter ~25 nm) by photolytic spray onto the SWCnT paper presented earlier. The electrical conductivity of the CnT paper increased from 3.23 S/m to 36.00 S/m. A 14.14 wt% of silver nanoparticles was measured by TGA. The addition of the nanoparticles increased the load retention at flexural failure to 92.1% and reduced the damage depth to 0.3 mm for a DBC test. *Xia et al.* [48] used a DC electrophoretic deposition technique to add silver nanoparticles to their SWCnT paper. With a deposition time of 240 s at a potential of 5V, the conductivity of the SWCnT paper increased by $9.7\times$ from 5.25 S/m to 50.92 S/m. The addition of these particles had the effect of increasing the

retention of the ultimate compressive strength to 91.05%, whereas the ECF retained only 83.28% after a DBC test. The explanation given for this increase was that when the lightning current passes, the silver nanoparticles sinter, recreating a conductive network on top of the damaged CnT network, thus limiting the impact on the CFRP.

Metallic nanoparticles in carbon nanofibre paper

Gou et al. [62] studied a paper containing carbon nanofibres and nickel nanostrands (NinS) in different proportions. CNFP-1 contained 9.75 g of CnF and 9.75 g of NinS while CNFP-2 and CNFP-3 contained 6.94 g of CnF and 19.55 g of NinS. CNFP-1 and 3 consisted of a single sheet while CNFP-2 was made from a sheet containing only CnF and another containing both materials. All solutions were sintered, and a latex binder was then added to improve the handling strength. CNFP-2 and 3 were, respectively, 2,730 and 2,501× more conductive than CNFP-1. After a 100 kA lightning test, the flexural strength was slightly reduced by 10% for CNFP-2 and 3 but was reduced by 61.6% for CNFP-1.

Spray of metal coated carbon nanomaterial

Details in Section 2.3.1.1.

Metal coated nonwoven carbon fibre paper

Details in Section 2.3.1.1.

Metal coated carbon fibre woven ply

Details in Section 2.3.1.1.

Metal coated chopped carbon fibre paper

Details in Section 2.3.1.1.

Metal coated nylon

Details in Section 2.3.1.1.

5.6.1.2 Sacrificial and insulating layer

Some research groups have evaluated the effect of adding an insulating layer between the LSP and the CFRP.

a) Glass fibres ply

Guo *et al.* [63] evaluated the effect of placing a woven glass fibres layer between the sacrificial layer, in this case an EAF or ECF, and the CFRP. This layer, 0.094 mm thick and weighing 102 g/m², improved the LSP efficiency of the laminates when exposed to waveforms C or D. As shown in Figure 0.2, without the GF layer, the first CF ply was exposed once the metallic foil was vaporised and was at some points damaged. However, when a GF layer was added, the CFRP was never directly exposed to the high current and high temperature, as can be seen in the bottom right picture. This explained the increase in the flexural strength retention, from 94.45% to 97.15% for the EAF and from 91.79% to 95.50% for the ECF.

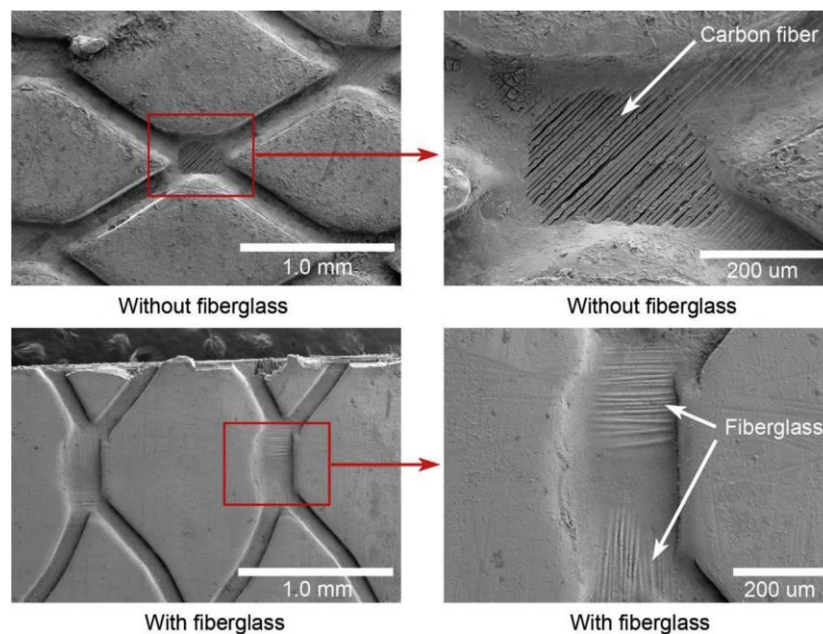


Figure 0.2: Microstructure of protected panels post-lightning. On top without the GF layer, on the bottom with the GF layer. The first CF ply is exposed after the lightning strike without the insulating GF layer [63].

b) Insulating adhesive

The two other adhesives that Han *et al.* [50] tested are insulating. The first (EP) contained only epoxy (Electrical conductivity: 2.3×10^{-8} S/m, breakdown strength in oil: 101.5 kV/mm) and the second (BN/EP) was an epoxy/hexagonal boron nitride (20 wt%) mix (Electrical conductivity: 6.8×10^{-12} S/m, breakdown strength in oil: 185.9 kV/mm). The LSP consisting of a MWCnT foil and a 100, 200 or 500 μm layer of insulating adhesive was tested at currents of 40 and 100 kA. Under equivalent conditions, the BN/EP coating was more resistant to lightning than EP: for a thickness of 200 μm and a current of 100 kA, only

860 mm² was damaged on BN/EP, while 7,420 mm² wide and 1.5 mm deep damage were observed on EP. The compressive strength is maintained after the lightning tests for all BN/EP coatings. As the adhesive is quite heavy (1.4 g/cm³ or 280 g/m² for a thickness of 500 µm), the authors tried to reduce the thickness of the adhesive by a factor of 2, but this resulted in damage similar to those described for EP previously.

The solution developed by *Zhao et al.* [61] and described in Section 2.3.1.1.c was also tested with an insulating film of expandable graphite doped epoxy. This film matched the performance of an ECF with a damage depth of 0.24 mm and a CALS of 401 MPa, only 8 MPa less than ECF, with a 37% lower areal density.

The insulating layer acts as [63]:

- an electrical insulator by limiting the arc attachment to the laminate surface as well as perforation by dielectric discharge,
- as a thermal insulator by protecting the CFRP from very high arc temperatures and gases from the vaporised sacrificial layer by Joule effect,
- as a refractory material that can withstand very high temperatures (up to 1,000 °C for glass fibre, 900-1,500 °C for BN [50] without catching fire).

However, as *Kumar et al.* [36] have noted, the high-intensity discharge emulators used in the laboratory generally operate at relatively low voltages (20 to 30 kV) which are not representative of the voltages found in nature (>100 kV). Thus, the use of dielectric layers for LSP is not recommended until high-current and high-voltage tests are carried out together to confirm their performance.

5.6.2 Inside the laminate

Modifications can also be made within the laminate to increase its resistance to lightning strikes. Several approaches were studied: the modification/replacement of the epoxy resin, the use of thin ply preregs, the addition of layers between the carbon fibre plies, of nanofillers or of conductive wires in the thickness direction. Each solution generally has one or both of the following objectives: increasing the through-thickness conductivity and increasing the interlaminar resistance.

5.6.2.1 Resin modification

a) PANI

Details in Section 2.3.2.1.

b) BMI

Bismaleimide (BMI) is a thermosetting resin with better heat resistance than epoxy. *Kamiyama et al.* [68] specifically studied the effect of resin on LSP efficiency. They exposed CF/epoxy, CF/BMI, and CF/PEEK laminates to 40 and 100 kA lightning strikes. The results of the CF/PEEK are discussed in the next section. At 100 kA, as shown in Figure 0.3, CF/epoxy (a) was destroyed, whereas CF/BMI (b) showed a damage area of 9,500 mm² with some fibre breakage at the attachment point. A bulge of 0.18 mm in diameter and a slight delamination at the back of the panel were also observed. The better LSP efficiency than CF/epoxy can be explained by an almost 100× higher through-thickness conductivity (partly due to the higher fibre volume fraction) as well as a higher resin decomposition onset temperature (370 °C vs. 280 °C).

Zhao et al. [43] fabricated plies of chopped NCCF embedded in BMI resin. The behaviour of this solution was not compared to that of an equivalent solution containing only epoxy resin and will not be discussed here. Same thing goes for *Chakravarthi et al.* [53] who filled a CF/BMI with Ni-SWCnT.

c) Thermoplastic

Polyetheretherketone (PEEK) is a thermoplastic (TP) resin with a high fracture resistance. A CF/PEEK laminate manufactured and tested by *Kamiyama et al.* [68] was the most resistant to lightning test. The damage area reported was 10,390 mm², and resin degradation and fibre breakage were reported at the attachment point, as shown in Figure 0.3.c). No delamination or bulging at the back were reported, contrary to CF/BMI. This good performance was explained by an electrical conductivity equivalent to that of CF/BMI, an even higher resin decomposition onset temperature at 530 °C and a fracture toughness 5 to 8× higher than that of CF/BMI or CF/epoxy. A mechanical test pre- and post-lightning test would help understand the potential of PEEK for LSP.

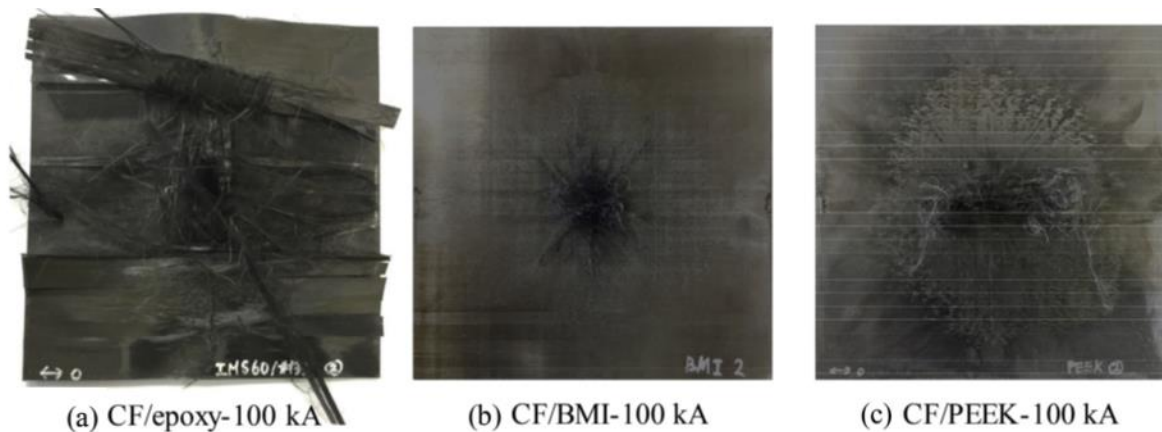


Figure 0.3: Views of laminates manufactured with different resin after a 100 kA lightning strike test. (a) CF/epoxy. (b) CF/BMI. (c) CF/PEEK [68].

Yamashita et al. [91] compared the resistance to lightning strikes of a laminate using thin-ply prepregs with a TP matrix. They used thick plies CFRP (epoxy matrix) and CFRTP (PA6 matrix) with the same stacking sequence as references. These results can be used to estimate the resistance to lightning strikes of TP resin. These two specimens were tested at 40 and 60 kA. In both cases the damage area was larger for CFRTP. However, the retention of mechanical properties in flexure was better for the CFRTP. At 60 kA, CFRP retained only 58% of its flexural strength, while CFRTP retained 65%.

d) Conductive epoxy

Logakis and Skordos [70] made a conductive resin from epoxy and MWCnT (0.1 wt%) which they used in pristine and ECF protected CFRP. The CnT loading was above the percolation threshold in epoxy. After a DBC test, the damage area decreased by 40% and 60%, respectively, compared to an equivalent laminate containing simple epoxy.

PANI-based resins were the most investigated since 2016. CF/PANI laminates showed a better LSP efficiency than CF/epoxy. However, the decrease in the ultimate flexural strength when using PANI-based resin was significant. Using it as a sacrificial layer, like *Kumar et al.* [17] did in 2019, might be the best use for this resin. BMI, thermoplastic resins, or epoxy filled with MWCnT also reduced the damage to the laminate in comparison with the pristine CFRP, but they were not able to prevent all damage as an ECF would. As *Logakis and al.* [70] suggested, conductive resins could be used in addition to a sacrificial layer to increase the conductivity in the through-thickness direction of the laminate.

5.6.2.2 Use of thin plies

Yamashita and al. [71], [92] studied the resistance of CFRTP thin-ply preregs to lightning strikes. They chose this approach because thin-ply preregs showed enhanced mechanical properties in comparison with normal preregs. They fabricated 5 mm-wide CF tows with an air spreading technique. These tows were either directly attached to a PA6 resin film or chopped to 18mm-long tows beforehand, to produce 44 μm thin sheet. Three sheets were stacked to produce a 132 μm thick layer. They produced four sorts of laminates: two quasi-isotropic (QI) with thin or thick layers and two chopped carbon fibre tape (CTT) RTP with again thin or thick layers. These laminates were tested with 20, 30, 40 and 60 kA peak currents.

The damage area was smaller for the laminates using thin-ply preregs. For 60 kA strikes, the reduction in the damage area for the QI laminates was 48% and for the CTT 29%. Fibre sublimation and resin evaporation were observed on all specimens but were limited to the first layer for the specimens using thin layers. However, in these specimens, the number of observed delamination was higher. The flexural strength retention for thick and thin ply laminates were, respectively, 65% and 80% for the QI laminates and 77% and 82% for the CTT laminates, for the 60 kA test. This increase in the retention was explained by the reduction of the electrical resistivity. The laminates using thin plies had a lower in-plane resistivity: 1.5 \times lower for QI and 2.5 \times lower for CTT. The better retention properties of the CTT laminates were explained by the more scattered delamination, occurring between two pieces of CF tape and not between two plies.

5.6.2.3 Interlayers

a) Non-metallic

In addition to a silver-coated carbon fibre nonwoven, *Zhang et al.* [57] put 40 μm thick and 7 g/m² SWCnT films between the first 13 plies of a 24-ply carbon fibre laminate. After DBC tests, the damage area was reduced by 77.6% and the damage depth by 68% compared to the unprotected specimen. Thus, this solution limited the area of the damage, but increased its depth, in contrast to the silver-coated nonwoven alone. However, no mechanical tests were performed to analyse the effect of the added layer.

The mechanical analysis was done by *Kumar et al.* [19]. They fabricated a 150 μm thick, MWCnT-based film, and deposited it on the surface of the laminate and between the first 4 layers. The protected laminate had a flexural strength of 378.25 MPa and a flexural modulus of 43.87 GPa compared to 584.5 MPa and 49.95 GPa for the pristine CFRP. However, the LSP efficiency were greatly improved: after 40 kA tests, the flexural strength was maintained at 99%. It is important to note the very good results of the pristine CFRP. Only a delamination of 30 mm in diameter around the attachment point was observed, without fibre breakage.

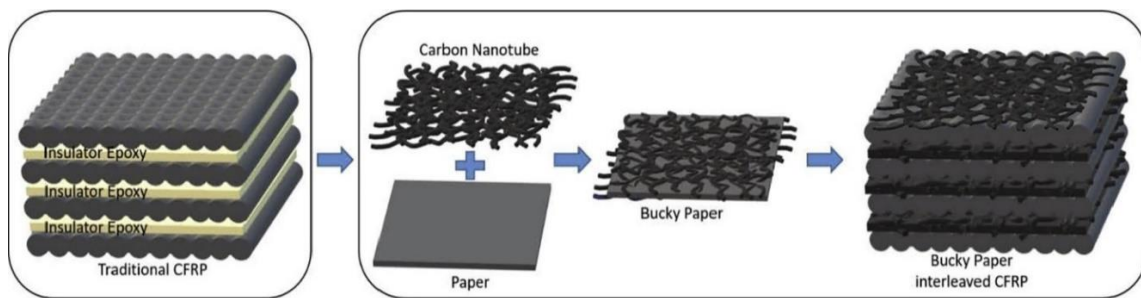


Figure 0.4: Insertion of the MWCnT-based film between the first 4 layers and on top of the laminate to enhance the through-thickness conductivity. Adapted from [19].

b) Hybrid

5.6.2.4 Nanofillers

Details in Section 2.3.2.3.

5.6.2.5 Conductive wires connecting the different plies

a) Metallic

Lombetti and Skordos [74] inserted steel and copper wires between the 10 central plies of a 24-ply carbon fibre laminate. The through-thickness conductivity of the CFRP was 21 S/m, and the addition of these wires increased the conductivity by 20 and 250 \times , respectively. The crack propagation toughness was increased by 2 and 3 \times , respectively. These composites were exposed to a Zone 2A test. The sample containing copper wires showed similar damage in depth and area to the ECF, while the sample containing steel wires showed more damage in depth (3.3 \times more than the ECF) and in area (1.8 \times more than the ECF).

b) Hybrids

Rehbein et al. [75] plated nylon wires, containing a different number of filaments, with silver. They used these yarns to form multi-axial non-crimp fabrics (NCFs). These fabrics were stacked with a silver-coated carbon fibre nonwoven between each layer. This increased the through-thickness conductivity by a factor of 5.7 to 31.4 and the in-plane conductivity by a factor of 1.04 to 2.78 depending on the nylon yarns used and the presence or absence of the nonwoven. After exposure to a DBC test, laminates containing no nonwoven veils, but silver-plated nylon yarns showed a 90% reduction in damage depth compared to CFRP. The addition of nonwoven veils only reduced the damage depth by 20-30%. The yarns resulted in an added mass of only a few grams per square meter. However, this led to a decrease in the volume fraction of fibres in the laminate, thus reducing its mechanical performance. To achieve the same fibre areal density, additional plies must be added, limiting the weight gain to 20-45 g/m² in comparison with a 195 g/m² ECF.

APPENDIX B SIMULTANEOUS THERMAL ANALYSIS (STA)

We performed a STA on a CF panel. Three samples were heated at different heating rates: 5 °C/min, 10 °C/min and 25 °C/min, as shown in Figure 0.5. A priori, only one reaction was taking place in the baseline composite: the epoxy matrix pyrolysis. This reaction started at 367 °C for the 5 °C/min heating rate, at 382 °C for 10 °C/min and at 398 °C for 25 °C/min. Hence, the higher the heating rate was, the higher the onset temperature of the resin pyrolysis was. These heating rates were several orders of magnitude lower than the heating rate the panels were subjected to during a LS test. Hence, we expected the resin pyrolysis to occur at higher temperature during the tests. We measured a different char yield, 64%, 70% and 69%, for the three samples at different heating rates. This disparity can be explained by the different fibre weight fraction among the samples. However, these values are accurate: the resin weight fraction of the preregs was 37 wt% before curing.

We only did a basic analysis of the differential scanning calorimetry curves, and the onset temperature of the resin pyrolysis was in the same range.

We also performed a thermogravimetric analysis on a paint sample. The degradation started around 250 °C and three reactions were observed. These data were used to establish the criteria for the thermal camera observations.

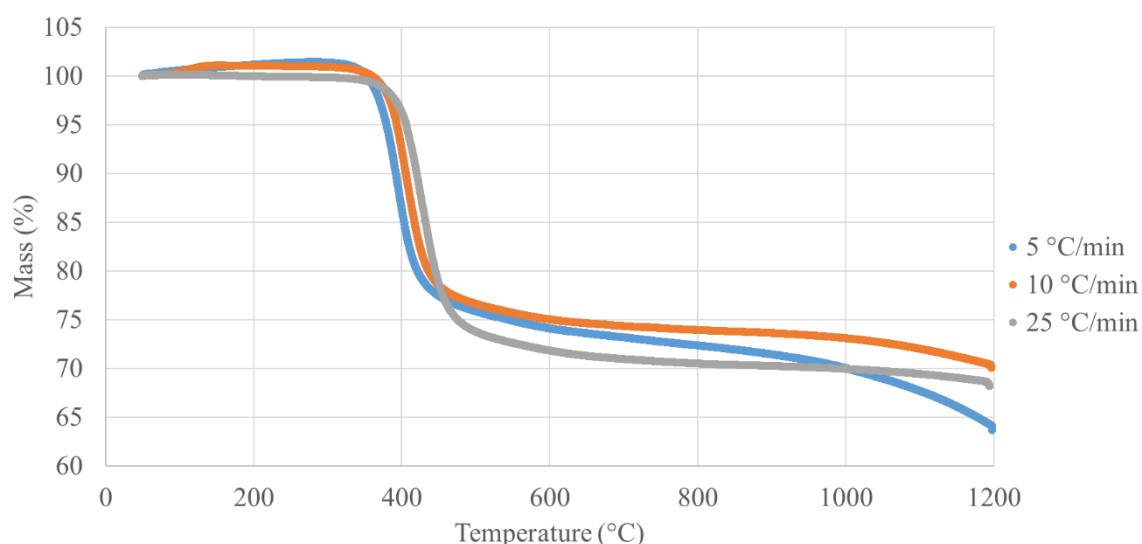


Figure 0.5: Thermogravimetric analysis of a CF panels at three heating rates: 5, 10 and 25 °C/min

APPENDIX C EMISSIVITY

We measured the emissivity of four samples: CF, PCF, ECF and PECF at different temperatures and infrared wavelengths using a reflectometer. As shown in Figure 0.6, the emissivity was independent of the temperature for CF. The same behaviour was observed for the other four samples. The emissivity had a small dependence on the wavelength. In our case, the average over the wavelength was sufficient as input for the thermal camera.

As listed in Table 0.1, CF and ECF had an emissivity of 87.4% and 89.5%, respectively. The painted panels emissivity was a little higher with 92.4% and 92.8% for PCF and PECF. Based on these measurements, we used an emissivity of 89% for all the nonpainted panels and of 92% for the painted panels.

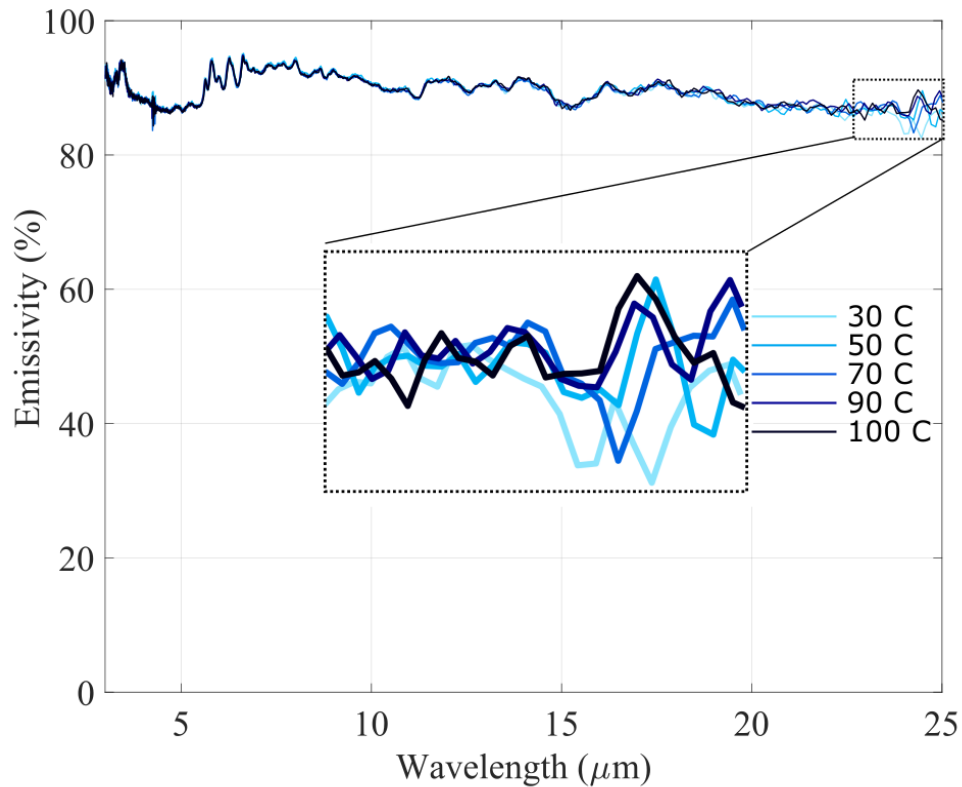


Figure 0.6: Emissivity of a CF sample at different temperatures and for infrared wavelength ranging from 2.5 μm to 25 μm

Table 0.1: Materials emissivity measured with a reflectometer.

Materials	CF	PCF	ECF	PECF
Emissivity (%)	87.4	92.4	89.5	92.8

APPENDIX D COMPUTATION OF THE EQUIVALENT ELECTRICAL CONDUCTIVITY BASED ON SEM OBSERVATIONS

We also computed an equivalent conductivity σ_{eq} of the NCCF filament. We considered the carbon filament and the nickel coating in parallel on a given length l . Hence:

$$\begin{aligned} \frac{1}{R_{eq}} &= \frac{1}{R_{CF}} + \frac{1}{R_{Ni}} \\ \Leftrightarrow \frac{S_{tot} \times \sigma_{eq}}{l} &= \frac{S_{CF} \times \sigma_{CF}}{l} + \frac{S_{Ni} \times \sigma_{Ni}}{l} \\ \Leftrightarrow \sigma_{eq} &= \frac{S_{CF} \times \sigma_{CF} + S_{Ni} \times \sigma_{Ni}}{S_{tot}}, \end{aligned}$$

Where S_{CF} is the section of the carbon fibre filament, S_{Ni} is the section of the nickel coating, $S_{tot} = S_{CF} + S_{Ni}$, $\sigma_{CF} = 10^5 \text{ S/m}$ is the conductivity of the carbon fibre filament and $\sigma_{Ni} = 1.44 \times 10^7 \text{ S/m}$ is the conductivity of nickel. The results are listed in Table 0.2. Since the carbon fibre filament section is the same in all NCCF-based material, the thicker the nickel coating thickness, the higher the equivalent conductivity. However, $\sigma_{eq,NW0.04}$ is still almost 6× smaller than $\sigma_{eq,ECF} = \sigma_{Cu} = 5.96 \times 10^7 \text{ S/m}$.

Table 0.2: Equivalent electrical conductivity of the NCCF filament of the woven and nonwoven in comparison with the copper filament

LSP	Equivalent electrical conductivity of a filament (10^6 S/m)
ECF	59.6
NC0.09	1.86
NW0.5	4.05
NW0.3	6.84
NW0.1	7.76
NW0.04	10.6

These values might also be used for a numerical simulation of the electrical conduction or the LS test.

APPENDIX E ELECTRICAL ARC ATTACHMENT OBSERVATIONS

To better understand the interaction between the composite panels and the electrical arc we developed a setup to create a low current discharge at the surface of the panel. We used the high voltage source, the high voltage probe, the oscillator, and the injection setup used for the lightning strike emulation. The copper electrode was located 1 cm above the panel surface and the panel was grounded. When the source was switched on, the electrical potential in the electrode rose until it was high enough (~11-13 kV) to create a discharge between the electrode and the panel, and so on. We let the discharge happen for ~3 minutes per panel, at the rhythm of more than 100 discharges per second. We photographed the discharges with a 100 mm lens and a 1/50" exposure time.

Based on these observations, we observed three different attachment behaviours, as shown in fig.... For each column, the first two images are photographs of an electrical arc between the copper electrode and the panel surface. The last photographs present the state of the panel surface after 3 minutes, highlighting the different attachment points.

We could describe the three attachment behaviours as follow:

- Single attachment point (PECF, PCF and PNS0.1): all electrical arcs attached on a single point for a long time. This point might change after a while, like on PCF or PNS0.1, or drift closer to the tip of the electrode, like on PNS0.1,
- Multiple attachment points (ECF): electrical arcs attached on multiple preferential points of the copper mesh, mostly at the crossings.
- Random multiple attachment points (NS0.1 and CF): electrical arcs attached on multiple points with no preferential points.

In fact, these results only highlight the amount of potential attachment points for the electrical, i.e., the points where the potential difference with the copper electrode is the lowest. Hence, when the panels are painted, the attachment point does not vary because the paint is already evaporated at this point.

But these results are not useful to understand the constraining effect of paint on the arc root radius or the difference in behaviour between PECF and the other painted panels.

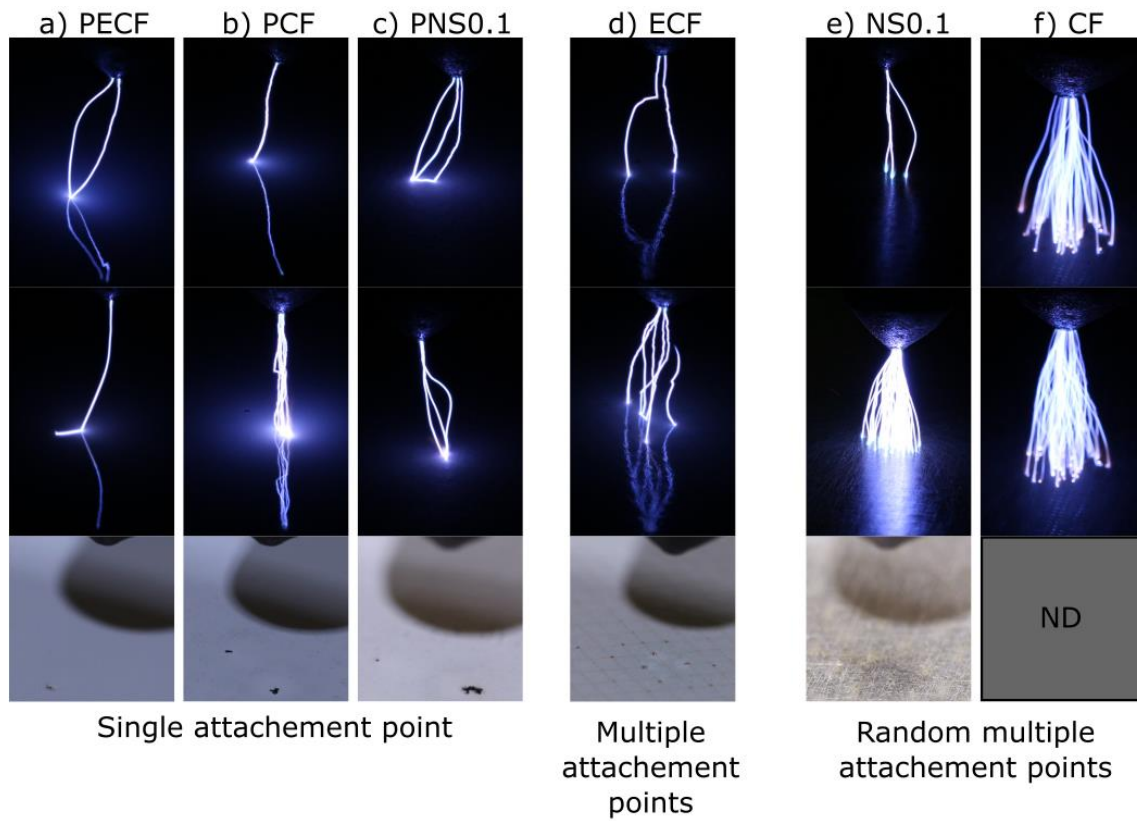


Figure 0.7: Observed electrical arc attachment behaviours on the surface of nonpainted and painted composite panels. Single attachment point: a) PECF, b) PCF, c) PNS. Multiple attachment points: d) ECF. Random multiple attachment points: e) NS and f) CF.